AFRL-OSR-VA-TR-2015-0056

STRENGTHENING SUPERCONDUCTIVITY IN MACRO-ARRAYS OF NANOCLUSTERS AND NANOSTRUCTU

Anvar Zakhidov
UNIVERSITY OF TEXAS AT DALLAS

02/05/2015
Final Report

Air Force Research Laboratory
AF Office Of Scientific Research (AFOSR)/ RTD
Arlington, Virginia 22203
Air Force Materiel Command

REPORT DOCUMENTATION PAGE

Form Approved
OMB No. 0704-0188

1. REPORT DATE *(DD-MM-YYYY)*
11-02-2015

2. REPORT TYPE
Final Performance

3. DATES COVERED *(From - To)*
01-09-2009 to 31-10-2014

4. TITLE AND SUBTITLE
STRENGTHENING SUPERCONDUCTIVITY IN MACRO-ARRAYS OF NANOCLUSTERS AND NANOSTRUCTURES

5a. CONTRACT NUMBER

5b. GRANT NUMBER
FA9550-09-1-0384

5c. PROGRAM ELEMENT NUMBER

6. AUTHOR(S)
Anvar Zakhidov

5d. PROJECT NUMBER

5e. TASK NUMBER

5f. WORK UNIT NUMBER

7. PERFORMING ORGANIZATION NAME(S) AND ADDRESS(ES)
UNIVERSITY OF TEXAS AT DALLAS
800 W CAMPBELL RD
RICHARDSON, TX 75080 US

8. PERFORMING ORGANIZATION REPORT NUMBER

9. SPONSORING/MONITORING AGENCY NAME(S) AND ADDRESS(ES)
AF Office of Scientific Research
875 N. Randolph St. Room 3112
Arlington, VA 22203

10. SPONSOR/MONITOR'S ACRONYM(S)
AFOSR

11. SPONSOR/MONITOR'S REPORT NUMBER(S)

12. DISTRIBUTION/AVAILABILITY STATEMENT
A DISTRIBUTION UNLIMITED: PB Public Release

13. SUPPLEMENTARY NOTES

14. ABSTRACT

Objective of this project was to create nanostructured superconducting systems with higher Hc and Jc for power applications as nanocompositewires and also to search for new types of superconducting nanomaterials with higher critical temperature Tc. The interfacial novel phase have beenconfirmed to have a record Tc = 47-49 in Pr and other rare earth doped Ca 122 pnictide superconductors by ultrasensitive low-field microwaveabsorption method. Coexistence of lower Tc and higher Tc observed by LFMA proves the interfacial nature of newly found SC phase. on thecontrary the LFMA in 122 pnictide shows only one signal and one phase. In thin films of FeSeTe films deposited by pulsed laser deposition veryhigh Hc, (estimated to be 186 T by HWW formula) has been achieved at the compositions close to antiferomagnetic order. Flexible, weavable andknottable superconducting magnesium diboride yarns have been fabricated that provide attractive gravimetric properties as a superconductor, whilehaving a 20 times lower density than for bulk MgB2.

15. SUBJECT TERMS
NANOCLUSTERS, NANOSTRUCTURES

16. SECURITY CLASSIFICATION OF:			**17. LIMITATION OF ABSTRACT**	**18. NUMBER OF PAGES**	**19a. NAME OF RESPONSIBLE PERSON**
a. REPORT	**b. ABSTRACT**	**c. THIS PAGE**			Anvar Zakhidov
U	U	U	UU		**19b. TELEPHONE NUMBER** *(Include area code)* 972-883-6218

Standard Form 298 (Rev. 8/98)
Prescribed by ANSI Std. Z39.18

Final Performance Report for the AFOSR program *FA9550-09-1-0384*

Project Manager: Dr. Harold Weinstock

STRENGTHENING SUPERCONDUCTIVITY IN MACRO-ARRAYS OF NANOCLUSTERES AND NANOSTRUCTURES

PI: Dr. Anvar Zakhidov
Co- PI: Dr. Ray Baughman
Dr. Myron Salamon

Institution: University of Texas at Dallas
BE 26, 800 West Campbell rd.
Richardson, TX 75080

Sub-contractors: Dr. Apparao Rao, Clemson University,
Dr. Lisa Pfefferle, Yale University (first 3 years of project),
Dr. Haiyan Wang, Texas A&M University (TAMU), last 2 years
Dr. Wei-Kan Chu, Houston University, Texas Center of Superconductivity

Funding and Reporting period: November 1, 2009 till October 30, 2014
(with no cost extension)

This program is linked and partnering with two internationally funded AFOSR programs:

1. Search of SC in CNT by Haruyama in Japan,
2. Superconductivity at interfaces led by Yakov Kopelevich in Brazil in University of Campinas

Table of Contents

9. Personnel supported

10. Publications of team members related to program

11. Interaction/Transitions.

12. APPENDIXES:

Appendix 1: Cryo-Centers with 3 closed cycle Li-He cryostats created in UTD in support of this AFOSR project,

1. Statement of Objectives.

The First objective of the proposed program is to identify new classes of higher critical temperature Tc superconductors in a family of nanostructured low dimensional materials:

1. In 1-d nanowires and nanotubes, including BN and BCN nanotubes synthesized in Yale
2. Search of superconductivity in bundles of SWCNT upon doping
3. In 2-d graphene based systems upon ion implantation
4. In novel layered Fe based 112 and 122 pnictides and Fe 11 chalcogenides
5. In Boron doped graphene and Boron doped diamond.

This task can be solved by developing a methodology for combined search by 3 component test: 1) Zero resistance: R(T) = 0, 2) Meisner effect: M(T) turning to diamagnetic at Tc, 3)Microwave absiorption: Abrupt appearance of low field microwave absorption (LFMA): dP/dH non zero below Tc. This third LFMA ultrasensitive contactless test (capable of detecting nanograms of SC phase) in combination with ESR was chosen as “Occam’s Razor” to cut out the claims of superconductivity in many materials in which only one of signatures of superconductivity: R(Tc)=0 or M(Tc) <0 was observed.

Second main Objective is to demonstrate the possibility of creating and development of ultraflexible, lightweight superconducting wires based on nanocomposites of MgB2 and FeSete family based layered superconductors coated on mechanically strong carbon nanotubes.

<u>The overall detailed objectives of the proposed Project are following:</u>

- Identify the new classes of low dimensional materials, which can be promising for higher Tc superconductivity, such as Boron nanotubes, BN-nanotubes (synthesized by Yell University team), using combination of magnetic, transport and microwave techniques: ESR and LFMA or MMMA.
- Confirm superconductivity in Boron doped SWCNT by a ultrasensitive microwave LFMA test and study P, S and other dopants effects on SWCNT and MWCNTs
- Confirm the INTERFACIAL nature of superconductors based on 122 pnictides materials for higher Tc > 49 K. Design new interfacial superconducting systems.
- Search of higher Tc in various interfacial systems including FeSe on STO and other substrates
- Develop a general approach for creating superconducting wires based on CNT conducting cores, coated by layered superconductors;
- Develop cost-effective technologies for fabrication of the MgB2@CNT ultraflexible superconducting wires.

- Evaluate the performance of such nanocomposite MgB2@CNT wires. Demonstrate possibility to obtain high critical current and critical fields in nanocomposites.

The specific objectives of Program effort for CNT can be summarized as follows:

- Evaluate methods for creating superconducting nanocomposite wires, such as PLD (by TAMU sub-team), PPD (by UTD), SPS (by Clemson) and find optimum parameters of nanocomposite Sc@CNT wires. required for practical implementation of the proposed lightweight wires for Air Force power applications;
- Test different techniques, particularly a combined LFMA/ESR microwave ultrasensitive method for confirmation of superconducting state in 2-D and interfacial new superconductors.
- Experimentally and theoretically prove the feasibility of the increased Tc in 2-D interfacial systems, such as Ca 122 pnictides, a concept proposed by Paul Chu for pr-doped Ca 122 pnictide crystals.

Challenges in Superconducting Materials: Higher Tc, Jc and Hc

Superconductivity, first witnessed in mercury by Kamerlingh Onnes in April of 1911[i], is a phenomenon whereby a material's electrical resistance vanishes when its temperature is reduced below a critical threshold. Additionally, a superconductor will completely expel any magnetic fields from inside itself through the Meissner effect, discovered by Walther Meissner and Robert Ochsenfeld.[ii] This separated these materials from being considered simply perfect conductors and further defined the superconducting state.

Even now over a hundred years later, new and more varied superconductors with their own unique properties are still being uncovered. Among them are the iron based pnictides and chalcogenides, such as $EuFe_2As_2$, FeSe, and their relatives. In the iron chalcogenides, thin films deposited on single crystal substrates by pulsed laser deposition (PLD) show an enhancement of their superconducting transition temperature in relation to the bulk, and an increased critical current density as well as a high upper critical field.[iii] These are all highly desirable qualities for nearly every application, from current carrying wires to high strength superconducting magnets. The capacity for deposition is especially useful as it allows for the fabrication of more complicated structures as well as versatility. We will examine the reported and measured properties of some type Ba, Ca-122 and $EuFe_2As_2$ pnictides, and type-11 FeSe and FeTe chalcogenide thin films deposited by pulsed laser deposition on a variety of substrates including carbon nanotubes. UTD has the extension of the research into pulsed plasma deposition: PPD of the type-11 chalcogenides, high field measurements of FeSe0.1Te0.9 thin films deposited by PLD, and alternate substrates of single walled carbon nanotubes, which both showed superconducting Tc.

Low field microwave absorption LFMA as an ultimate test for Superconductivity.

Low-field microwave absorption, or LFMA, is a powerful technique for advanced characterization of superconducting materials. Especially when combined with the traditional tools of electrical resistance (transport), and magnetization, superconductivity can be claimed with a high degree of accuracy and confidence. However, additionally to confirming macroscopic details such as T_c found from transport and magnetic measurements, LFMA can provide insight into its microscopic superconducting nature, can detect and separate additional phases of extremely small volume fraction (10^{-11}cm^3) and/or critical field, and can even be used to characterize the nature of Josephson junctions (insulating or normal state). These properties are either difficult or impossible to determine from magnetization or transport alone. In addition, the technique is rapid, non-contact and non-destructive, and can be performed on an EPR spectrometer.

In the dissertation of Austin Howard, prepared as a result of this program (all details can be found in the Ref 30 of Publications) the LFMA technique was applied to characterize several novel superconducting materials, in particular pnictides and chalcogenides, with the purpose of clarifying outstanding questions as to their true nature. We also introduce, for the first time, an extensive vision of the LFMA technique to the multiple frequency domain in order to isolate individual signal origins, providing even more fleexibility to this already powerful technique.

1. Search for Superconductivity with high Tc in carbon nanotubes CNT and other novel nanosystem.

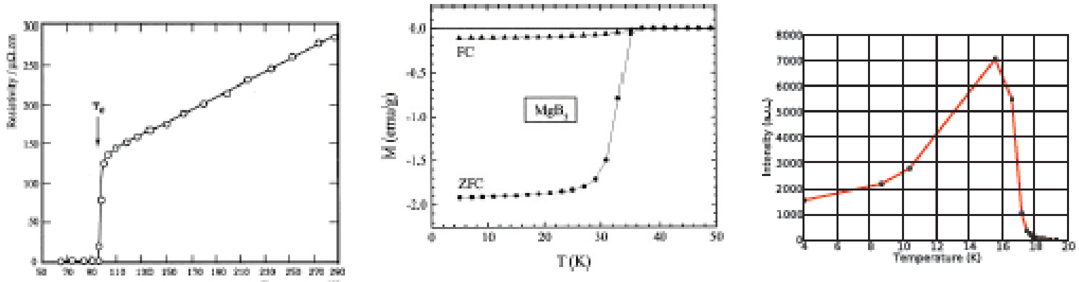

(a) Transport ($R = 0$), discovered in 1911 by Kamerlingh Onnes

(b) Meissner Effect, or Magnetization ($\chi = -1/4\pi$), discovered in 1932 by Meissner and Ochsenfeld

(c) Low-field Microwave Absorption (LFMA), discovered in 1987, with the discovery of YBCO

Figure 1.2: Superconductivity detection methods

When Kamerlingh Onnes proclaimed resistance of “mercury practically zero" in a historic laboratory notebook entry in April 1911, he began a remarkable series of discoveries into the field of superconductivity (Figure 1.2). Kamerlingh Onnes' great achievement was reaching 4.2 K with helium, as his discovery of zero resistance below the critical temperature (T_c) involves nothing more than a voltmeter and current source.

Twenty years later, Meissner and Ochsenfeld would discover that placing a superconductor in an external magnetic field caused the field immediately outside to increase, corresponding to a complete expulsion of the field inside the superconductor. The “Meissner effect" means that below its critical temperature (T_c), a superconductor exhibits perfect diamagnetism ($\chi = -1/4\pi$ in cgs units), and therefore the phenomenon of superconductivity is also measurable by a magnetometer, as well as an ohmmeter.

These two measurement techniques: transport (electrical resistance) and magnetization (in SQUID or other magnetometers) are still the most commonly used for characterization of superconductors. While sensitivity and accuracy have improved over the last 100 years, these methods still generally detect bulk scale effects of a SC transition. For simple (Type I) superconductors (such as Kamerlingh Onnes' mercury), these techniques are perfectly reliable: true 0 resistance is readily obtained, and complete field expulsion ($\chi= -1/4\pi$) occurs suddenly at T_c. Even for most Type II superconductors, few problems arise with definitively measuring a superconducting transition.

However, when investigating the more complicated superconductors that are the focus of current research, we come into several problems. For example:

1. The volume fraction (fraction of total volume which is in a superconducting state) may be small, restricting the minimal magnetic susceptibility.

2. Occasionally, we study materials which have almost two-dimensional superconducting regions, providing for a volume fraction which is so small that it is difficult to detect relative to the bulk signal by transport or magnetic susceptibility.

3. If not properly pinned, vortices can move (by Lorentz force) in response to current flow, thus destroying the true vanishing resistance state. Alternatively, disconnected islands of superconductivity may be present in the material, eliminating a percolation pathway and not allowing for true zero resistance R=0.

These issues can make bulk scale measurements difficult and unreliable. A drop in resistance which does not reach zero, or diamagnetism without $\chi= -1/4\pi$, may be ignored, or, worse, falsely ascribed to superconductivity, as in reality there are many other possible reasons for this behavior.

To combat this issue, we can turn to a relatively unused, yet powerful, technique, known alternately as “Low-field Microwave Absorption" (LFMA) or \Magnetically Modulated Microwave Absorption" (MMMA or MMWA).[y] LFMA is a non-contact method to probe the microscopic nature of superconducting materials, instead of measuring bulk properties. By directly measuring the interaction of microwave radiation with superconducting vortices and Josephson Junctions (JJ) present in all Type II superconductors, we can detect superconducting phases with very low volume fraction, and garner more definite evidence of a superconducting state. Additionally, we can gather orientation dependent information.

We will show below that only if 2 of test shown at Fig. 1 are positive one can be confident that superconductivity is detected. In other cases, particularly if only one test is positive, the claims are most probably false. Indeed we showed in this program, that SC-ty claimed in Boron-doped SWCNTs and also in BN and BCN type nanotubes did not passed a “Occam’s Razor” test by LFMA and negative M(T)<O true diamagnetism, while R=0 found initially in MWCNT upon ion implantation by B, S and P was going in some samples all the way to negative R puzzle, and also did not passed an LFMA test, implying that SC-ty is not yet confirmed, although cannot be

excluded with more careful M studies in ultra clean samples (with no magnetic catalyst imporities).

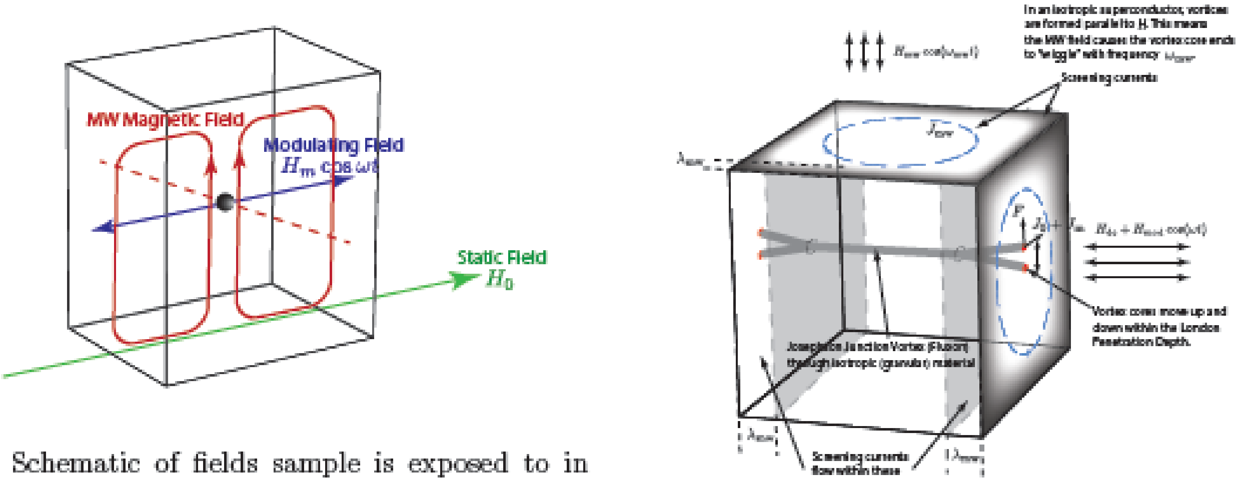

(a) Schematic of fields sample is exposed to in ESR. The MW polarization (electric field) vector is along the z-axis, while both magnetic fields are aligned along the y-axis.

(b) Magnetic fields and currents sample is exposed to in LFMA.

Figure 2.1: Schematics of system

Some details of LFMA system are shown at Fig. 2.1., while the detailed description of LFMA method and all the mechanisms of microwave absorption in superconducting phase is described in Thesis of A. Howard (publications 31). The mechanisms of LFMA due to fluxon penetration into SC JJ loop and RSJ model of JJ: Josephson Junction network based model of LFMA are shown at Fig. 2.5 and details can be found in same thesis.

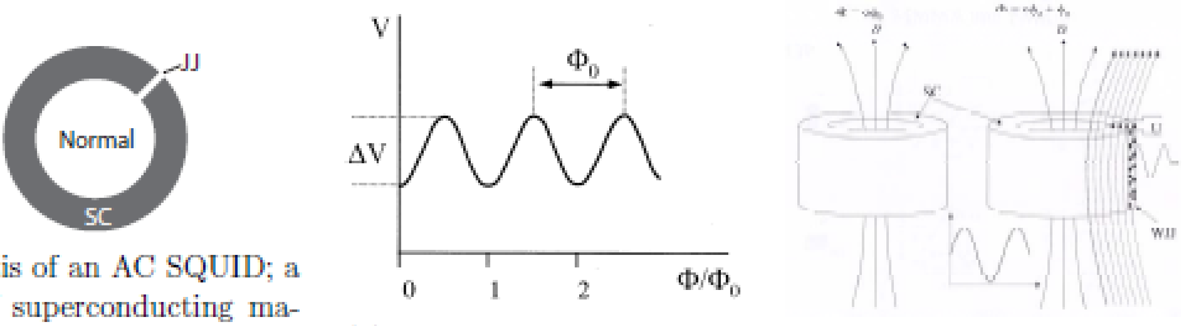

(a) Basis of an AC SQUID; a loop of superconducting material with a single JJ.

(b) Response of an AC SQUID. [?]

(c) Penetration by fluxons into Josephson Loop. [?]

Figure 2.5: Fluxon and RSJ Model Concepts

1.1.Introduction: Why Carbon nanotubes are specially attractive for Superconductivity?

1.1.1 Carbon nanotube CNT properties and applications and prospects for superconductivity as ultrastrong SC wires

Since first being observed by Iijima [1] in soot produced by d.c. arc-discharge evaporation of a graphitic target, carbon nanotubes (CNT) have been attracting the attention of scientists and engineers for more than 20 years. Very soon after the discovery numerous theoretical studies predicted remarkable physical and chemical properties of individual single-wall (SWNT) and multi-wall carbon nanotubes (MWNT) (Table 1). Some of these properties have been confirmed experimentally and promise great potential to use CNTs in various applications [2].

Although carbon nanotube-based materials for practical use are still under development. Many applications require CNTs to be self-assembled in a periodic or aligned manner to have improved mechanical, thermal and electrical properties [3, 4]. Even though many commercial products already incorporate nanotubes in a basic way, there are plenty of areas where a complicated synthesis and refinement treatment of high quality CNTs is required, making most applications not economically competitive with existing cheap commercial analogues.

Most commonly, CNTs are utilized in the form of thin films, or interconnected networks. Several synthetic methods have been developed to produce high-purity, high-quality free-standing films of carbon nanotubes with different number of walls, such as vacuum-filtration of SWNT suspensions [5, 6], drop-casting[7], aerosol CVD synthesis of SWNT [8], or drawing of CNT sheets from a vertically aligned CNT forest [9, 10, 11]. Thin films can also be obtained by low-cost processes such as dip-coating, spin-coating, and spray coating [12, 13], although this group of methods requires substrates, and CNT films cannot be provided in a free-standing form. The number of applications that have been suggested with the use of CNT thin films is enormous and well-described in literature, including optoelectronic devices as transparent conducting electrodes [11, 14, 15], sound projectors[16, 17, 18], polarizers [19, 20, 21, 22], bolometers [23], and actuators [24]. Additionally these films can be twisted into yarns with high mechanical strength, electrical conductivity, temperature and chemical stability [25]. Composites of CNT films and yarns with functional materials allow extending applications in many areas [26].

Physical property	Theoretical prediction for individual CNT	Experimental measurement of individual CNT	Examples of CNT-based material properties	Properties of analogous non-CNT material
Tensile strength	130 GPa (SWNT) [27]	~52 GPa (SWNT) [28] ~63 GPa (MWNT) [29]	0.64 GPa DWNT cables [3] 1.3 GPa wet-spun CNT fibers [4]	1.6–2.5 GPa Maraging steel
Young's modulus	5.5 TPa (SWNT) [30]	~1470 GPa (SWNT) [28] ~950 GPa (MWNT) [29]	200 GPa wet-spun CNT fibers [4]	200 GPa steel

Electrical conductance	$2G_0{}^1$ (SWNT)	$(0.4-0.5)\cdot 2G_0$ (SWNT) [31] $490\cdot 2G_0$ (MWNT) [32] $(5-7)\cdot 2G_0$ (MWNT) [33]	$7\cdot10^6$ Sm^{-1} DWNT cables [3] $5\cdot10^6$ Sm^{-1} wet-spun CNT fibers [4]	$6\cdot10^7$ Sm^{-1} copper wire
Maximum current density	~10^9 A cm^{-2} (SWNT) [34]	$4\cdot10^9$ A cm^{-2} (SWNT) [35] ~10^8 A cm^{-2} (MWNT) [32] ~10^{10} A cm^{-2} (MWNT) [33]	$1.6\cdot10^6$ A cm^{-2} DWNT cables [3] 10^5 A cm^{-2} CNT fibrils [36]	$1.4\cdot10^4$ for copper wire 0.5 mm diameter
Thermal conductivity	6600 Wm^{-1}K^{-1} (SWNT) [37]	3600 Wm^{-1}K^{-1} (SWNT) [35]	640 Wm^{-1}K^{-1} wet-spun CNT fibers [4]	3320 Wm^{-1}K^{-1} pure diamond [38]

Table 1: Physical properties of carbon nanotubes

1.2. Clemson University Sub-Tasks on CNT synthesis and Doping

In the past four years, Clemson and UTD teams have collaboratively endeavored to produce superconducting materials that exhibit high critical field and current density. To this end, Clemson team adopted a multi-pronged approach (as shown in Fig. 1) to produce nanostructured superconductors by completing the following tasks:

Task 1-Synthesis of B-, N-, S- and P-doped carbon nanomaterials (single-, double-, & multi-walled carbon nanotubes and graphene) using in-situ and ex-situ approaches.

Task 2-Synthesis of nanocomposite materials using aligned and randomly oriented carbon nanotube paper (also known as buckypaper) and superconducting materials such as MgB_2 for enhancing critical currents by vortex pinning, and

Task 3-Development of non-linear optical, and Raman spectroscopic methods to identify the dopant configuration, environment, and bonding configurations.

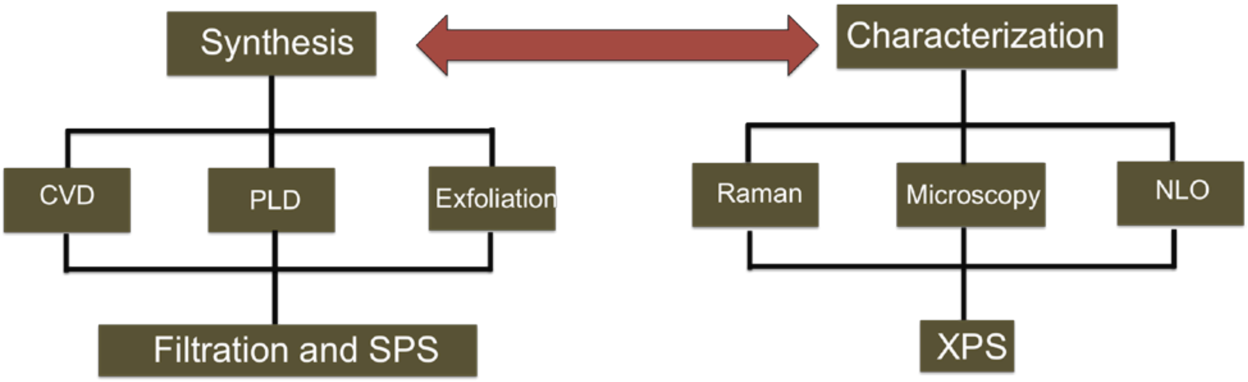

—**Figure 1.6**: A schematic describing the multi-pronged approach of Clemson team for achieving carbon-
[1] (based superconductors with high current density.

Herein, we present the summary of Clemson team's efforts in achieving carbon-based superconductors.

Task 1-Synthesis of doped carbon nanomaterials: The possibility of doping/intercalation in carbon materials has attracted much interest from researchers since it allows the tailoring of structural and electronic properties for realizing unique properties. For example, calcium intercalated graphite (C_6Ca) and highly B-doped diamond exhibit superconducting properties and charge density waves. In case of carbon nanomaterials, unique density of states (van Hove singularities in CNTs) and strong electron-phonon coupling present ideal conditions for attaining high T_c. In fact, Clemson team's previous collaborative efforts with Haruyama's group have shown promising results of superconductivity in B-doped SWCNT bundles [1]. Along similar lines, Ping Sheng's group from Hong Kong University observed superconductivity in DWNT bundles while Grover Larkin's group noticed indications of superconductivity in P-doped graphite [2,3]. Based on these exciting results, Clemson team synthesized several doped nanomaterials using different approaches. In this section, we present the synthesis and characterization summary of all the samples that are prepared as a part of this project.

Numerous samples prepared both in Clemson and in Japan have been tested by combination of Resistance, magnetization and LFMA methods and reported at several APS and MRS meetings and AFOSR reviews.
Summarizing those we can say that M(T) shows downturns, mimicking meissner effect (see below) but S-ing LFMA has never been observed.

1.3.Synthesis of original CNT sheets in UTD and processing of CNT sheets.

Carbon nanotube sheets from spinnable forest: synthesis and characterization.

Vertically aligned forest of MWNT have been synthesized by catalytic chemical vapor deposition (CVD). Silicon wafers with native oxide were covered with 3 nm of Fe catalyst by e-beam deposition. Prepared substrates were cut into small pieces (from 25x25 mm to 25x75 mm each) and put inside 3-zone CVD reactor (46 mm inner diameter). The growth was performed at temperatures 700-750 ℃, growth time was 10 min in a low of the mixture of He (~70%), H_2 (~30%) and acetylene (2-5%). During heating and cooling steps the furnace was flashed with He (1000 sccm).
Produced forest of CNT exhibited properties of drawability and spinnability (Figure 7).
Depending on synthesis conditions, forests of different heights and densities can be produced, which immediately influence CNT-drawn sheets thickness and densities.

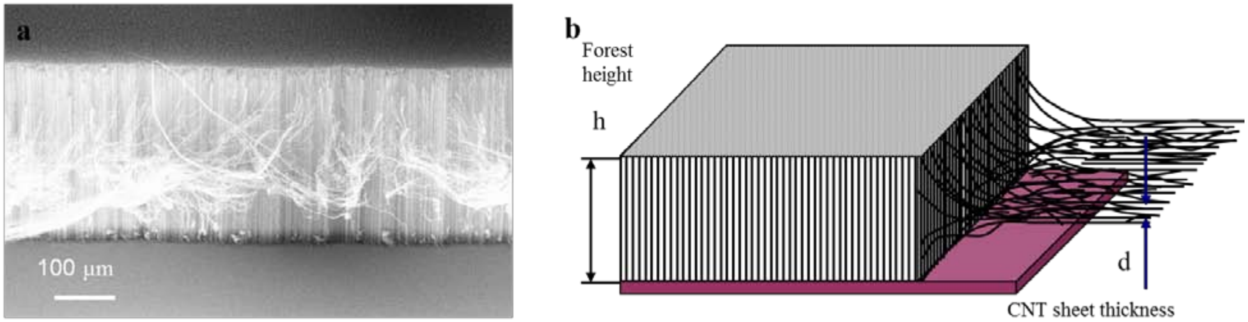

Figure 1.4: a) Side view of CNT forest (SEM); b) schematic representation of dry-drawing process of the CNT sheet from the CNT forest, where ***h*** is a forest height, and ***d*** is the CNT aerogel thickness.

By ranging the furnace temperature, duration of synthesis and position of substrates inside the reactor, forests of different heights can be produced. Forests showed spinnability properties in a wide range of heights: from 150 to almost 800 um (Figure 8a). CNT sheets drawn from different forests exhibited different sheet resistance and transparency which varied in a wide range and strongly correlated with the forest's height. Short forests (150 um) were transformed into sheets which had low conductivity (relative sheet resistance R_{sh} ~1500 Ohms/sq) and high transparency (T ~ 90%). At the same time from tall forests (up to H~ 800 um) CNT sheets with low sheet resistance (R_{sh} ~200 Ohms/ sq) and low transparency (T ~ 30-40%) were produced.

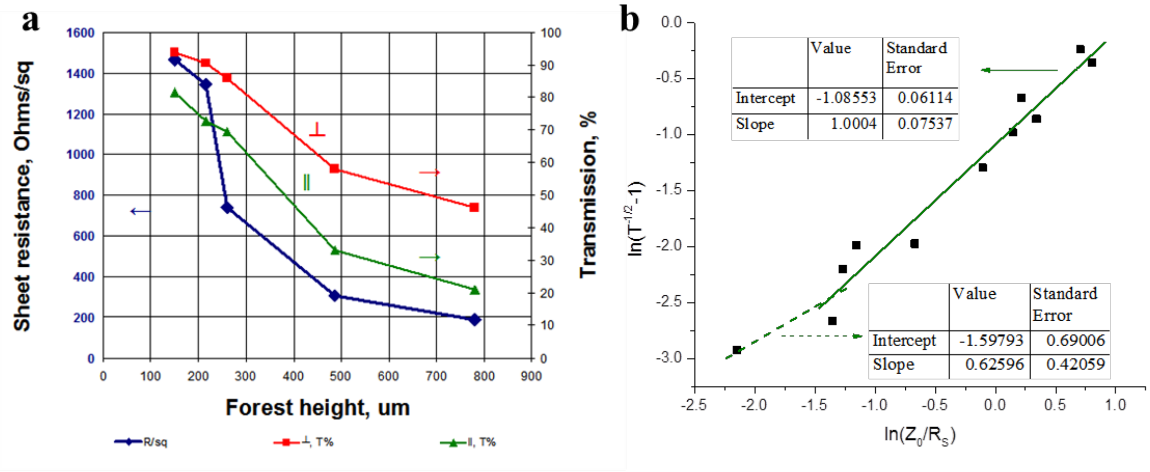

Figure 1.5: a) Forest height versus sheet resistance and transparency at wavelength 550 nm for 5 different forests. CNT sheets were deposited on glass and densified with alcohol. Blue curve corresponds to sheet resistance, red curve – transparency measured in light polarized in direction perpendicular to the sheet orientation, green curve – transparency measured in light polarized in direction parallel to the sheet orientation; b) analysis of conductive regime in CNT sheets using bulk-like equation (3.1) (solids green line) and percolative regime equation (3.2) (dashed green line).

We can characterize properties of CNT sheets in a framework of transparent conductors. Equations (1.2) and (1.4) can be transformed into linearized equations with variables $[\ln(T^{-1/2}-1)]$ and $\left[\ln\left(\frac{Z_0}{R_{sq}}\right)\right]$: equation (3.1) for bulk-like behavior and equation (3.2) for percolative network:

$$\ln(T^{-1/2}-1) = \ln\left(\frac{\sigma_{op}}{2\sigma_{dc}}\right) + \ln\left(\frac{Z_0}{R_{sq}}\right) \quad t > t_{min} \tag{3.1}$$

$$\ln(T^{-1/2}-1) = -\ln\Pi + \frac{1}{1+n}\ln\left(\frac{Z_0}{R_{sq}}\right) \quad t < t_{min} \tag{3.2}$$

Both regimes can be identified for CNT sheets of various thicknesses (Figure 8b), although the percolative regime is only relevant for films with very high transparency. Since only few samples in our study are in this range, the estimation of figure of merit Π varies between 2.5 and 10. In overall the most relevant model of CNT sheets is as a well interconnected network with d.c. conductivity independent of thickness, and it is valid for the most samples used in our study (Figure 8b). The slope of the fitted line is ~1, which followed the proposed equation (3.1), and figure of merit is $\frac{\sigma_{dc}}{\sigma_{op}} = 1.48 \pm 0.09$. This value is very low for practical applications, where figure of merit of 35 is required, and additional treatment to improve conductivity can be made [10].

The dependence of transmission of CNT sheet on a direction of light polarization is observed (Figure 8a) and it follows from the anisotropy of nanotube orientation inside the sheets - nanotubes tend to orient along the drawing direction.

.

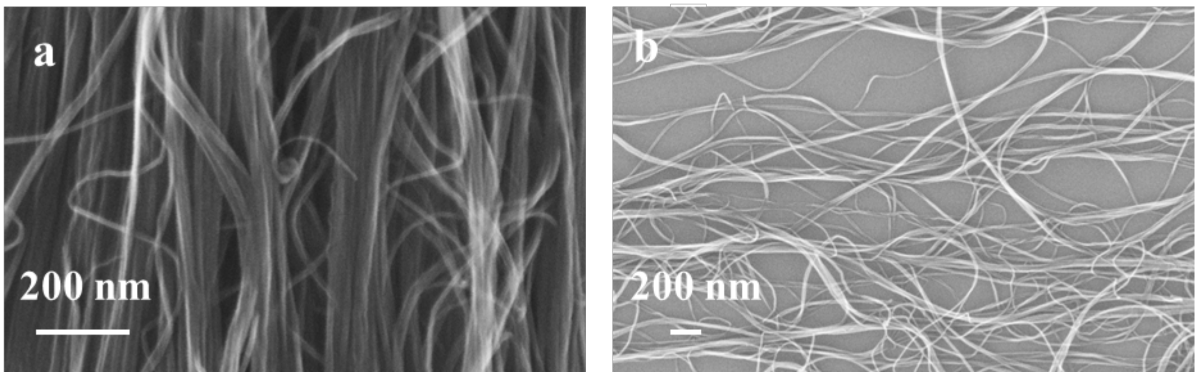

Figure 1.6: SEM images of densified CNT single sheets: a) thick sheets dry-drawn form forest of longer 550 µm height; b) thin sheets dry drawn from forest of shorter 200 µm height.

Conductivity and transmission of carbon nanotube films produced by dry-drawing from vertical CNT forest have been characterized. CNT sheets have been shown to be a relatively good polarizer with high temperature and chemical stability. The main advantage of such polarizers is their great performance in a ultrawide wavelength range, which cannot be covered with commercial polymer and wire-grid polarizers. UV, visible, infrared and terahertz spectroscopy have been used to study optical anisotropy.

Figure 1.7. Typical carbon vapor deposition system.

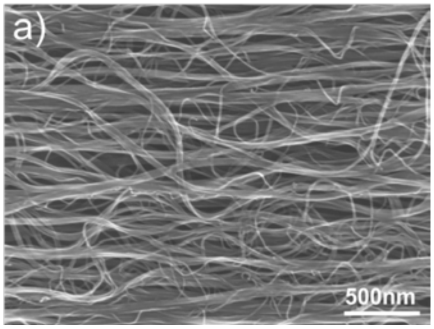

Figure 1.8. SEM image of oriented multiwall CNT sheet.

.

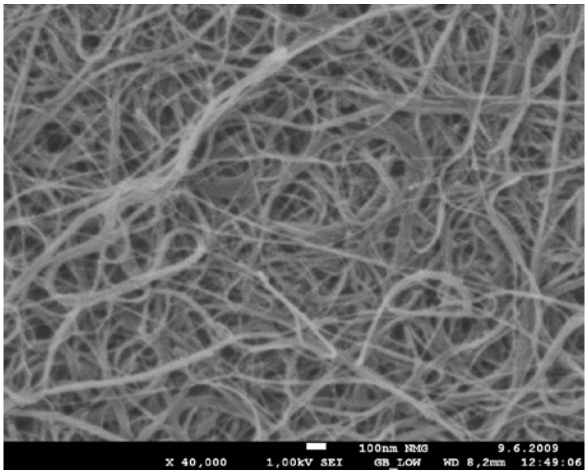

Figure 1.9. Non-oriented SWCNT grown via aerogel method in vertical reactor

1.3.Theoretical concepts on enhancing Tc in ropes of single wall SWCNT:

We have developed theoretical description of a bundle of SWCNTs that contains semiconducting and metallic tubes with interstitial Boron type doping or Charge transfer type intercalation doping. Due to doping Tc can be increased due to two possibilities considered below shortly:

1.3.1. Increasing Tc in bundles of semiconducting and metallic SWCNTs

Full description of this theory has been published (as Ref. 26 in Published papers) and below we show only short description of approach and results.

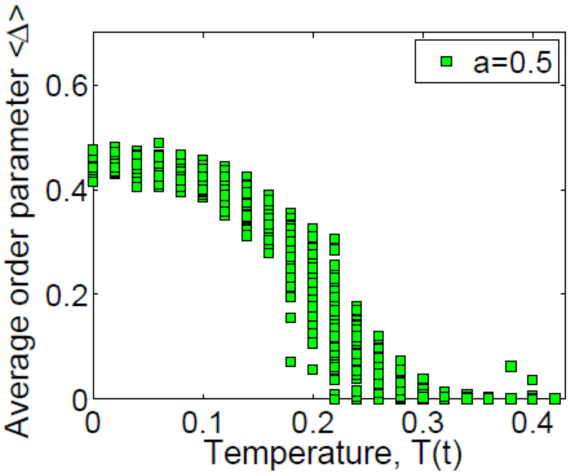

FIG. 4: A set of spatially averaged order parameters (in units of t) as a function of temperature used for statistical average over different configurations at the percolation regime ($a = 0.5$). Note that the distribution has a limited variation width.

It is expected that doping of SWCNTs in a bundle by, for example, boron, may signifficantly improve their superconducting properties[6]. At a proper level of doping the Fermi level may be at a one dimensional singularity of the energy spectrum that gives a higher density of states (DOS), that will lead to a higher critical temperature T_c. In particular, we assume here that such kind of mechanism of doping enhanced T_c may be much better pronounced in the case of semiconducting SWCNTs, which may have higher DOS due to lower in energy van Hove singularities. This is in contrast to metallic SWCNTs, where singularities in the DOS are much higher in energy, and start being filled much later during the doping process (according to the Kataura plot[8]). This means that a bundle consisting of doped semiconducting nanotubes could be a much better superconductor, compared to a bundle made of metallic SWCNTs.

However, synthesis of SWCNTs by currently known methods usually results in a mixture of semiconducting and metallic nanotubes. Since the nanotubes after the synthesis initially are not doped (or unintentionally slightly p-type doped, e.g. by oxygen of atmosphere), those are only metallic tubes, which may have superconducting transition, while semiconducting tubes will be \diluting" superconductivity in the bundle by the inverse proximity effect. Upon doping (i.e. by electrochemical methods), the semiconducting tubes can become superconducting with a higher superconducting gap and thus a higher T_c than in metallic nanotubes.

One may try to estimate a spatially averaged order parameter and the corresponding effective critical temperature for a bundle consisting of a mixture of these two types of SWCNTs. From an experimentalist's point of view it is even more important to solve a bit more complex problem: for a given fraction of doped semiconducting SWCNTs in the bundle and the experimentally determined critical temperature T_c, to predict the critical temperature for a bundle, consisting only of doped semiconducting SWCNTs. It will be also interesting to know, whether it is possible to obtain the critical temperature T_c higher than in other carbon based nanostructures, like in alkali metal doped fullerenes.

Spatial variations of the superconducting order parameter are signifficant for nanoscale systems, including nanotubes. In this work we used a microscopic theory based on inhomogeneous Bogoliubov-de Gennes equations to establish how the superconducting properties of a bundle depend on the fraction of doped semiconducting nanotubes. We assume that the nanotubes in the bundle are approximately of the same radii and tightly packed making a triangular lattice in the bundle's transverse cross-section, with the primitive vectors ~a_1 = R~x, ~a_2 = R~x=2 +p =2R~y. Here ~x; ~y are the unit basis vectors, and R is the average intertube distance. The lattice can be enumerated by indexes (p; k), which correspond to the position of a nanotube $R_{p;k}$ = ~$a_1 p$ +~$a_2 k$, but in this work we prefer to enumerate nanotubes in a N _ N bundle using a single index through the mapping $i = p + kN$, where N is the number of nanotubes in the raw. The doped semiconducting nanotubes are assumed to occupy the fraction a of the sites in the bundle, and the metallic nanotubes occupy the 1 □ a fraction of the sites. A full three dimensional description of a bundle taking into account the band structure and chirality of individual nanotubes would make simulations of the Bogoliubov-de Gennes equations too complex. On the other hand, assumption about the translation invariance along the longitude direction of the nanotubes would make the simulations marginally simpler, because one still needs to deal with quantum problem in three dimensions, but at the same time this assumption would throw away the band structure diffeerence between semiconducting and metallic nanotubes. In this study we adopted a simplified two dimensional picture which allows us to repeat our simulations several dozens of times for different arrangements of the nanotubes in the bundle. In the two dimensional picture the conduction electrons can stay in a nanotube or can hop to the neighboring nanotubes (sites).

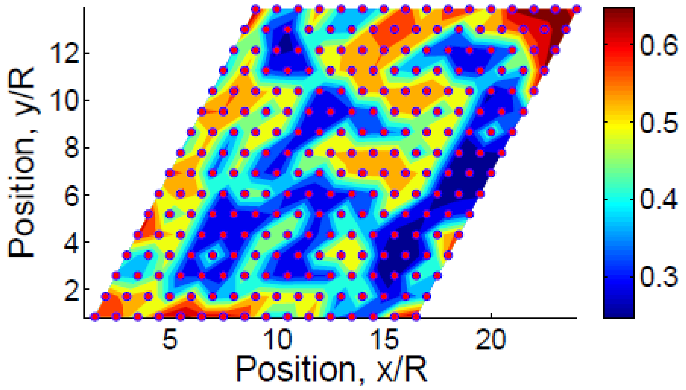

FIG. 5: A particular realization of the spatial distribution of the superconducting order parameter (in units of t) at the percolation regime ($a = 0.5$) and zero temperature. Red dots mark the triangular lattice of a 16×16 bundle.

According to our model for an optimally doped bundle consisting of 100% semiconducting SWCNTs the T_c should increase to the unsuppressed T_c of 19−20K (please see Fig. 3). The effect of T_c suppression similar to discussed here has been observed in alkali metal fulleride molecular alloys of $A_x(C_{60})_x(C_{70})_{1-x}$ and adding non-superconducting component, i.e. C_{70} molecules, which do not show any superconducting pairing due to symmetry reasons and probably due to weaker electron-phonon coupling, strongly suppressed T_c from 19 K in 100% C_{60}, i.e. in K_3C_{60} to T_c=10 K in 20% substituted C_{70} alloy. The experiments with selectively separated metallic and semiconducting SWCNTs, which now become available by new methods of effective separation will allow to check the validity of presented here simple model and to clarify the role of quantum fluctuations, which has not been accounted here.
One has to note that even for relatively small bundles 16_16 the physical properties have relatively small variations for different realizations of the spatial distributions of semiconducting nanotubes. To support this observation we plot a whole set of the spatially averaged order parameters for 50 random configurations of the nanotubes for different temperatures. We choose the equal number of the metallic and semiconducting nanotubes in the bundle $a = 0{:}5$. In Fig. 4 one can see there are relatively limited variations of the order parameter corresponding to different configurations of the nanotubes. The overall dispersion is limited to approximately 0:05t at zero temperature, and becomes relatively significant at temperatures approaching the critical temperature. For experimentalists this means one needs to take extra care about her measurements of small samples near the critical temperature.
In Fig. 5 we plot a particular realization of the spatial distribution of the superconducting order parameter (in units of t) at the percolation regime ($a = 0{:}5$) and zero temperature. In Fig. 5 red dots mark the triangular lattice of a 16_16 bundle. One can see the formation of big clusters of nanotubes with the same superconducting properties. For the measurements

of the transverse conductivity of such bundles at finite temperatures one should expect to see a dramatic drop of the conductivity for $a > 0{:}5$, i.e. above the percolation threshold for the triangular lattice. At this concentrations the semiconducting nanotubes will likely create a connected network within a finite bundle of nanotubes. We propose that this prediction will be tested experimentally.

1.3.2.Ion screening in 1-d systems: promise for SC-ing pairing in ionic doped CNT

Intercalation-type doping is an important practical means of providing the electronic subsystem with (extra) charge carriers without disrupting its chemical-bond skeleton. For quasi-1D systems, this doping is, for instance, a major route for controlling electric properties of conducting polymers. High dopant concentrations may be achieved in different ways: by traditional chemical volume doping or by interfacial double layer charging , particularly with ionic liquids Many intercalation-doped systems exhibit qualitatively new properties such as superconductivity in graphite compounds in fullerides and in hydrocarbons. In addition to supplying charge carriers, dopant ions and intercalants in general may however also play other roles. So the size of the dopant is known to critically affect the distance between the fullerene molecules in alkalidoped fullerides . Electron coupling with intercalant vibrations was attributed to be the reason for higher SC transition temperatures in certain graphite compounds as well as in fullerides

In the (paper 3 in Publications) we have emphasized the role of the collective dynamics of dopant ions for quasi-1D electronic conductors as a source of the ensuing long-range electronion Coulomb interaction, similarly to how it occurs in 3D for the BCS model. We point out that the dynamical response of the dopants may radically affect the interplay of the interactions by effectively screening the long-range electron-electron repulsion and thereby creatingmore favorable conditions for SC correlations. This represents another example of strong effects that may take place upon embedding 1D electronic systems in 3D environments. Our demonstration is based on the model of an anisotropic 3D system of Coulombically-interacting parallel Luttinger-liquid chains introduced by Schulz that will be supplemented by their Coulomb coupling to the ionic subsystem. Being interested only in the spinindependent long-range Coulomb interactions, we limit our discussion here to the Coulomb forward-scattering processes with small momentum transfer $\mathbf{q}$ ($g2 = g4$ processes in the g-ology language), for which the macroscopic expression for the bare Coulomb interaction

$$V0(\mathbf{q}) = 4\pi/q2,\ q2 = q2x + q\perp, \quad (1)$$

is valid. Here the 3D momentum ($h = 1$) $\mathbf{q} = (qx, \mathbf{q}\perp)$ is specified via its components along, qx, and perpendicular, $\mathbf{q}\perp$, to the chains.

We have demonstrated (details can be found in paper 3 of Publications) that the dynamical response of the intercalated dopant ions may have a significant effect on the interplay of DW and SC instabilities in quasi-1D electronic systems. More favorable conditions for SC correlations are achieved via the screening of the long-range electron-electron repulsion by the ionic charge density polarization. The efficacy of this screening is particularly strong for the jellium-like ionic response making the low-energy electron-ion system excitations behave as for the non-interacting electrons. In the effective 1D electron model this would correspond to forward scattering coupling constants $g2 = g4$ vanishing at small momentum transfer. It is known for 1D electron systems with repulsive interactions that, with the inclusion of backward scattering processes (coupling constant $g1$), it is the sign of the combination $2g2-g1$ that determines the dominant superconducting SC (negative sign) *vs* DW (positive sign) correlations. One may want to speculate then that perhaps the vanishing of the effective $g2$ due to the screening by the ionic jellium is sufficient to drive the system towards the SC behavior. This however needs to be checked with a self-consistent treatment of the ionic effects on backward scattering, which is beyond our current scope. On the other hand, we showed that the existence of the electron interaction with another non-polarizational phonon mode can result in negative effective $g2$ for small momenta. In this case, SC correlations may develop already due to the forward scattering only. It is clear that the presence of dopant ions may also cause detrimental effects such as the electron localization – presumably avoidable for sufficiently high dopant concentrations, the latter is of course also needed for practically meaningful magnitudes of the ionic plasma frequency Ωp. For instance, concentration $ni = 1021$ cm−3 of sodium ions would yield $\Omega p \simeq 66$ K. It has been shown experimentally that the concentration of dopant ions in bundles of carbon nanotubes can bevaried in a wide range by interfacial double layer charging in electrolytes and ionic liquids strongly affecting theelectronic work function, transport and optical properties. While the model system we discussed in this paper is a 3D assembly of 1D chains, it is conceivable that the basic physical effect could also be operative in thinner layers.

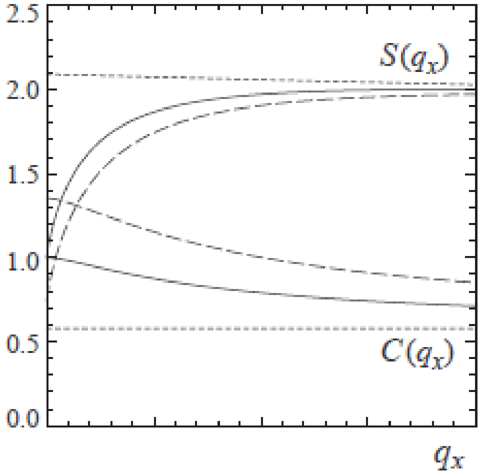

FIG. 2: The momentum q_x-dependent functions $S(q_x)$ and $C(q_x)$ in Eq. (25) calculated using the model parameters of Fig. 1 for a square lattice of chains with $\pi/a_\perp = \omega_p/v_F$. These functions for SC and DW correlations are calculated each for the three of discussed model cases: short-dash lines show the behavior in the system of just electronic plasmons, solid lines for the system of electrons plus jellium-like dopant ions (Fig. 1(a)), and long-dash lines for the system of electrons plus jellium-like dopant ions plus one non-polarizational phonon mode (Fig. 1(b)).

Part 2. Search for Superconductivity in CNT upon various doping and in nanocomposites

Doping may induce defects in their walls. This step is most important as it creates the necessary defects for allowing dopant substitution. Next, the refluxed SWNTs were vacuum filtered using a 0.45 µm nylon membrane and washed thrice with boiling deionized water and dispersed into ethanol suspensions containing the dopant precursor (B_2O_3 powder for B-doping, melamine for N-doping, phosphoric acid for P-doping, and elemental S powder for S-doping). Following a 1 h bath sonication and evaporation of the ethanol, the SWNTs mixture are annealed at 180 °C in a 100:10 sccm Ar:H_2 gas flow for 2 hours. Finally, all the samples are annealed in flowing Ar at 1000 °C for 30 min to allow reconfiguration of defects/dopants.

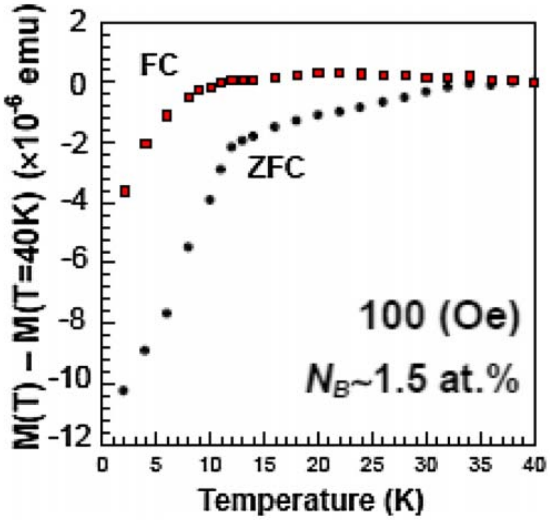

Figure 2.1: Normalized magnetization as a function of temperature at magnetic fields (H) of 100 Oe in FC and ZFC regimes in thin films of assembled B-SWNTs, which are synthesized from a target with nominal doping content N_B~ 1:5 at:%

Fig. 4 shows the XPS spectra of B-doped SWNTs prepared using MEA with 0.5, 1 and 4.0 at% B2O3 powder (labeled as S1, S2 and S3). The C1s photoemission spectrum for pristine SWNTs (which has been thoroughly investigated in Ref.6 by Clemson team) exhibits a binding energy peak ~284.45 eV. It is well known that the position of C1s peak varies with B- or N-doping. In case of MEA, we found that the C1s peak was downshifted by ~0.15 eV in B-doped SWNTs, in agreement with our previous results on laser ablated B-doped SWNTs [9]. Furthermore, we observed that the C1s peak width in all the samples (S1, S2, and S3) is ~0.6 eV similar to the laser ablated SWNTs. As shown in Figs. 4 b-d, the B1s core signal may be deconvoluted into two peaks at 191.5 and 192.8 eV, which correspond to the presence of substitutional B in the SWNT lattice and B_2O_3 respectively. The latter peak (~192.8 eV) most likely appears due to any residual B_2O_3 left in the samples during the synthesis procedure. The substitutional B-doping contents are shown in Table 1. As expected, we observed that the net substitutional B content increased with increasing nominal concentration of B_2O_3 in the synthesis indicating the MEA is suitable for achieving high doping concentrations. We have prepared several samples of SWNTs, DWNTs, and graphene samples using MEA for testing superconductivity in doped carbon nanostructures. A comprehensive list of these samples is given in the attached excel sheet.

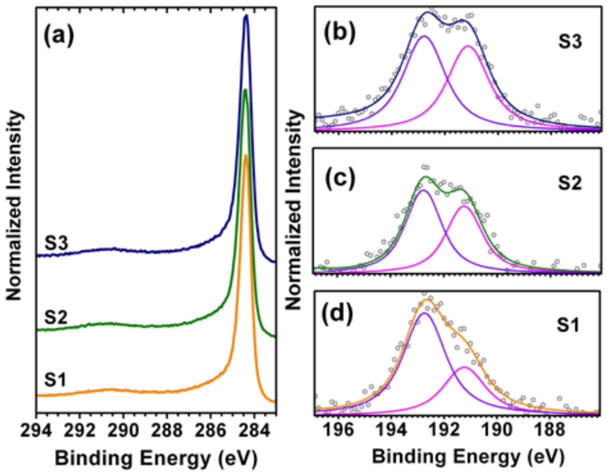

Figure 2.2: The C1s (panel a) and the B1s lines (panels b-d) for the three B-doped samples prepared using the modified Eklund approach.

Previously, several groups have suggested the possibility of superconductivity in S-doped graphite [10]. For this reason, we have studied the magnetic properties of S-doped samples in detail. Below, we briefly discuss the magnetization results obtained on some of the doped SWNTs and graphene nanoplatelets (GnP).

Sample ID	Nominal B2O3 Concentration	Substitutional B content (at. %)
S1	0.5	0.19
S2	1	0.22
S3	4	0.42

Table 2.1: The dopant content of three B-doped SWNTs prepared using MEA. The second column shows the nominal concentration of B_2O_3 used in the synthesis procedure for preparing S1, S2, and S3 samples. The third column shows the percentage corresponding to B in substitutional configuration as determined from XPS.

Experimental evidence for ferromagnetism in graphene-related systems has been controversial. Several studies have previously shown the presence of ferromagnetic (FM) ordering in highly oriented pyrolytic graphite (HOPG) and carbon films at room temperature. Recently, Nair *et al.* showed that point defects in graphene (such as fluorine dopant atoms and defects caused by ion-irradiation) carry magnetic moments with spin ½ [11]. In our samples, we observed an unexpected presence of ferromagnetism (FM) in pristine GnP. While many groups have attributed magnetic ordering to defects and edges in GnPs, the mechanism (direct/indirect exchange) responsible for the FM ordering at room temperature is still unclear. The fundamental understanding of this mechanism can possibly open new avenues for defect/dopant-engineering to achieve superconducting phase transition via enhanced electron-phonon coupling. For this reason, we studied the influence of defects and dopants on the FM of GnPs by subjecting bulk few-layer graphene to chemical exfoliation and sulfur doping.

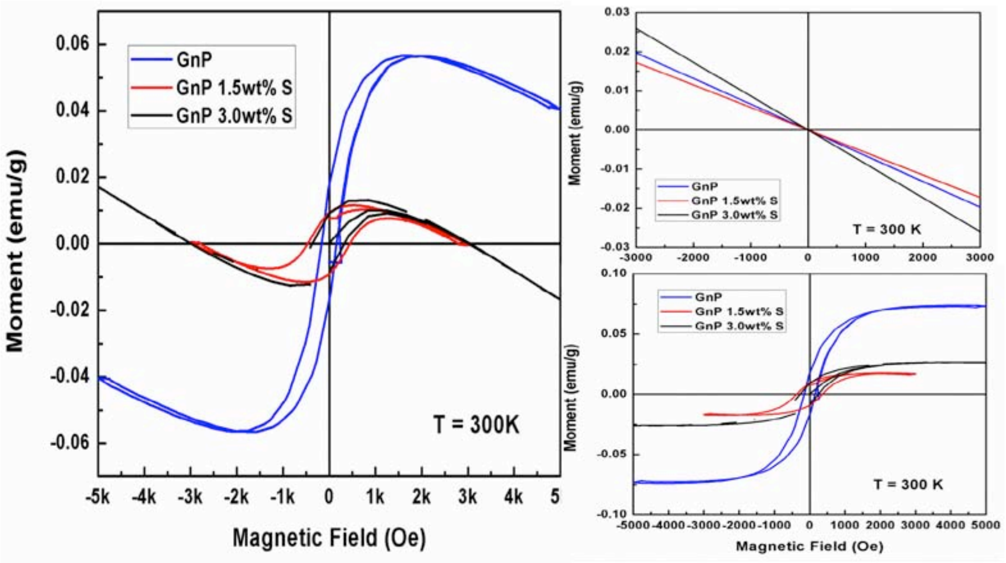

Figure 2.3: a) Magnetization curves for pristine and doped graphene samples at 300 K obtained at Clemson University. b) Diamagnetic contribution to the net signal

We found that the saturation magnetization of GNPs systematically decreased upon sulfur doping suggesting that S-dopants demagnetize defects in GNPs. Our density functional theory calculations provide evidence for defect demagnetization by the formation of covalent bonds between S-dopant and defects concurring with the experimental results.

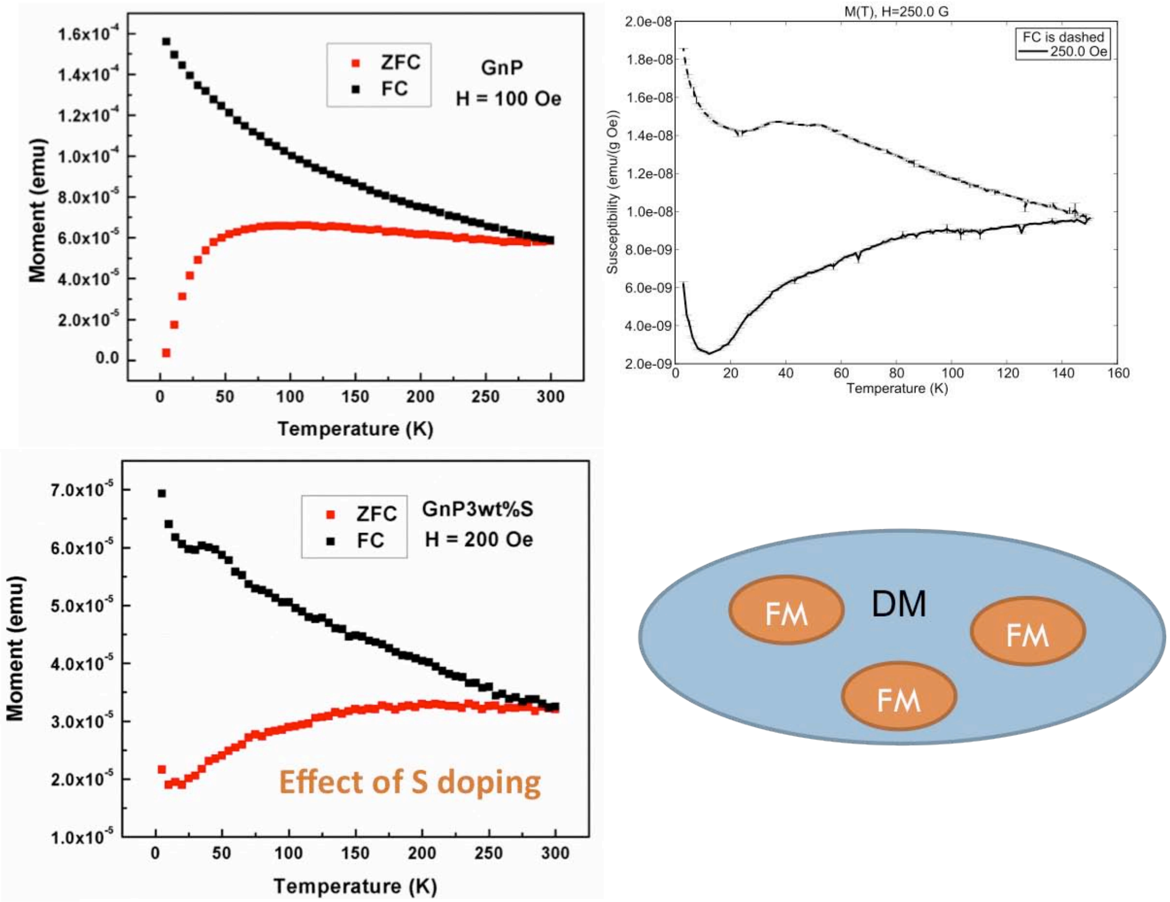

Figure 2. 4: a), b) and c) show dependence of magnetic moment on temperature for all the graphene samples. Clearly, all the samples exhibit diamagnetic type response similar to bulk graphite ~30 K. d) shows the possible magnetic domains in graphene samples.

As shown in Fig. 2. 5, we observed significant FM ordering in both pristine and S-doped graphene samples at 300 and 5 K. The magnetization (M) vs. applied field (H) curves show FM-like hysteresis superposed on a diamagnetic (DM) signal. We decoupled this diamagnetic response from the total magnetic signal (see Fig. 5b). The net ferromagnetic signal in the samples is shown in Fig. 4c. Similar signature was observed at 5 K (data not shown) suggesting that samples posses interacting defects leading to FM ordering. This observation is novel since the defects do not act as non-interacting spins, as shown by Nair *et al* [11]. We believe that S-dopants interact with each other via pi-orbitals of graphene or adsorbed oxygen leading to FM ordering. Furthermore, susceptibility showed peculiar dependence on temperature (see Fig. 6). As shown in Fig. 6a, Pristine GnP showed a dip in susceptibility ~30 K comparable to the well-known diamagnetism in graphite. Similar changes were also observed in 1 and 1.5 at% S-doped GnP. In addition, S-doped GnPs exhibit a valley below 30 K, which upturns for T <20 K (see Fig. 6c). These features may be caused by interacting S-dopants that form FM domains within the sample. It is possible that our samples contain FM and DM domains as depicted in Fig. 2.6d. Along similar lines, S-doped SWNTs also showed peculiar M vs T behavior upon S-doping similar to GnP (as shown in Fig. 7). In fact, the field cooled magnetization data of all the S-doped SWNT samples exhibits a FM phase transition in agreement with the Landau mean-field theory. A clear transition can be observed in all the samples ~200 K along with an evident slope change ~30 K. In conclusion, S-doped GnP and SWNTs exhibit strong FM ordering due to the introduction of defects.

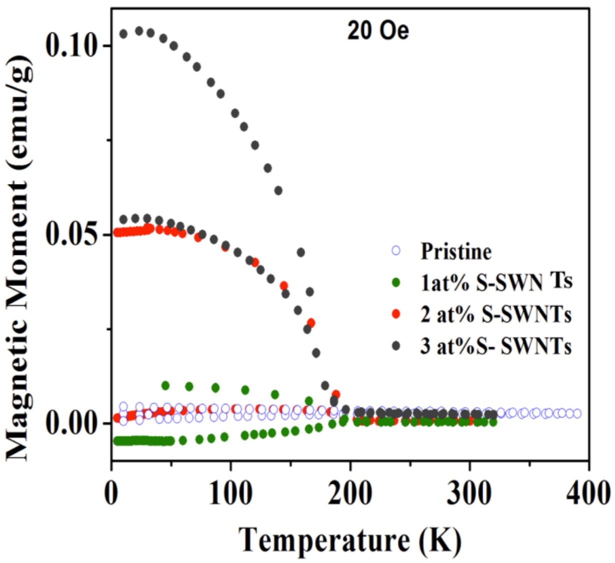

2.4. Chemical Vapor Deposition (CVD) and equipment developed for CVD:

The CVD technique is an important method for doping heteroatoms into the carbon lattice. Using this technique, Clemson team has synthesized a variety of samples including N-doped MWNTs, Pb-doped SWNTs, and N-doped graphene sheets. As shown in Fig. 8, Pb-catalyzed SWNTs showed significant drop in net magnetization ~20 K indicating the possibility of superconducting regions in the sample. In our extensive discussions with UTD, we realized that these drops may be arising due to known superconductivity of Pb ~8 K.

Figure 2.5: Zero-field cooled magnetization data of all the S-doped SWNT samples is in agreement with the Landau mean-field theory. A clear transition can be observed in all the samples ~200 K along with an evident slope change ~30 K.

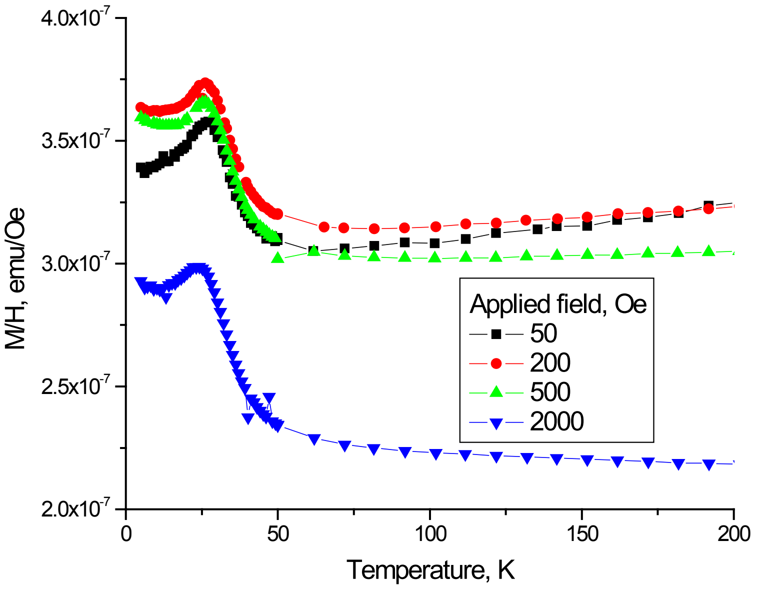

Figure 2.6: Magnetization measurements for CVD grown Pb-catlysed SWNTs show a change in susceptibility ~20 K.

Clemson team has also explored the synthesis of single, bi-, and few-layer graphene sheets. We utilized micro-Raman spectroscopy and XPS to study various bonding configurations possible in N-doped graphene. Previously, dopant induced changes in the Fermi velocity were observed to result in a effectively downshifted (up-shifted) Raman peak below the G' band for *n*-doped (*p*-doped) single-walled carbon nanotubes. However, in case of N-doped graphene, we found that several Raman features can vary depending upon both the dopant concentration and its bonding environment. For instance, only the pyridinic/pyrrolic dopants were observed to result in intense *D* & *D'* bands with a concomitant downshift in the *G'* band frequency. In Ref. 12, we correlated XPS measurements with Raman spectroscopy to elucidate the effects of dopant bonding configuration on the electronic and vibrational properties of bilayer graphene. Our results showed that graphitic dopants are more suitable for superconducting application as they induce least amount of disorder.

Partial **Summary and Conclusion on Superconductivity Search in Carbon nanotubes and 1-D nanowires**

The UTD-Clemson-Yale team concentrated efforts of years 2010-2013 on the search for superconductivity in several nanostructured systems: various nanotubes (SWCNT, MWCNT, Boron nanotubes (BNT), nanodiamond, graphene and HOPG) upon various types of doping by p-type (Boron) and n-type doping: (As, P, S) by ion implantation and other methods: Progress in this search can be summarized as following:

1. We have shown theoretically that in bundles of undoped pristine SWCNTs, containing 1/3 of metallic tubes Tc is suppressed to observed 0.5 K by inverse proximity effect by semiconducting component, and we have found in a simple mean field theoretical approach that Tc should increase several times in 100 % metallic SWCNT bundles [1].
2. To increase further Tc in SWCNTs we checked experimentally the suggested effect of suppressing inverse proximity effect in mixed SWCNT (of composites of metallic and semiconducting) bundles. Since pure bundles of Semiconducting single wall SWCNT, are now available by separating pure (>99% purity) semiconducting S-SWCNT from pure metallic M-SWCNT, the Tc is expected to grow significantly in S-SWCNTs due to more favorable for doping position of singularities in density of states, as compared to M-SWCNTs Examples of pure S-SWCNT doping have been demonstrated, which show promises for higher Tc. For now Tc ~ 6K is detected by LFMA in K- and B-doped Semiconducting SWCNTs, but not in Metallic SWCNTs. . Our team members (A. Rao, J. Haruyama [1, 2]) have already obtained Tc=15-19 K in boron doped mixed SWCNTs [3,4]. This results can not be reproduced by our doping methods.
3. Most importantly the UTD team has observed and recently confirmed SC-ing type R(T) behavior in oriented MWCNTs sheets, interconnected by T-junctions into 3-D networks [3]. However some samples showed negative R(T) puzzle at lowest T<5 K. We will discuss the possible origin of this artifact and describe the “cross-interconnected” CNT networks, in which this artifact-effect can be suppressed. Superconducting type correlations are observed starting around Tc~40-60 K in Boron doped (by ion implantation) MWCNTs sheets. This B-MWCNT samples are characterized by SQUID, low-field microwave absorption LFMA combined with ESR and ex-situ by SEM, AFM, transport measurements at T>2K. However the LFMA was not of SC-ing type Fundamental problem with achieving superconducting phase in quasi-one-dimensional systems, such as CNTs, is the necessity of 3-dimensional coherence, for which UTD team have developed several methods: formation of 3-D networks of T-junction interconnected MWCNT bundles by proper CVD synthesis conditions, infiltration by non-SC metals (Ag, Au) for proximity effect (suggested to suppress phase fluctuations) and also spark plasma sintering (SPS) of CNTs (by Clemson sub-team). In such interconnected

MWCNT dense 3-D networks properly doped by boron by ion implantation the possible SC-ing type with Tc ~ 20-40 K has been detected in transport measurements but not confirmed by LFMA (though at lower T) this data needs further confirmation though by SQUID and ac-magnetometry. And thus SC-ty is still not confirmed in present.

4. We have developed methods to create light-weight superconducting wires and cables by co-spinning non-superconducting MWCNT yarns with various superconducting components. We have demonstrated new method for making wires of nanocomposites of MgB2 with MWCNT yarns [5] and YBCO with MWCNT sheets [5].
5. The new method of laser assisted CVD of boron coating on MWCNTs has been developed, permitting formation of MgB2 upon reaction with Mg vapor. The resulting superconducting wire is being now optimized gotr higher critical currents.
6. We have performed B-doping and K-doping of separated SWCNTs" semiconducting and metallic and found superconducting low-field microwave absorption LFMA of SC-ing type with Tc at 6 K in semiconducting SWCNts, while metallic SWCNTs do not show signs of SC-ty.

Methods and Equipment for Achieving New Objectives in 2-D and 1-D systems:

1.1 Pulsed Laser Deposition (PLD): The PLD method is one of the most effective techniques for controlled heteroatomic doping in carbon nanostructures. Previously, Clemson team has succeeded in producing B-doped SWNTs by ablating boron and metal catalyst impregnated carbon target with Nd-YAG laser [4]. In the PLD process for producing B-doped SWNTs, a target is placed in a quartz tube and heated to 1100 °C in Ar atmosphere at a pressure of ~500 mTorr. A Nd:YAG laser (1064 nm, 10Hz) is then used to ablate the target. The targets contain graphitic carbon, Co:Ni catalyst (0.5:0.5 at.%) and elemental boron. In this project, Clemson team prepared 0.5-3.5 at% B-doped SWNTs using the PLD method and characterized them using electron microscopy, Raman and X-ray photoelectron spectroscopy (see Fig. 2). The list of all the PLD samples sent to UTD team is catalogued in the attached excel sheet.

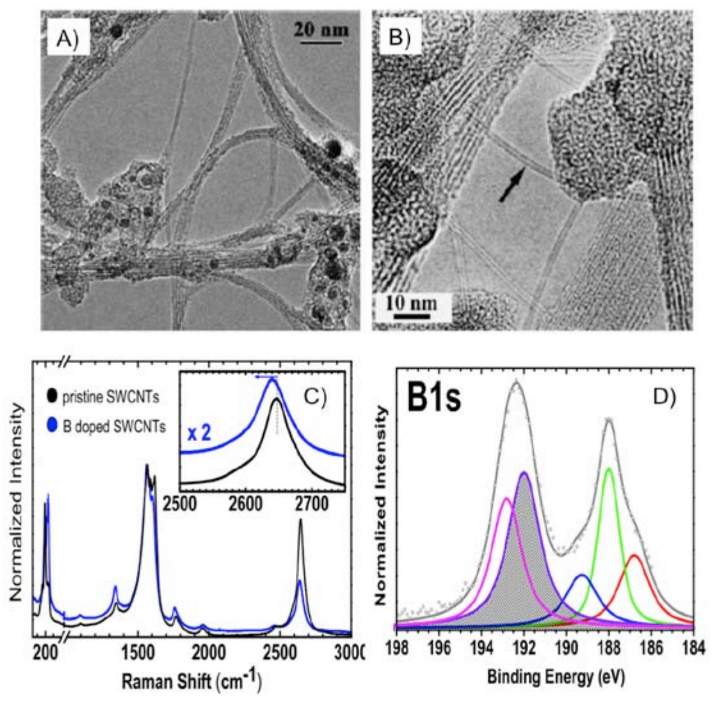

Figure 2. 7: Typical transmission electron micrographs of PLD grown B-doped SWNTs. C) The Raman spectrum of B-doped SWNTs clearly down-shifted with respect to pristine SWNTs due to electron phonon renormalization [5]. D) XPS spectrum of B-doped SWNTs shows the 1.5 at% nominal B-doped SWNTs contain 0.3 at% of boron in SWNT lattice as substitutional dopant.

Previously, Haruyama's group observed an evident drop in normalized magnetization in 1.5 at% B-doped SWNT bundles is below 12 K (see Fig. 3). Although the nominal doping ratio in these samples is known, the actual doping ratio could not be determined directly using Raman spectroscopy. The fact that B substitution in the SWNT lattice is not necessarily uniform makes it challenging to quantify the amount and bonding environments of boron. Nonetheless, we have utilized synchrotron based XPS to determine B-doping levels in superconducting 1.5 at % B-doped SWNTs with sub-atomic precision. As shown Fig. 2D, our XPS results [6] indicated that ~0.3 at% substitutional boron is present in superconducting SWNT bundles. One of the disadvantages of PLD method is that an increase in the elemental boron content in the target can significantly alter the thermodynamics of the SWNT growth process inhibiting SWNT formation. Therefore, other techniques are much needed in order to increase the amount of dopant in B-doped SWNTs. For this reason, we have developed novel post-synthesis process to dope SWNTs, as described in the proceeding section.

Part 3. SUPERCONDUCTIVITY in IRON PNICTIDES: Search for higher Tc phases

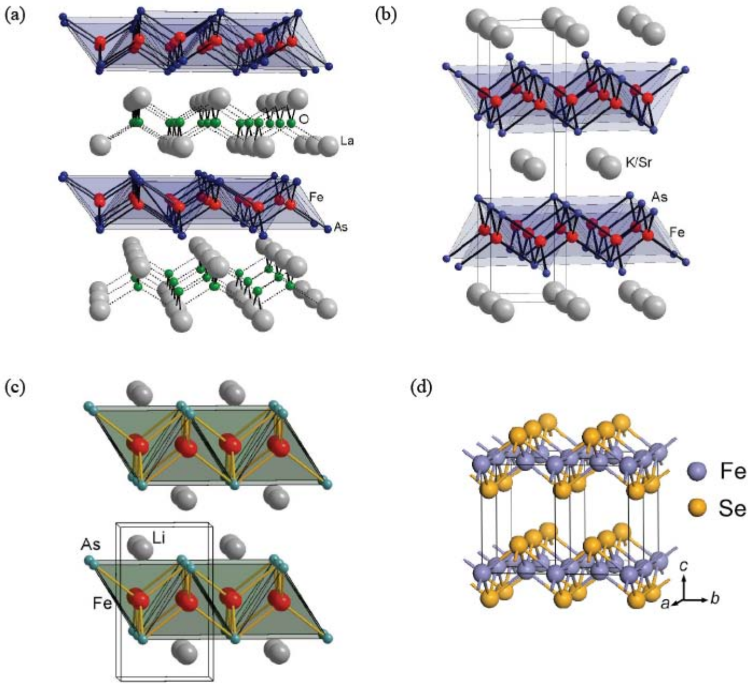

Figure 3.2: Various pnictide and chalcogenide structures. (a) 1111, (b) 122, (c) 111, (d) 11 [iv]

3.2. Synthesis of iron pnictide Ba(Fe$_{1-X}$Co$_X$)$_2$As$_2$ and CNT Composites.

A portion of the research during N. Cornell's eight week stay at Zhejiang University in Hangzhou, China involved the synthesis of iron pnictide superconducting compounds with the intention of measuring their properties as well as refinements in order to improve their utility. The length of time necessary for successful synthesis of these compounds required focus on one compound primarily. We began with Ba(Fe$_{1-X}$Co$_X$)$_2$As$_2$, an iron pnictide that exhibits a superconducting transition above 24K when doped to X=0.09.

Like other superconducting pnictides, $Ba(Fe_{0.91}Co_{0.09})_2As_2$, can be synthesized through solid-state reaction methods to form polycrystalline samples, or single crystals through the flux method. The first task was to synthesize the base compounds of FeAs and CoAs by combining the parent elements in the correct stoichiometric ratios, grinding them into uniform powders, and sealing them inside evacuated quartz tubes. Then the sealed tubes were interred inside an electric furnace and heated to temperatures of 900°C and held for 24 hours.

samples followed the same procedure combining the previously synthesized compounds together in the proper ratios before being likewise ground into powders. Next the samples were pressed into pellets and placed within an alumina crucible inside a sealed and evacuated quartz tube before heating to 900°C for 24 hours. Early synthesis of polycrystalline samples proved to be too brittle unless the barium was first reacted with arsenic to make BaAs before being combined with the FeAs, CoAs, and Fe to form the proper structure for the pnictide. Additionally, polycrystalline samples need to be reground and reheated multiple times in order to become sufficiently homogeneous.

Single crystal samples were grown from the flux combining barium, FeAs, and CoAs inside an alumina crucible and quartz tube. The furnace required a much more controlled sequence than the polycrystalline synthesis, ramping up to hold at 700°C for 10 hours before increasing to 1100°C and holding for 5 hours. Upon cooling back to 900°C over 50 hours, $Ba(Fe_{0.91}Co_{0.09})_2As_2$ crystals form within the flux. Adjustments to the rate at which the furnace allowed the samples to cool increased the size and frequency of the grown single crystal pnictides.

Transport measurements on the polycrystalline and single crystal samples of the iron pnictide can be seen in figures 3.4 and 3.5, respectively. A clear transition into the superconducting state can be seen in both, with a T_c^{zero} of 24.4 K in the single crystal sample. Further measurements were carried out in a Quantum Design MPMS on the magnetic susceptibility. Figure 3.6 shows the field cooled vs zero field cooled curves for fields up to 1 Tesla in polycrystalline $Ba(Fe_{0.91}Co_{0.09})_2As_2$, confirming the material's superconducting behavior.

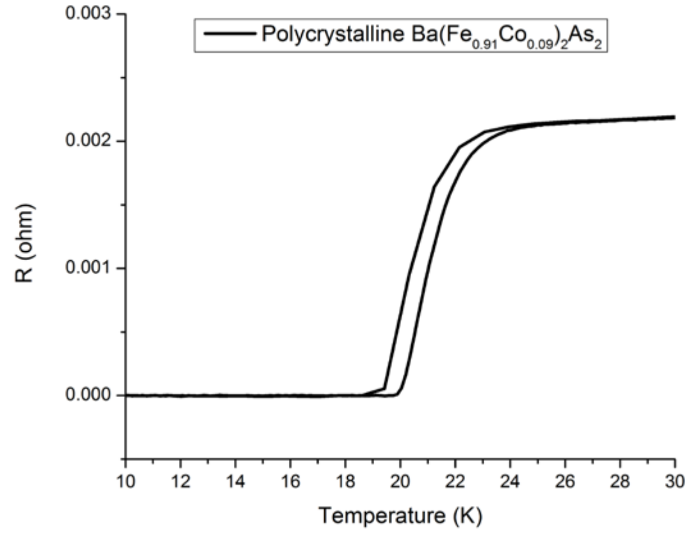

Figure 3.4 Superconducting transition in polycrystalline $Ba(Fe_{0.91}Co_{0.09})_2As_2$

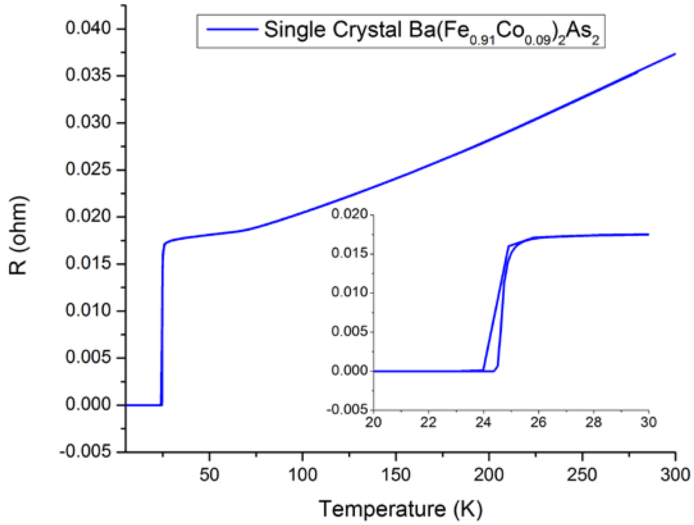

Figure 3.5 Superconducting transition in single crystal Ba(Fe$_{0.91}$Co$_{0.09}$)$_2$As$_2$

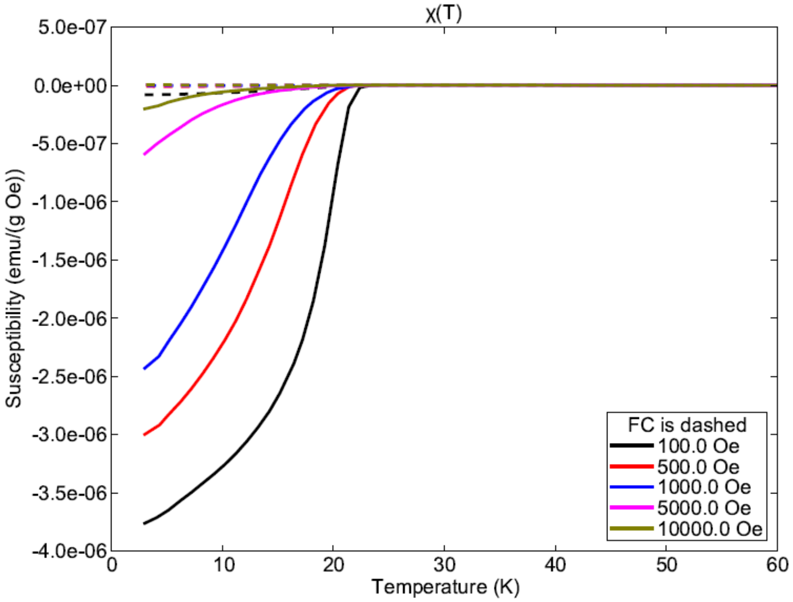

2. *Figure 3.6 SQUID measurements of susceptibility in polycrystalline Ba(Fe$_{0.91}$Co$_{0.09}$)$_2$As$_2$*

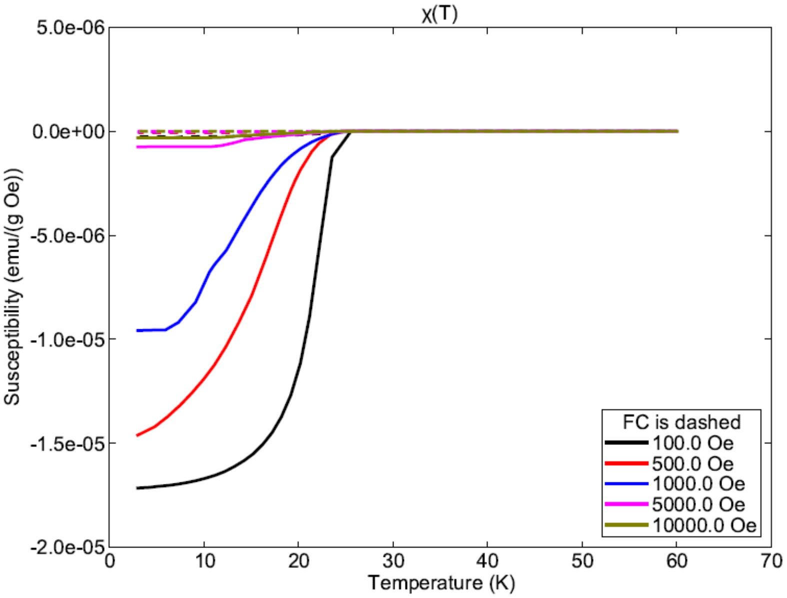

Figure 3.7 SQUID measurement of a composite $Ba(Fe_{0.91}Co_{0.09})_2As_2$ *and carbon nanotube yarn showing the superconducting behavior of the included iron pnictide.*

Attempts were made to combine polycrystalline $Ba(Fe_{0.91}Co_{0.09})_2As_2$ with carbon nanotubes with the aim of creating a superconducting yarn that is light, strong, and easily fabricated. Highly spinnable forests of CNT were drawn into sheets before having fine ground powder of $Ba(Fe_{0.91}Co_{0.09})_2As_2$ deposited on the surface before being twisted into yarns before annealing. Under the strain of twisting, even separate particles on the surface of the nanotube sheet are confined inside the yarn at micrometer or nanometer scales. The tests with some of the first grown polycrystalline Ba122 pnictide samples were successfully spun into yarns, but were unable to replicate the superconducting transition in transport measurements of resistivity. Measurements of the magnetic susceptibility in the MPMS of the pnictide CNT composite as seen in figure 3.7 show that the robust grains of $Ba(Fe_{0.91}Co_{0.09})_2As_2$ still remain superconducting nevertheless, and as such continues to be a viable candidate for further superconducting wire research.

3.3. Study of 122 and 112 structures studied by Low Field Microwave Absorption.

3.3.1. Comparison of Pr-doped Ca 122 and Ca 112 pnictides by Microwave LFMA spectroscopy

Praseodymium doped $CaFe_2As_2$ (122 structure) and $CaFeAs_2$ (112 structure) are characterized by modulated Low Magnetic Field Microwave Absorption (LFMA) spectrsocopy. In both (Pr,Ca)122 and (Pr,Ca)112 structures, a strong hysteretic LFMA is found, with a T_{c1} of ~22 K and ~20 K, respectively. However, in (Pr,Ca)122, measurements also show an unusual Narrow Peak (NP) LFMA signal appearing at higher temperatures, above the lower T_{c1} superconducting state until a T_{c2} of 49 K. This NP LFMA is associated with interfacial superconductivity, which has been found earlier in (Pr,Ca) 122 by highly anisotropic magnetization measurements which showed very low critical field Hc1~1-3 G, comparable with the width of NP found here. The absence of NP in Pr-doped Ca 112 correlates with the absence of higher Tc2 in this newly discovered crystal structure, which has chains of pure As between FeAs planes. These results give useful information about the microwave signatures of interfacial superconductivity present in the (Pr,Ca)122 system, and may form a roadmap towards a stabilized high temperature superconducting phase in pnictides.

Among the recently discovered class of doped pnictide superconductors, the so-called 122 systems ($M\text{Fe}_2\text{As}_2$ with M an element of valency 1 or 2 {Sasmal:2008dz}) have attracted significant interest {Lv:2011db, Kim:2009dg, Chu:2009ks, Rotter:2008hl, Sasmal:2008dz}. In particular, superconductivity in the studied Ca122 pnictide has been found to be significantly different from a seemingly similar system, Ca112 {Yakita:2014js, Katayama:2013cc}. The maximum T_c in reported 122 systems is only 38 K {Rotter:2008hl, Sasmal:2008dz}; however, a recent independent observation of a high temperature phase, with a significantly higher T_c (47-49 K), in Pr-doped Ca122 {Lv:2011db} opens a new perspective to search for even higher critical temperatures. The reported high temperature phase has an exceedingly small volume fraction and is easily suppressed by small magnetic field. For this reason, combined with the absence of the characteristic specific heat anomaly anywhere between 2 K and 49 K {Lv:2011db}, and the high magnetic anisotropy below T_c {Wei:2013tq}, it is thought that the high temperature phase is formed from interfaces present in the crystal. This "interfacial superconductivity" may in the future be improved or stabilized {Kudo:2013fk}, leading the way for high temperature superconducting (HTSC) pnictides.

In this paper, we report results of modulated low magnetic field microwave absorption (LFMA), a powerful technique in examining the microscopic behavior of each system below their respective T_c. The (Pr,Ca)122 system exhibits an unusual signal, with a very narrow absorption peak (NP) centered on zero field, between T_c = 49 K and a transition at around T = 30 K. This type of signal is not observed in the (Pr,Ca)112 pnictides.

(Pr,Ca)122 and (Pr,Ca)112 single crystals were grown from the self-flux method, as described previously by Lv, et al {Lv:2011db}. For LFMA measurements, the 122 crystals were affixed to a quartz capillary tube and sealed inside a 4mm EPR ampoule (Wilmad LabGlass) at ~10^{-6} torr. The crystals were fixed in such a way that their orientation relative to the measurement apparatus could be controlled. LFMA was performed inside a standard electron paramagnetic resonance (EPR) spectrometer (Bruker EMX), fitted with an X-band (9.8 GHz) microwave source and TE_{102} cavity. Temperature control is achieved by a ColdEdge cryogen-free cryostat, capable of reaching T = 4 K by a flow of helium transfer gas, which is passed over a heat exchanger attached to a Sumitomo compressor/cold head before being passed by the sample.

The fields inside of the cavity are those shown in Figure 1. These fields are provided by a large pair of Helmholtz Coils (for H_0), a pair of modulation coils within the cavity, and the microwave radiation itself {Lund:2011up}. Thus the sample is exposed to three magnetic fields: in the x direction, a slowly sweeping (2.5 G/s) magnetic field H_0 (generally ramping between –50 and +50 G) and a modulation field of intensity on the order of 1 G and sinusoidal oscillation with frequency of 100 MHz; and in the z direction, a magnetic field from the standing microwaves. The static and modulation fields form vortices or fluxons within a Type-II superconducting material, which are oscillated about their pinning centers by the microwave currents {Talanov:2005ww}. The oscillations absorb a portion of the microwave energy, causing a signal from the device {Stankowski:2006ux}.

Magnetization measurements are performed in a Quantum Design MPMS.

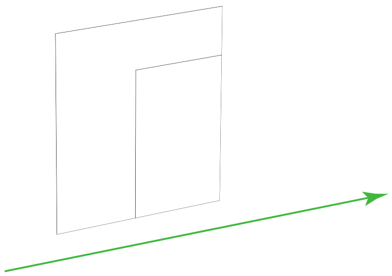

Figure 3.8: Orientation of magnetic fields inside the TE_{102} resonant cavity of the EPR device, which is used for LFMA measurements. The sample location is denoted by a black circle.

The typical LFMA spectra observed for (Pr,Ca)122, with H_{mw} || *ab* planes, upon zero field cooling of a sample to 4 K and increasing T slowly are shown in Figure 2(a) and Figure 2(b), where H_0 || *ab* planes or *c* axis of the crystal, respectively. An increased modulation field can bring out smaller features with less noise, at the expense of possible loss of detail. An increased microwave power increases the screening currents responsible for oscillations about the fluxon's pinning centers. {Talanov:2005ww, Shaposhnikova:2007dk}

LFMA shows two distinct shapes in temperature regions $T < 30$ K and $T > 30$ K. Below 30 K, we see relatively typical LFMA signals for a superconductor with both flux trapping and Josephson decoupling {Shaposhnikova:2003hr}. Intensity and hysteresis width decrease with increasing temperature. Above 30 K, the signal changes dramatically. Hysteresis nearly vanishes, but a strong, narrow zero field peak, or NP, appears similar to that arising from Josephson Junction (JJ) decoupling found earlier in HTSC {Stankowski:2006ux}. The field width of this signal is only ~2 G. It is worth noting that the width of the NP is also observed in $M(H)$ curves, in the $T > 30$ K regime, as the value of H_{c1}, the minimum of the characteristic "butterfly" curve of superconductivity (discussed below).

We may compare these results with those in Figure 2(c,d), which differ only by a rotation of the sample about the *z* axis, that is, where H_0 || *c* axis of the crystal, but still with H_{mw} || *ab* planes. Qualitatively the behavior is similar, with a transition from the hysteretic LFMA of the low temperature phase to the NP signal of the high temperature phase. However, the signal intensity is higher (which may be partially due to the demagnetizing factor), and the NP signal appears at a lower temperature than in the previous case. A similarly large anisotropy, supporting the hypothesis of interfaces, is also observed in magnetic measurements {Lv:2013tb}.

The temperature dependence of intensity, as shown in Figure 3, reveals just how dramaticly the NP signal appears in measurements. The high temperature phase manifests as a sharp increase in peak-to-peak signal intensity, without a corresponding increase in the hysteretic signal.

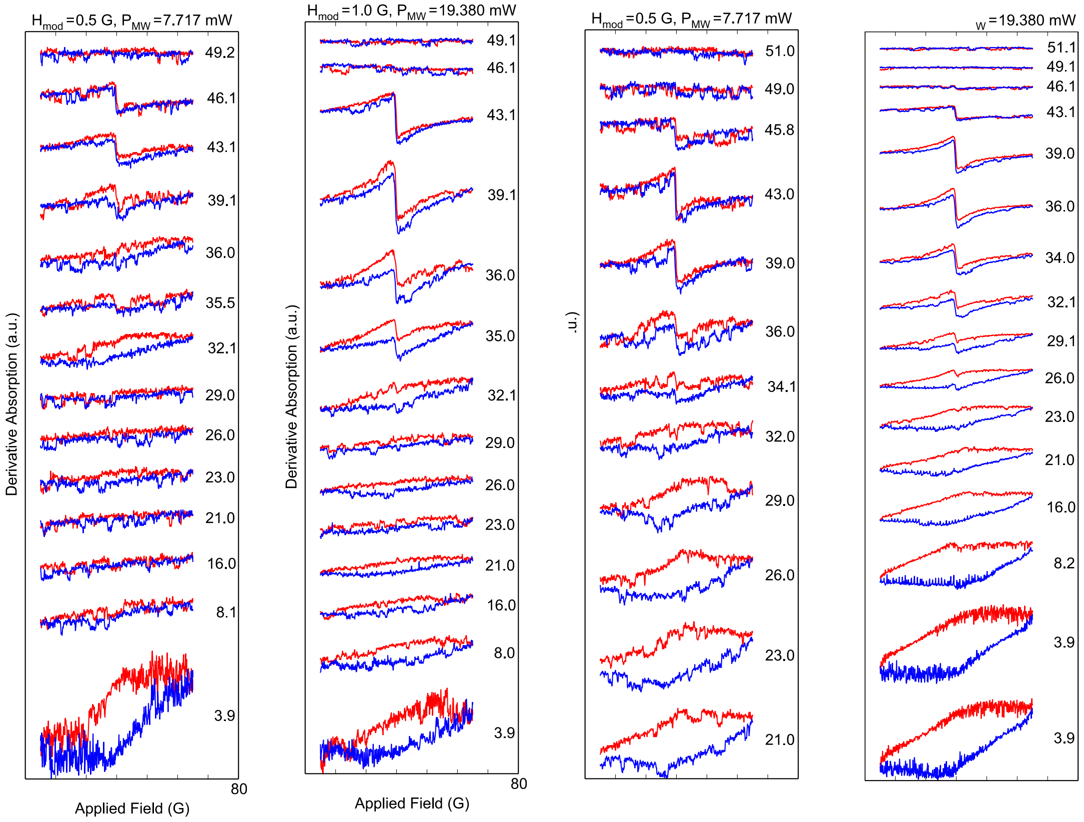

(a) (b) (c) (d)

Figure 3.9: LFMA spectra of (Pr,Ca)122 sample, with the orientation fixed such that $H_{mw} \parallel ab$ planes; (a,b) $H_0 \parallel ab$ planes of the crystal, and (c,d) $H_0 \parallel c$ axis of the crystal. Each stack of curves represents a specific combination of microwave power and sinusiodal modulation field amplitude. The number to the right of each curve is the temperature of measurement in Kelvin. A dramatic transition is clearly seen in the vicinity of 30 K. Below that transition, the LFMA exhibits a purely hysteretic signal, from trapped flux within the superconducting state, while above the transition, a narrow field width absorption peak (NP) appears in the signal, with the absence of any hysteresis, and vanishes at ~49 K, the temperature observed by other methods as the onset of "interfacial superconductivity." We note a general increase in signal strength for (c,d) (partially due to demagnetizing factor), and a decrease in the onset temperature of the NP signal. All curves (a-d) have a clockwise hysteresis.

We may further analyze this signal by fitting the temperature dependence of LFMA intensity to the Josephson junction model of Nebendahl {Nebendahl:1993wz}. The model states that LFMA intensity, as a function of temperature, should fit an equation of the form:

$$I_{pp}(T) = a_0 \frac{1}{\left(1+\eta_0\left(1-T/T_c\right)^{2\alpha}\right)^{3/2}} \left(1-\frac{T}{T_c}\right)^{2\alpha} \tag{3.1}$$

where a_0, η_0, T_c, and α are determined from curve fitting. The α parameter is particularly important, as it indicates the type of Josephson junctions (JJ) present: $\alpha = 1$ for SIS-type junctions (superconductor-insulator-superconductor), $\alpha = 2$ for SNS-type junctions (superconductor-normal metal-superconductor).

Constraining $1 \leq \alpha \leq 2$, and assuming that the NP feature is due to JJs, we can fit the $H \parallel ab$ curve with $T_c = 48.3 \pm 0.6$ K, $\alpha = 2$, $\eta_0 = 1.23 \times 10^3$, and $a_0 = 5.04 \times 10^5$. ($H \parallel c$ gives similar fitting coefficients.) Therefore, not only is the predicted T_c of 49 K confirmed, but the behavior of the high temperature superconducting phase is determined to be from SNS-type Josephson Junctions.

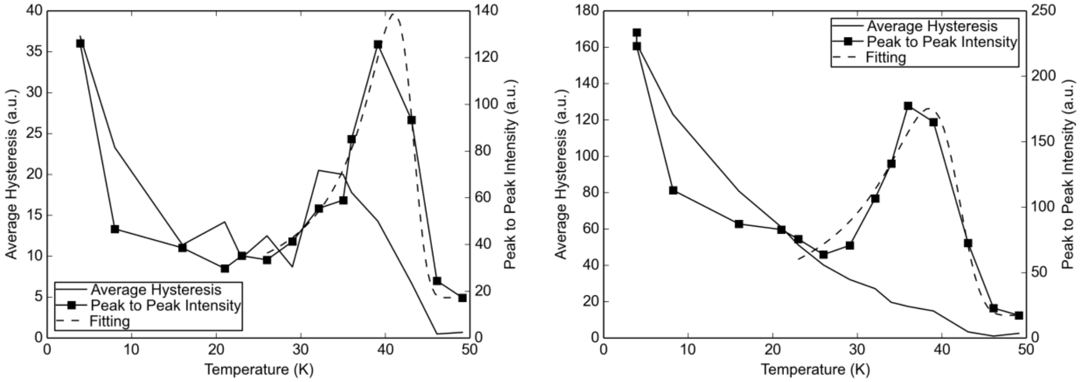

(a) (b)

Figure 3.10: Intensity of hysteresis (solid) and hysteresis+NP (squares) versus temperature, where $H_{\mathrm{mod}} = 1$ G, $P_{mw} = 19.43$ mW, for orientation (a) $H_0 \parallel ab$, and (b) $H_0 \parallel c$. The dashed line is the fit to the model of Nebendahl (Eq. 1). The appearance of the NP is clearly visible as a spike in the total intensity curve which does not appear in the hysteresis intensity dependence. The split in signals occurs at 26 K for (b), but does not occur until 35 K in (a).

The (Pr,Ca)112 system has a substantially different behavior in LFMA measurements. Typical LFMA spectra observed upon zero field cooling of a sample to 4 K and increasing T slowly are shown in Figure 4. We observe two noticeable differences between the 112 and 122 systems. Firstly, the (Pr,Ca)112 results show no indication of a higher temperature NP-type signal, only the hysteretic signal of the low temperature phase below 23 K. Figure 5(a) shows the falloff of intensity with temperature, and no additional spike appearing from a high temperature phase NP-type signal. (This behavior is correlated by magnetization in Figure 5(b); the zero field cooled and field cooled curves split above 40 K for (Pr,Ca)122, but remain together until close to 20 K for the (Pr,Ca)112.) Secondly, the strength of the signal decreases dramatically with increasing microwave power (see inset of Figure 5(a)), an effect which was not observed in the 122 case. In fact, the strength of the LFMA spectra for (Pr,Ca)122 increases with microwave power. The magnetic field component of the microwave radiation has a square root dependence on microwave power, and can be calculated {Anonymous:tr} to be $B_{mw} = 2.73$ G at 15.43 mW, where the LFMA signal vanishes for all temperatures below T_c. Further investigation is required to understand this unusual behavior, and the significance of this $H_{mw} \sim 3$ G transition with (Pr,Ca)112.

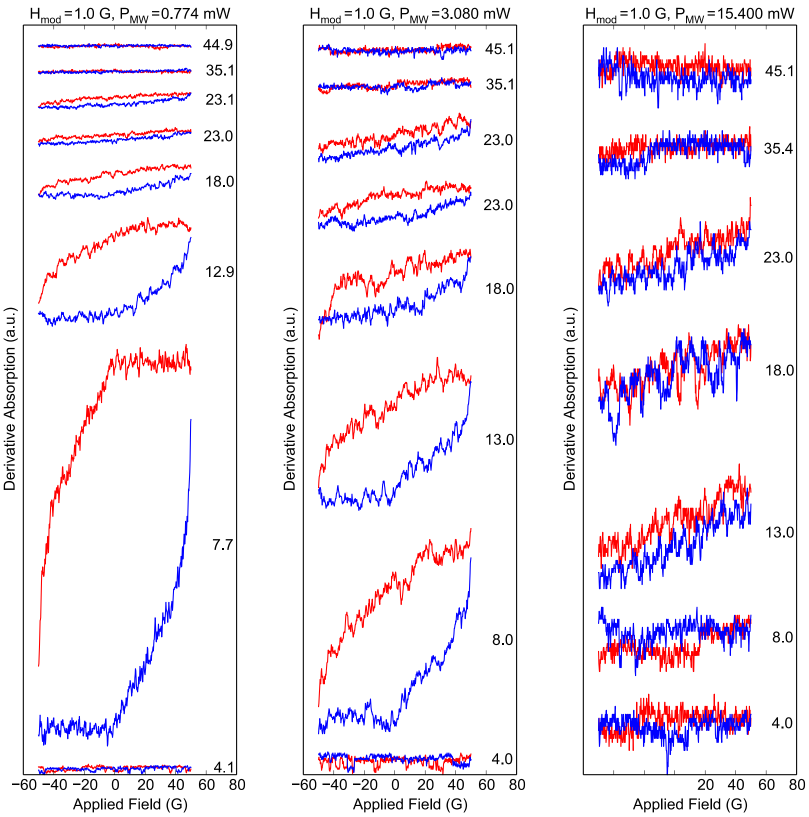

Figure 3.11: LFMA scans of (Pr,Ca)112 sample for various microwave powers, and hence magnetic fields. (All scans performed with modulation amplitude of 1 G.) Increased microwave power causes a rapid decrease in LFMA hysteresis. All curves have a clockwise hysteresis.

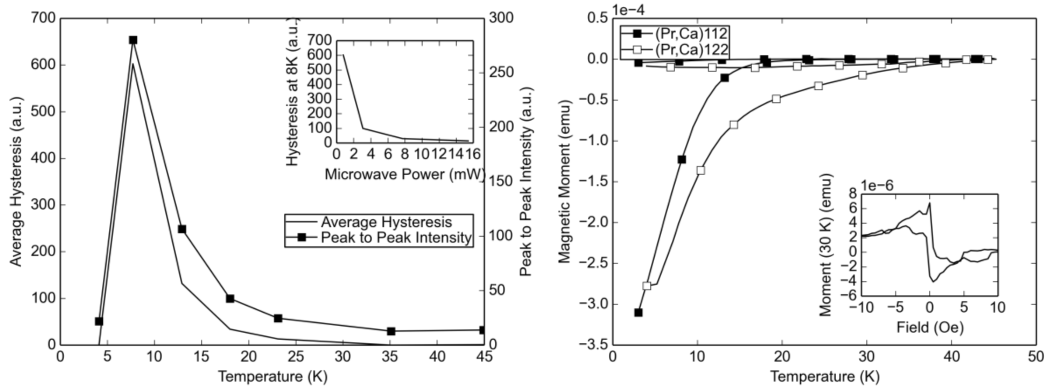

(a) (b)

Figure 3.12: (a) Main plot: dependence of hysteresis and peak-to-peak intensity on temperature for (Pr,Ca)112 with H_{mod} = 1 G, P_{mw} = 0.774 mW. We note the absence of any high temperature phase appearing in either curve. Inset: Strength of hysteresis at 8K, with H_{mod} = 1 G, as a function of applied microwave power. (b) Main plot: Zero field cooled (lower) and field cooled (upper) magnetization data with an applied field of 10 Oe, comparing (Pr,Ca)122 with (Pr,Ca)112. We note that the 122 pnictide ZFC data deviates from the FC data above 40 K, while the 112 pnictide ZFC does not deviate from FC until near 20 K. Inset: $M(H)$ measurement for (Pr,Ca)122 at 30 K, showing the same small H_{c1} as LFMA. (Counter-clockwise hysteresis.)

In conclusion we showed that Low-field microwave absorption LFMA is a powerful and ultra-sensitive technique for characterizing complex, multiphase superconducting materials such as the (Pr,Ca)122 and (Pr,Ca)112 single crystalline systems. We have demonstrated the ability to detect small volume fraction of lower Tc1 by hysteretic LFMA in SC phases in both Pr-doped Ca 112 and 122 systems, and even smaller volumes of "interfacial" phases of the higher T_{c2} phase in (Pr,Ca)122. Additionally, we have shown that the 122 and 112 systems do not behave similarly near $T1_c$, a fact which is only known from the complete absence of the narrow peak signal in the Ca 112 samples. Additional analysis will be required in order to fully understand the complicated nature of multiphase superconductivity in these electronically doped Ca 122 and 112 pnictides.

3.4. Re-entrant behavior of $EuFe_2(As_{0.73}P_{0.27})_2$

Superconductivity and ferromagnetism are both states into which a substance can enter upon decreasing temperature. In most situations these states are in opposition to each other and the presence of one either prevents or removes the other. However, it has been shown that GdCeRuSrCuO exhibits coexistence of bulk superconductivity ($T_c = 42K$) in the magnetic state ($T_N = 180K$).1 In addition Felner et al. shows the magnetic state to be confined to the Ru site and suggests that the STM data shows the samples to be composed of a single phase and not a mixture of magnetic and superconducting phases. Coexistence was also found in the similar compound of RuSrGdCuO2 where superconductivity was observed in bulk transport measurements of the resistivity within the persisting ferromagnetic phase. Recently, there has been more work on another class of compounds possessing iron that can be doped to become superconducting, and in some cases coexist with internal magnetic states as well.

Superconductivity can be suppressed by a magnetic field to varying degrees depending on the specific material being tested. This is normally evidenced by a shifting of T_c to lower temperatures under an applied magnetic field. However, if the material in question has a magnetic ordering that is temperature dependent, and occurs both below and near the superconducting transition temperature, the sudden emergence of the internal magnetic field can suppress the superconducting phase enough that it results in an increase in the resistance below T_c. The internal field stabilizes quickly below T_M, and as the temperature decreases, the superconducting phase continues to increase to the point where it once again dominates the internal field and the resistance will decrease with temperature down to zero.

Pnictides of the 122 variety contain Fe_2As_2 layers with either Ca, Sr, Ba, or Eu. They are interesting both for their lack of oxygen content and being rich in iron. Superconductivity has been achieved in this system by both charge carrier doping, and suppression of the spin density wave (SDW) transition from the long range Fe order through applied pressure.

In $SrFe_2As_2$, studies were able to show a superconducting transition with $T_c = 19.5$ K when the Fe sites were doped by Co.3 They go on to conclude that this superconducting phase coexists with magnetism (SDW) that occurs higher than T_c, around 120K.

In $BaFe_2As_2$, doping by Co also showed the emergence of superconductivity, including within the SDW state for lower doping levels.4 Additionally, there was a splitting of the SDW transition upon increasing doping levels until the transition fell below T_c. The Co doping in Ba-122 and Sr-122 both provides electrons and suppresses the long range SDW in Fe.

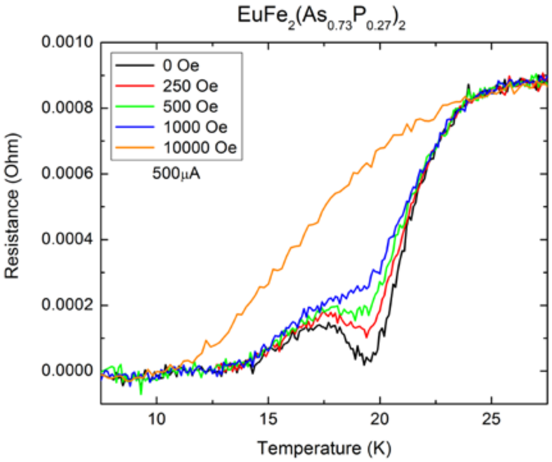

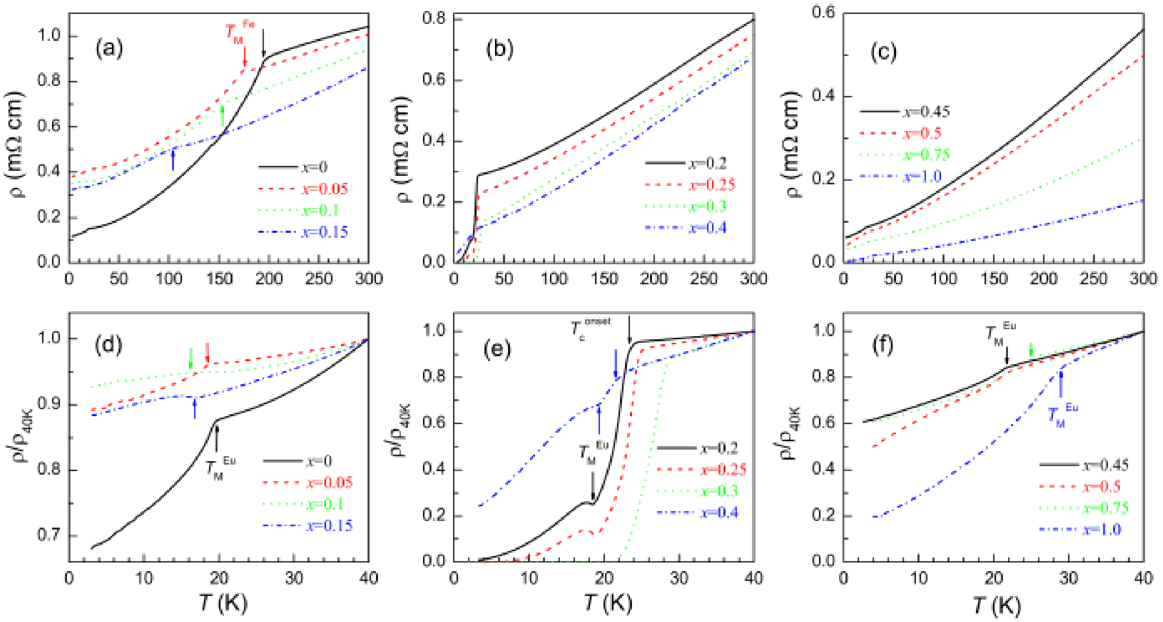

3.5. Re-entrant Superconductivity in $EuFe_2(As_{1-x}P_x)_2$

$EuFe_2As_2$ as a parent pnictide shows superconductivity upon doping into the FeAs layers, as well as long range magnetic ordering in the Eu sublattice. Without doping, the Fe sites also undergo antiferromagnetic ordering. Upon substitutional doping of the As sites with P, the FeP bonds shrink the lattice applying a chemical compression.5 This has an effect on the Eu^{2+}, changing some from divalent to trivalent Eu^{3+}. The reduced lattice spacing also has the effect of increasing the interlayer RKKY coupling and encouraging Eu spins to a ferromagnetic ordering. The effects of increasing doping levels are shown below in the data from Guanghan Cao[6]:

Those polycrystalline samples were synthesized via solid-state reaction of EuAs, Fe_2As, and Fe_2P. Samples were ground, mixed, and pressed into pellets before annealing at 1273K for 20 hours. Superconductivity occurs in $EuFe_2(As_{1-x}P_x)_2$ starting with a doping level of x = 0.2. Additionally, there is a shoulder in the resistance below T_C that occurs at T_M for the Eu. The magnetic ordering at first suppresses the superconducting transition just below T_M, as seen by an increase in the resistance, before the superconducting transition dominates again at lower T. It is worth noting that the competition between superconducting and ferromagnetic phases are uniquely evident in the Eu-122 pnictide due to the fact that T_c and T_M transitions are within 5K of each other.

Additional samples of $EuFe_2(As_{0.73}P_{0.27})_2$ were measured in a Quantum Design physical property measurement system. R(T) data shown below:

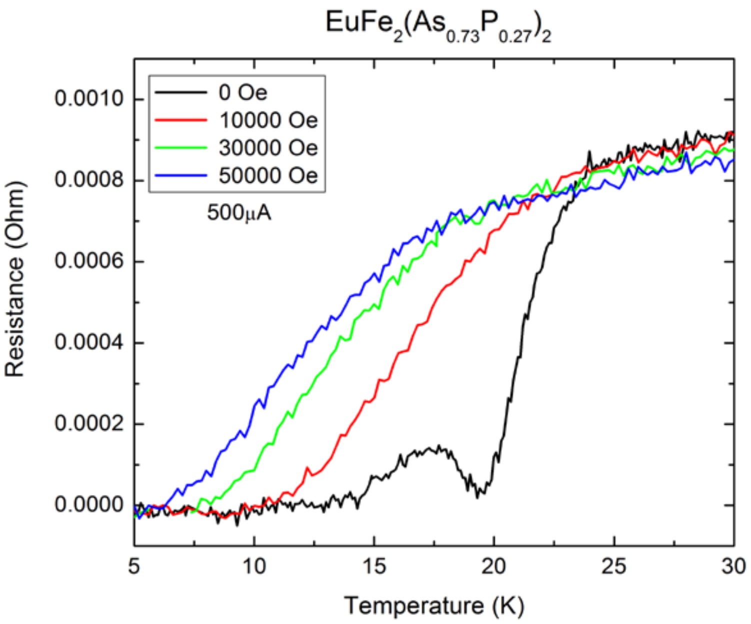

In this doping level, similar to those shown above, there is an increase in the resistance below the magnetic transition T_M. The onset of superconductivity is more rapid than in previous samples, reaching zero resistance before its re-entrance. Interestingly, upon the application of increasing magnetic fields, the onset of T_c does not decrease or change, only the magnitude of the resistance drop decreases until it vanishes. Once the resistance shoulder has disappeared, further increases to the magnetic field now serve to decrease T_c as expected.

Part 4. SUPERCONDUCTIVITY IN LAYERED IRON CHALCOGENIDES: FeSe and FeSeTe.

4.1. Overview of FeSe and FeTe Chalcogenide Synthesis and Properties

Type-11 iron based superconducting materials, as well as their type-122 siblings, possess a layered structure with an Fe square plane coordinated with either a pnictogen or chalcogen element.[v] Iron chalcogenides of the 11 variety in general exhibit a high tolerance for magnetic fields while in the superconducting state, evidenced by a very gradual decrease in the transition temperature with applied field. This makes them greatly sought after for applications involving high-fields such as superconducting magnet energy storage for which they exceed the field resistance of current niobium-based superconductors.[vi]

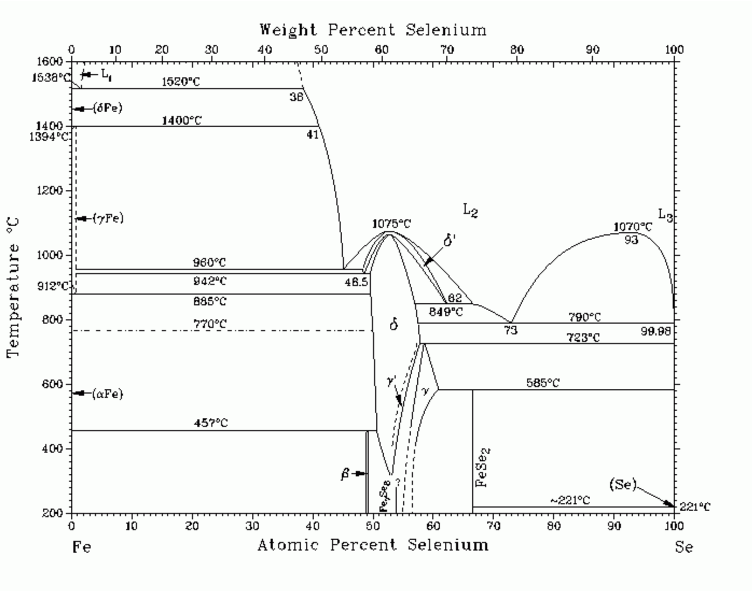

Figure 4.1: Phase diagram of Iron Selenide

Bulk crystals of FeSe exist in several phases: δ-FeSe, β-FeSe (sometimes referred to as α-FeSe) as well as Fe_3Se_4 can all be produced during synthesis (Fig.4.1). FeSe also exhibits a structural transition from tetragonal to orthorhombic with decreasing temperature. Upon substitutional doping of Te, the phase diagram of $FeSe_{1-x}Te_x$ reveals the suppression of the structural transition along with an increase in T_c to a maximum in the tetragonal phase at x=0.5.[vii] This crystal sublattice is similar to that found in the oxypnictides such as LaOFeAs. It is of note that pure FeSe does not show a clear superconducting transition unless it is selenium deficient, when it shows a T_c that reaches its peak at a 0.88 Se/Fe concentration.[viii]

4.2. Thin Films of FeSe, FeSeTe, and High Esitmated Hc2

FeTe does not show signs of superconductivity in the bulk, but when prepared and deposited as a thin film via pulsed laser deposition, it possesses a superconducting transition temperature above 12K.[ix] In addition, experiments performed on films synthesized in vacuum determined that oxygen can be crucial to the superconducting properties of $Fe_{1.08}Te:O_x$ films, where formerly it was considered detrimental.[x]

Nearly all thin films of iron chalcogenides are currently deposited though pulsed laser deposition (PLD), in which a stoichiometric sintered target is ablated by a laser in order to grow a well ordered film on a substrate. Deposition temperature, laser frequency, energy, and distance between the substrate and target are all variable parameters that can affect the quality of the grown thin films with both film thickness and deposition temperature having a strong effect on the superconducting transition.[xi]

Interesting as well, are the differences between the calculated $\mu_0 H_{c2}$ of the Werthamer–Helfand–Hohenberg (WHH) theory:

$$\mu_0 H_{c2}^{\mathrm{orb}}(0) = -0.69 T_c \left(\frac{\mathrm{d}\mu_0 H_{c2}}{\mathrm{d}T} \right) \Big|_{T_c}$$

And the zero temperature Pauli limiting field for weakly coupled superconductors given by

$$\mu_0 H_p(0) = 1.86 T_c \sqrt{1+\lambda_{so}} = 1.06 \Delta_0 \sqrt{1+\lambda_{so}},$$

where λ_{so} is the spin-orbit scattering constant. In polycrystalline samples of type-11 $FeSe_{0.25}Te_{0.75}$ the $\mathrm{d}\mu_0 H_{c2}/\mathrm{d}T$ was found to have large values that gave rise to estimated WHH orbital limited fields that exceeded both the Pauli and paramagnetically limited fields.[xii] It is common for the upper critical fields measured to deviate from the WHH model and become smaller than the estimate at low temperatures. In this case, the measured upper critical field $\mu_0 H_{c2}(0) \sim 40$ T still interestingly exceeds the Pauli limited field.

The objective for our research follows from the problems described above. We desire to develop a method for making better films of iron pnictides and chalcogenides, since thin films show increased critical field (H_c) ,critical current (J_c), and transition temperatures (T_c). Additionally, we want to better study the details of coexisting superconductivity and magnetism, and to clarify the role of magnetism in increased physical properties, such as T_c. Further refined measurements of transport, magnetic and microwave properties are also desired to better study very thin films and nanostructures such as rods or fibers. Finally, we want to create nanocomposite wires of iron pnictides and chalcogenides with CNT yarns for advanced applications.

4.3. PLD deposition of FeSeTe

Pulsed laser depositon (PPD) is a physical vapor deposition technique whereby a high-power laser beam is used to excite a target of the material to be deposited, This pulsed beam causes ablation of the surface material and subsequent generation of a plume of the target material that expands through the vacuum chamber before depositing as a thin film on the working substrate. Depositions can be carried out either in ultra high vacuum or with a background gas.
Factors that influence the deposition rate include laser energy, laser frequency, target material, distance from target to substrate, temperature of substrate, and pressure of the vacuum chamber. The $FeSe_{0.1}Te_{0.9}$ thin films were deposited at 400°C on single crystal STO (001) and glass substrates with a KrF excimer laser (Lambda Physik Compex Pro 205, $\lambda = 248$ nm, 5 Hz). The distance from target to substrate was kept at 4.5 cm. The growth rate of the $FeSe_{0.1}Te_{0.9}$ was around 0.5 Å/pulse. The laser power density was 3 J cm^{-2}. The base pressure for all the depositions was less than 1×10^{-6} Torr in vacuum.

4.4. Pulsed Plasma Deposition of Higher Tc Superconductors (system developed in UTD)

4.4.1. Pulsed Plasma Deposition of $FeSe_{0.1}Te_{0.9}$ Thin films

The method of pulsed plasma deposition (PPD) is a physical vapor deposition technique. It uses a high-voltage and high-current source of electrons to ablate solid targets. Pulses up to 20 kV and 2 kA lasting less than 5 microseconds at up to 100 Hz generate an extremely high energy density at the target, ablating the material and forming a plasma. The plasma expands outward from the target as a plume of ions towards the substrate where it deposits into thin films as can be seen in figure 4.3.

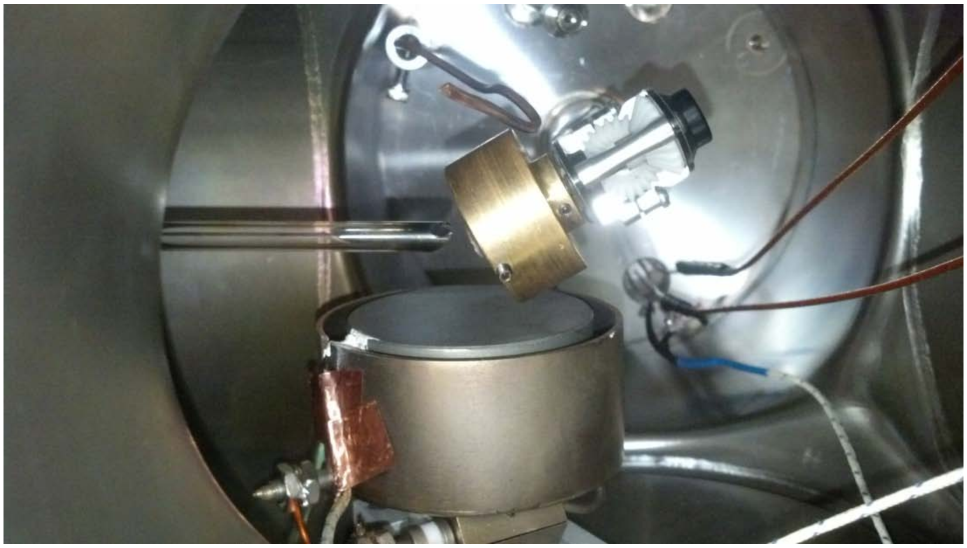

Figure 4.2 Image of the PPD chamber showing the rotating target holder, quartz nozzle, and substrate heater.

Figure 4.3 PPD system in operation with visible plume of ablated material.

Running the PPD source requires an operating gas, in our case argon, that flows through the electron gun and into the vacuum chamber. The powerful electric field generated during a pulse ionizes the gas which provides the high-energy electrons and plasma that bombards the target. This gas flow is highly adjustable, leading to a wide range of deposition chamber pressures from 5 x 10^{-5} to 1 x 10^{-2} mbar. Since the optimum pressure for deposition varies between materials, this allows for increased tuning to find the best conditions for a specific thin film. In addition, the chamber pressure influences the type of electrons generated. Low pressures encourage the generation of high-energy electrons but limits the maximum current, increasing the duration of the pulses. High pressures function in reverse, lowering electron energies but increasing current amplitudes for a shorter pulse. Chamber pressure, distance between gun and target, operational voltage, and substrate temperature are all variable parameters to adjust when finding the optimal regime for target deposition.

Since the PPD does not rely on laser absorption to create the plasma, target materials that would otherwise be difficult to deposit through PLD are made usable by this method. The pulse of energetic electrons can ablate all kinds of target materials, regardless if it is an insulator, semiconductor, metal, or even optically transparent. The pulsed nature of the plasma and the resulting ablation of the target allows for deposition on substrates at room temperature even though the temperature of the plume is much greater.

Preliminary depositions were carried out with a target of FeSe0.5Te0.5 on unheated substrates of glass, SrTiO3, and carbon nanotube sheets. Transport measurements of the resulting thin films confirmed that they were continuous but not superconducting.

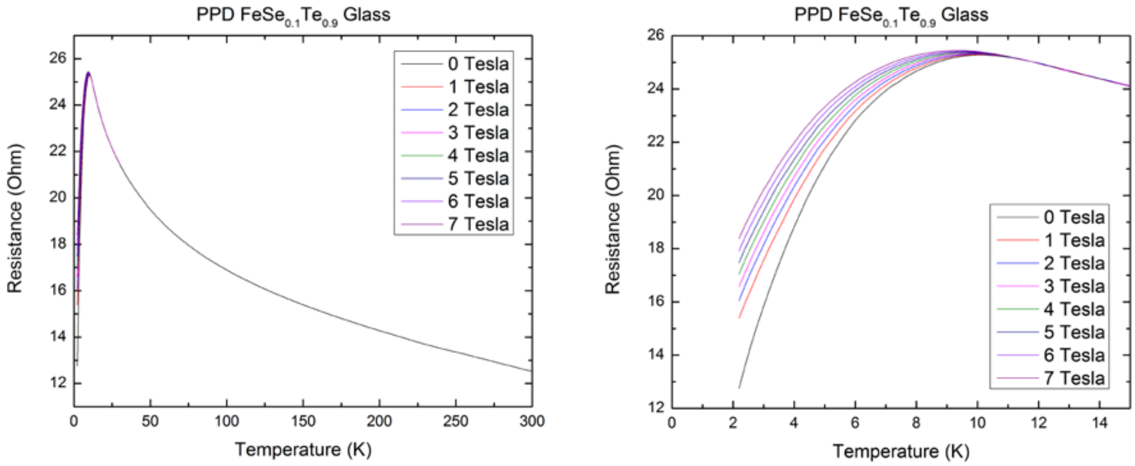

Figure 4.4 Resistance vs temperature measurements of FeSe0.1Te0.9 on plain glass substrate.

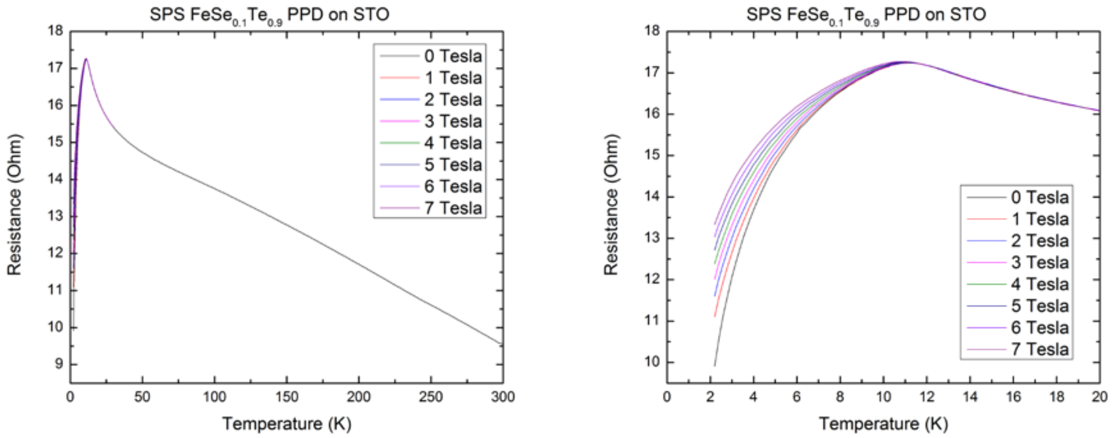

Figure 4.5 Resistance vs temperature measurements of $FeSe_{0.1}Te_{0.9}$ on $SrTiO_3$.

Installation of a new substrate heater allowed for deposition to be done at 400°C with a chamber pressure of 1.2 x 10^{-4} mbar with the substrate at a distance of 3.4cm from the target and pulses up to 12kV. Samples were prepared and deposited on substrates of glass and $SrTiO_3$ with a thickness of ~100nm. Figure 2.4 shows FeSe0.1Te0.9 deposited on glass with a T_c^{onset} of around ~10 K, and figure 4.5 shows the same chalcogenide deposited on the single crystal $SrTiO_3$ with a T_c^{onset} of ~11 K. Because of the extremely broad transition, the superconducting volume fraction must be considerably low, likely the result of non-optimized deposition conditions.

4.5. Increased H_{c2} in $FeSe_{0.1}Te_{0.9}$ close to as compared to $FeSe_{0.5}Te_{0.5}$

Ever since the discovery of the iron-based superconductors [1], they have aroused a great deal of research interest. Among them, the ‘11’ type iron based superconductor iron chalcogenide has the simplest structure with only a binary composition. The iron chalcogenide $FeSe_{1-x}Te_x$ demonstrates the interplay of structure, magnetism and superconductivity; the end-members FeSe and FeTe have quite different physical properties although they have similar crystal structure at room temperature. FeSe exhibits metallic behavior in the normal state and has a T onset c of 13 K [2]. FeSe and the composition close to the FeSe end will experience a transition from tetragonal to orthorhombic structure at low temperature described as distortion, indicated by the peak split in the XRD plot reported by Wang et al [3]. It was argued that the structural distortion is highly related to the superconducting transition temperature. The transition may also be suppressed by substrate confinement, for example, epitaxial thin film on MgO, $SrTiO_3$ and $LaAlO_3$ substrates with square pattern growth templates ($a = b$), which is not in favor of transition to the orthorhombic structure with $a \neq b$.

FeTe was predicted to have the highest transition temperature among the iron chalcogenide family [4]. However, FeTe exhibits antiferromagnetic (AFM) ordering at around 70 K along with a transition from tetragonal to monoclinic structure, which also corresponds to an anomaly in the temperature dependence of the resistivity plot, and it does not show superconductivity in bulk form [5]. Se or S can be covalently doped into FeTe to suppress the antiferromagnetic order from long range to short range to induce the superconducting transition [6]. The bulk materials have already been studied for the tellurium substitution effect on the superconductivity [2,5,7].

High quality epitaxial thin film is an ideal template to conduct a comparison study of the superconducting properties in correspondence with theoretical calculations. Differently from their bulk material forms, epitaxial superconducting FeTe thin films have been obtained through the strain effect [8] and oxygen incorporation [9,10]. a super high upper critical field close to 200 T has been achieved in FeTe thin films, which demonstrates the potential of this iron chalcogenide superconductor in high field applications [11,12].

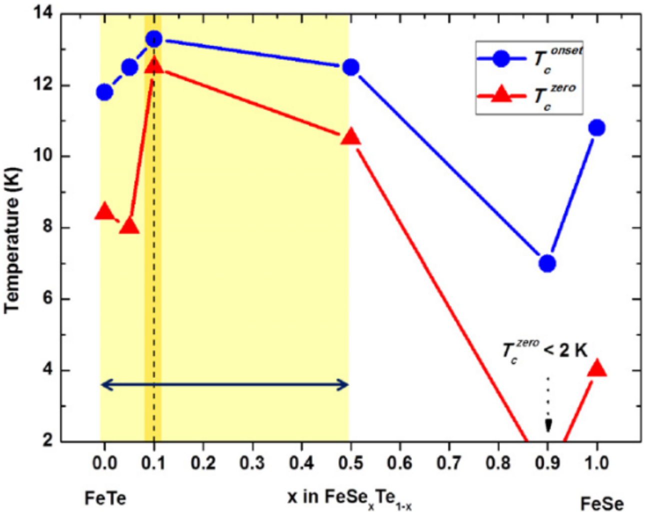

Figure 4.7. The dependence of the transition temperatures (T_c^{onset} and T_c^{zero} from transport measurements) on x in $FeSe_{1-x}Te_x$. The highlighted area marks the region for the compositions in this work and $FeSe_{0.1}Te_{0.9}$ presents the highest Tc, ranging from ~13.3 K (T_c^{onset}) to ~12.5 K (T_c^{zero}).

Towards practical applications, the drawback of FeTe films is their low critical current density, which is not measurable even at 2K by a vibrating sample magnetometer (VSM) in a physical property measurement system (PPMS). The low critical current density is possibly due to the low superconducting volume fraction in FeTe thin films and only the portion effectively doped with oxygen interstitial or substitution causing distortion to the parent non-superconducting phase demonstrates superconductivity. This explanation was also supported by the coexistence of superconducting and antiferromagnetic properties in iron chalcogenide superconductors such as FeTe thin films [8,9] and $KyFe_{2-x}Se_2$ [13–15]. It is also possible that the high upper critical field results from the parent antiferromagnetic phase.

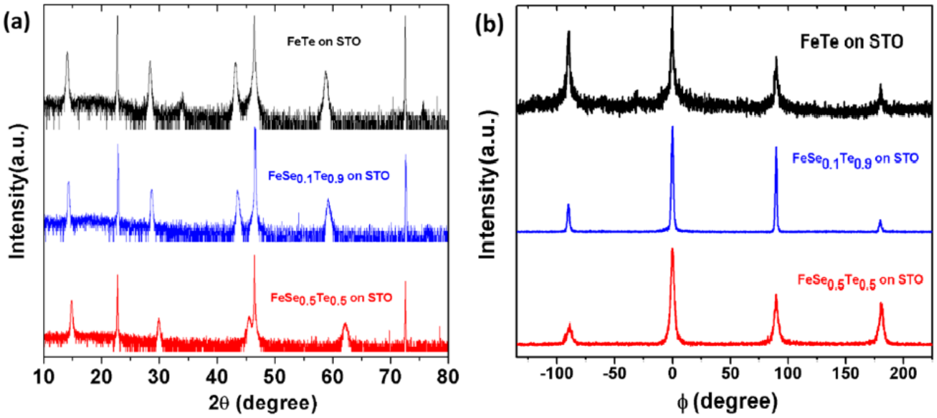

Figure 4.8. XRD plots of the single layer $FeSe_{0.5}Te_{0.5}$, $FeSe_{0.1}Te_{0.9}$, and FeTe thin films on STO substrates. (a) $\theta - 2\theta$ scan, (b) Φ scan of the $FeSe_{1-x}Te_x$ peaks.

To resolve this dilemma and to achieve both high upper critical field and high critical current density for practical applications, we propose to explore $FeSe_{1-x}Te_x$ epitaxial thin films with compositions close to the FeTe end, the end with antiferromagnetic order. The Te rich compositions are far away from the FeSe side without the orthorhombic transition at low temperature and close to the FeTe end without the monoclinic transition at low temperature. The idea lies in introducing chemical pressure into the parent FeTe phase to suppress the structural change at low temperature as well as the long range magnetic order to induce superconductivity. Se was selected to dope into the FeTe thin film to achieve homogeneous and stable incorporation because of the small ionic size difference between Te and Se. Microstructural and superconducting property characterizations were conducted to explore the optimum compositions for structural stability and superconducting properties.

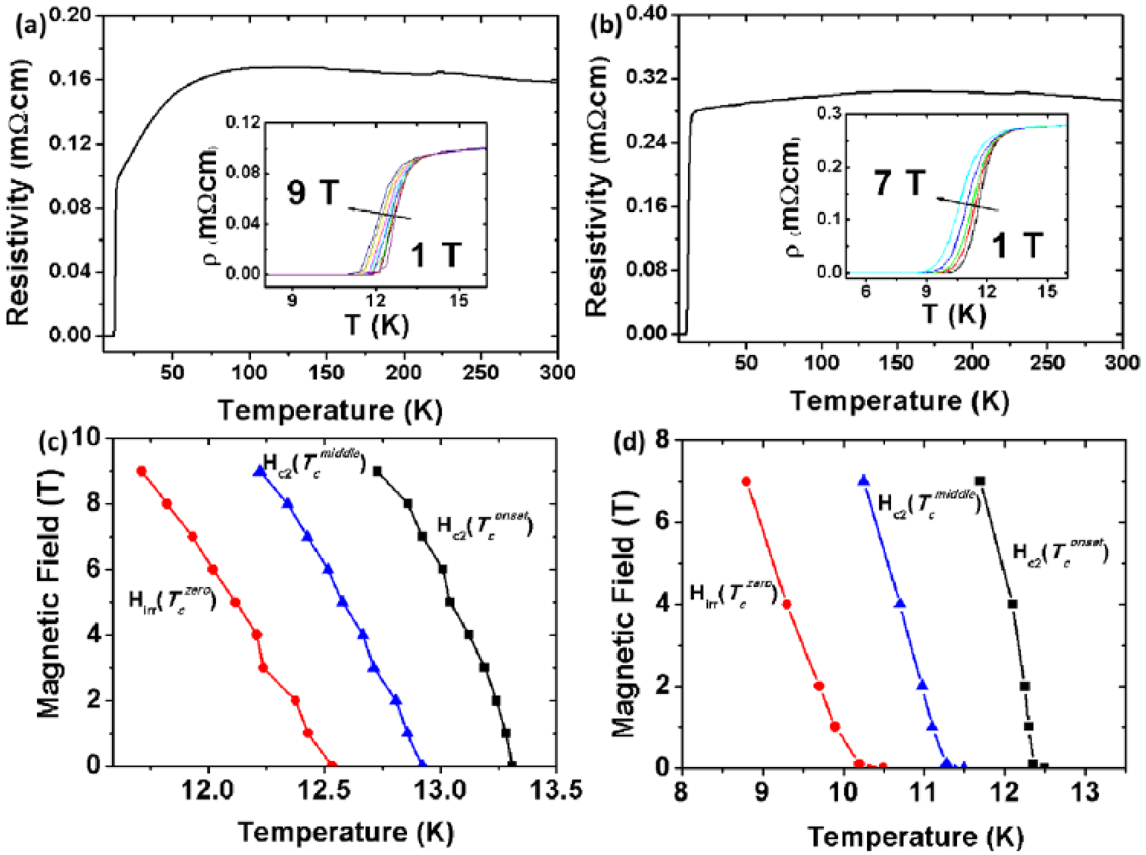

Figure 4.9. Parts (a) and (b) show the R(T) plots of the $FeSe_{0.1}Te_{0.9}$ and $FeSe_{0.5}Te_{0.5}$ thin films on STO from 2 to 300 K. The insets in (a) and (b) show the detailed superconducting transition regime from 2 to 20 K under magnetic field. The estimations for H_{irr} and H_{c2} are shown in (c) and (d) for $FeSe_{0.1}Te_{0.9}$ and $FeSe_{0.5}Te_{0.5}$ respectively.

FeSe, $FeSe_{0.9}Te_{0.1}$, $FeSe_{0.5}Te_{0.5}$, $FeSe_{0.1}Te_{0.9}$, $FeSe_{0.05}Te_{0.95}$, and FeTe targets were prepared by a standard solid-state reaction method with the appropriate stoichiometric mixture of Fe, Se and Te powders. The pure $FeSe_{1-x}Te_x$ (x = 0.5, 0.9, and 1) thin films were deposited at 400°C on single crystal STO (001) substrates in a pulsed laser deposition (PLD) system with a KrF excimer laser (Lambda Physik Compex Pro 205, $\lambda = 248$ nm, 5 Hz). During deposition, the target–substrate distance was kept at 4.5 cm. The growth rate of the $FeSe_{1-x}Te_x$ was around 0.5 Å/pulse. The laser power density was 3 J cm^{-2}. The base pressure for all the depositions was less than 1 x 10^{-6} Torr in vacuum. The total thickness of the $FeSe_{0.5}Te_{0.5}$ thin films was kept at around 100 nm.

The microstructure of the films was characterized by x-ray diffraction (XRD) (Panalytical X'Pert x-ray diffractometer), transmission electron microscopy (TEM) (FEI Tecnai G2 F20) and aberration-corrected scanning transmission electron microscopy (STEM) (TEAM 0.5, a modified FEI Titan microscope). The superconducting properties were characterized using resistivity–temperature (R(T)) measurement from 2 to 300 K with a four point probe method in a PPMS (Quantum Design). Both the self-field and the in-field critical current density (J_c^{sf} and $J_c^{in\text{-}field}$ (H∥C)) were measured under an applied magnetic field of 0-9 T at various temperatures with a VSM in the PPMS.

After all the different composition films have been deposited, the superconducting properties of the films are first screened by temperature dependence of resistivity (R(T), 2–300 K) measurements to screen the compositions. The T_c plots for T_c^{onset} and T_c^{zero} are shown in figure 2.7. It is clear that $FeSe_{0.1}Te_{0.9}$ presents the highest Tc at 13.3 K while $FeSe_{0.9}Te_{0.1}$ and $FeSe_{0.05}Te_{0.95}$ either did not show obvious T_c^{zero} or showed lower T_c results than $FeSe_{0.1}Te_{0.9}$. Therefore, this study focuses on the composition $FeSe_{0.1}Te_{0.9}$ and its comparison to $FeSe_{0.5}Te_{0.5}$ and FeTe. Figure 2.8(a) shows the standard $\theta - 2\theta$ XRD scans for the $FeSe_{0.5}Te_{0.5}$, $FeSe_{0.1}Te_{0.9}$, and FeTe films deposited on STO substrates. All three films are determined to be in the tetragonal phase without impurity phases and highly textured along FeSexTe1-x(00l) on STO (001). With increasing Te concentration the c axis parameters become larger for the $FeSe_{0.5}Te_{0.5}$, $FeSe_{0.1}Te_{0.9}$, and FeTe films and are calculated to be 5.9615 Å, 6.1851 Å, and 6.2585 Å, respectively. Figure 2.8(b) shows the Φ scans of the FeSe1-xTex(112) peaks for $FeSe_{0.5}Te_{0.5}$, $FeSe_{0.1}Te_{0.9}$, and FeTe. The four sharp peaks indicate the in plane texture for the thin films. The full width at half maximum (FWHM) values for the $FeSe_{0.5}Te_{0.5}$, $FeSe_{0.1}Te_{0.9}$, and FeTe(112) peaks are 3.7°, 1.9°, and 5.3°, respectively. Apparently, the in plane alignment for the FeTe film is not as good as that of the doped one with the FeSe framework. It is noted that the $FeSe_{0.1}Te_{0.9}$ has an even better in plane texture than the $FeSe_{0.5}Te_{0.5}$ thin film.

R(T) results (2-300 K) for $FeSe_{0.1}Te_{0.9}$ and $FeSe_{0.5}Te_{0.5}$ films on STO are plotted in figures 2.9(a) and (b), respectively. The details from 2 to 20 K are shown in the insets of (a) and (b). The $FeSe_{0.5}Te_{0.5}$ film shows a transition temperature Tc ranging from ~12.5 K (T_c^{onset}) to 10.5 K (T_c^{zero}). In comparison, the $FeSe_{0.1}Te_{0.9}$ has a higher transition temperature Tc ranging from ~13.3 K (T_c^{onset}) to ~12.5 K (T_c^{zero}), which is also higher than that of its bulk counterpart [5, 7]. The R(T) measurements under magnetic field parallel to the c-axis up to 9 T was carried out to estimate the upper critical field. The irreversibility line $H_{irr}(T)$ extrapolated with the T_c^{zero} and upper critical field $H_{c2}(T)$ extrapolated with the middle point of $T_c(T_c^{mid})$ and T_c^{onset} [16,17] are both plotted. The upper critical field is estimated by the WHH model,

$$-H_{c2}(0) = \frac{0.7\, T_c\, dH_{c2}}{dT\, |_{T_c}}$$

Based on the T_c^{mid}, the upper critical field H_{c2} is estimated to be 49 T and 114 T for the $FeSe_{0.5}Te_{0.5}$ and $FeSe_{0.1}Te_{0.9}$ films, respectively from the T_c^{mid}. The H_{c2} is much higher in the $FeSe_{0.1}Te_{0.9}$ thin film and the value is comparable to those of pure superconducting FeTe thin films deposited on STO substrate [8] and in controlled oxygen atmosphere [9]. Compared to the pure FeTe, it is much easier to get reproducible results in terms of homogeneity as well as deposition condition control in the vacuum deposited $FeSe_{0.1}Te_{0.9}$. It is apparent that the $FeSe_{0.1}Te_{0.9}$ shows smaller normal state resistivity compared to the $FeSe_{0.5}Te_{0.5}$, which is consistent with the finding of better epitaxial quality based on the Φ scan. Another feature of $FeSe_{0.1}Te_{0.9}$ is the anomaly corresponding to the structure and magnetic transition in the R(T) plot usually reported at around 70 K for FeTe bulk and thin film [18], which indicates that the antiferromagnetic transition becomes a broad hump starting at a temperature higher than 100 K.

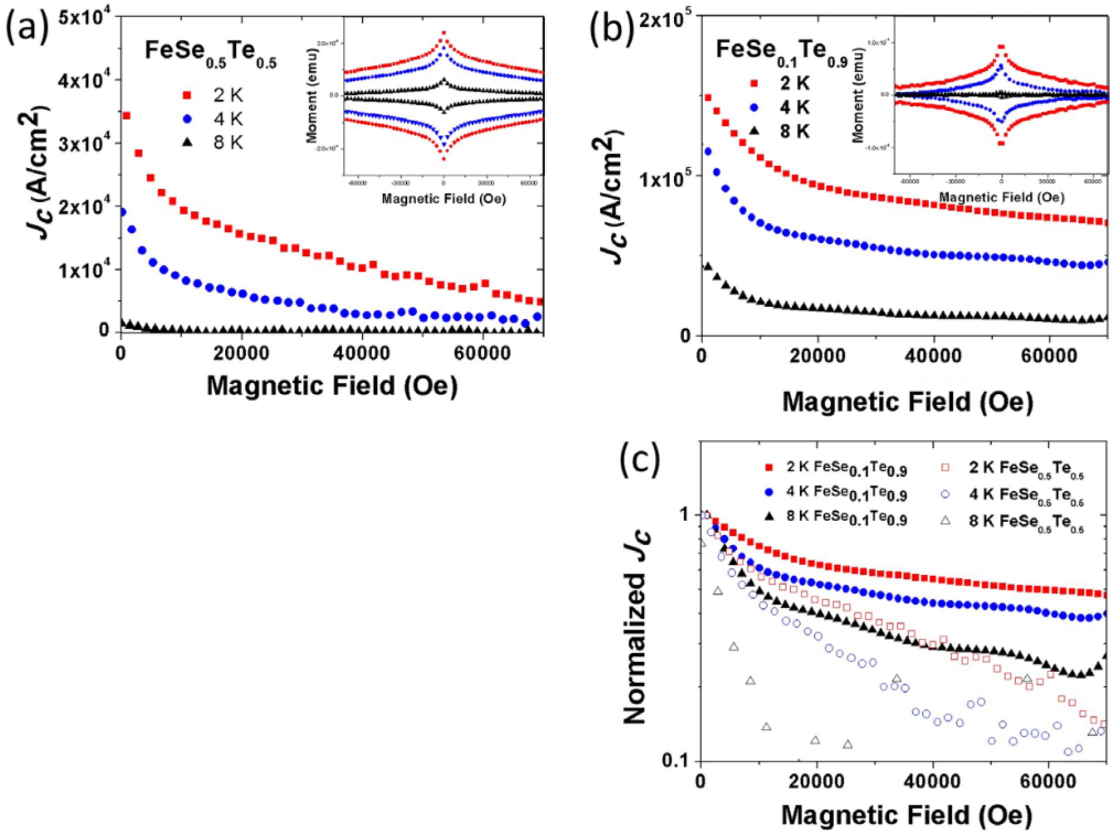

Figure 4.10. The field dependence of the critical current density for (a) $FeSe_{0.5}Te_{0.5}$ and (b) $FeSe_{0.1}Te_{0.9}$ thin films. The inset shows the magnetic hysteresis loops of the $FeSe_{0.5}Te_{0.5}$ and $FeSe_{0.1}Te_{0.9}$ thin films at 2, 4 and 8 K. (c) Normalized field dependence of the critical current density for the $FeSe_{0.5}Te_{0.5}$ and $FeSe_{0.1}Te_{0.9}$ thin films.

The magnetic hysteresis loops measured with the magnetic field parallel to the c-axis of the thin films are compared in figure 4.10 for the $FeSe_{0.5}Te_{0.5}$ and $FeSe_{0.1}Te_{0.9}$ thin films. There is no obvious fishtail shape in the hysteresis loops for any of the samples, indicating that our films are free from the weak or non-superconducting phases reported in bulk $FeSe_{0.5}Te_{0.5}$ [19,20]. The critical current densities were derived by the Bean model, which gives a reasonable estimation of the actual J_c value for moderate magnetization change in the testing range [19–21]. The calculated J_c values are plotted in figure 2.10 for 2, 4 and 8 K. Self-field J_c is as high as 1.8×10^5 A cm^{-2} at 2K, 1.3×10^5 A cm^{-2} at 4 K, and 0.5×10^5 A cm^{-2} at 8 K for the $FeSe_{0.1}Te_{0.9}$ thin film, compared to 3.4×10^4 A cm^{-2} at 2 K, 2.0×10^4 A cm^{-2} at 4 K, and 0.14×10^4 A cm^{-2} at 8 K for the $FeSe_{0.5}Te_{0.5}$ thin film. In addition, the J_c degradation of the $FeSe_{0.1}Te_{0.9}$ thin film is much slower under applied magnetic field, as indicated by the normalized J_c dependence on the magnetic field in figure 2.10(c). It should be noted that the J_c values of FeTe films were also measured by magnetization measurements. However, there is no obvious opening even at 2 K, which possibly indicates that the superconducting volume of the sample is relatively low. Therefore, it is difficult to give a definite value of the J_c for FeTe films at this stage. Further work is ongoing in the laboratory to further improve the FeTe transport properties.

The cross-section TEM images of $FeSe_{0.1}Te_{0.9}$ thin film on STO substrate and the corresponding selected area electron diffraction (SAED) patterns in the insets in figures 2.11(a) and (b) both show that the c-planes are parallel to the substrate surface with excellent epitaxial quality. The high resolution image along the film–substrate interface shows obvious film lattices and the clean film–substrate interface. The film thickness is around 100 nm. The film quality is comparable to the $FeSe_{0.5}Te_{0.5}$ thin film on STO substrate reported previously [22]. The c-axis parameter and ab plane lattice parameter of the $FeSe_{0.1}Te_{0.9}$ thin film are calculated to be 6.1721 Å and 3.8519 Å, respectively, according to the diffraction pattern. The c-axis parameter is consistent with the XRD result. Compared to the previous bulk $FeSe_{0.1}Te_{0.9}$ with c ~ 6.2136 Å and a ~ 3.8175 Å [7], the unit cell volume remains almost the same and the film lattice has ~0.67% compression in c and ~0.9% tensile strain in a. It is similar to the FeTe thin film on STO substrate which easily adapts to accomodate the mismatch with the substrate [8].

Figure 4.8(c) is a representative cross-section STEM micrograph. In STEM with the high-angle annular dark-field (HAADF) configuration, the image contrast is proportional to ~Z2. The contrast variation clearly demonstrates dark contrast nanoclusters which indicate the non-uniform distribution of the film composition. There are also nanoclusters with an average diameter of ~2 nm uniformly distributed in the thin film. This is, in a way, similar to our previous findings on the non-uniform composition distribution in $FeSe_{0.5}Te_{0.5}$ films, with dark contrast clusters as Te deficient or Se rich areas [22]. We further studied the details of the compositional variation with the intensity line profile based on the STEM images. It should be noted that the image contrast is an average through the sample TEM thickness.

The intensity line profile across one such nanocluster, as marked by the arrow, is inserted in figure 2.8(d). It is obvious that the intensity difference is much lower than the value of $Z_{Te}^2 = Z_{Se}^2$ and therefore suggests that the entire film region contains both Te and Se with minor variation in the composition between the matrix and the nanoclusters, i.e., slightly Se rich and Te deficient in nanoclusters. The volume fraction of the clusters is calculated to be ~6.28%. The average distance between clusters is ~5 nm, which is of the order of the coherence length of the iron chalcogenide [1,23]. The intrinsic chemical inhomogeneity was reported in an $Fe_{1+y}Se_{1-x}Te_x$ thin film study with STEM [24], and this nanoscale phase separation of the Te rich or Te deficient clusters with different superconducting transition temperatures compared to the ‘parent’ phase acts as possible flux pinning centers to enhance the in-field J_c and the pinning force [22]. In the case of $FeSe_{0.1}Te_{0.9}$, it is highly possible that point defects of composition variation can work as the flux pinning centers which yield high upper critical field. It was reported that better pinning properties are expected upon further optimization of the composition to get more self-assembled pinning centers [11].

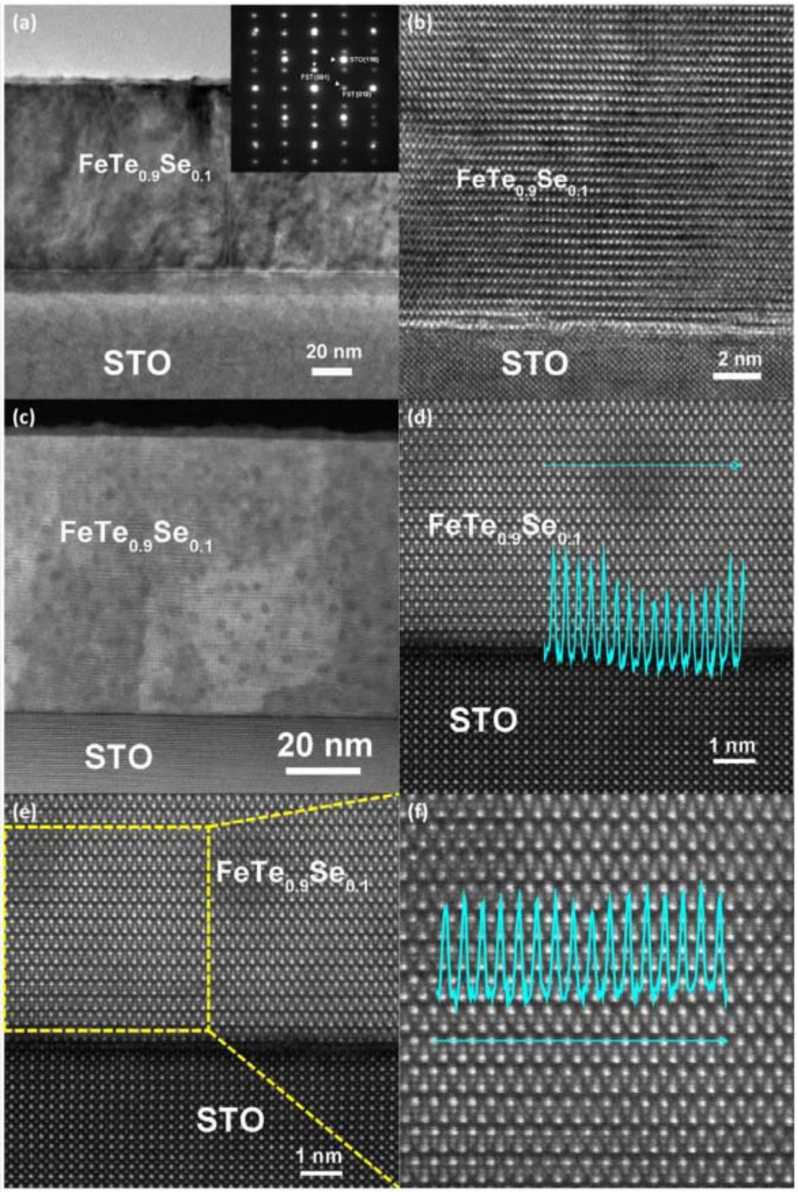

Figure 4.11. TEM results: (a) low magnification cross-section overview with the inset showing the SAED for the film with the substrate, (b) high resolution cross-section view for the $FeSe_{0.1}Te_{0.9}$ thin film on STO substrate, (c) STEM image of the low magnification cross-section overview for the $FeSe_{0.1}Te_{0.9}$ film on $SrTiO_3$ (100) substrate, (d) high resolution STEM with intensity line profile along the marked chalcogen plane in a typical dark cluster, (e) high resolution Cs-corrected STEM image for the $FeSe_{0.1}Te_{0.9}$ film on the $SrTiO_3$ (100)substrate, (f) enlarged view of the atomic lattice of the $FeSe_{0.1}Te_{0.9}$ thin film; the intensity line profile along the marked chalcogen plane is inserted.

To explore the Se and Te composition distribution in the film, an intensity line profile across the chalcogen planes was applied in the enlarged high resolution Cs-corrected STEM image in figure 2.8(e) to study the Se and Te distribution in the 'parent' phase. There is no obvious intensity variation in the peaks, as illustrated in the line profile inserted in figure 2.8(f), which indicates the homogeneous distribution of the Se and Te elements in the 'parent' phase, and also there is no obvious structural variation. The intensity profile in the STEM micrograph identified a nearly random distribution of the Te and Se, which is very similar to our previous STEM study on $FeSe_{0.5}Te_{0.5}$[24] and single crystal $FeSe_xTe_{1-x}$ (0<x<0.5) by Ekino et al [25].

Based on the above observation, a random distribution of the Te and Se throughout the 'parent' phase in the $FeSe_{0.1}Te_{0.9}$ thin film seems more reasonable and more likely to achieve better superconducting properties. Compared to the ineffective and unstable doping of oxygen into the FeTe indicated by the reversible oxygen incorporation during the thermal cycle under different atmospheres [10], uniform Se doping could be more ideal. The approach of doping the parent FeTe with a small amount of Se has been demonstrated to be effective to achieve homogeneous superconducting properties at the small price of a minor decrease of the upper critical field compared to $FeTe:O_x$ thin film. In addition, a much higher critical current density was achieved in this $FeSe_{0.1}Te_{0.9}$ thin film compared to the $FeSe_{0.5}Te_{0.5}$ thin film. It is interesting that, even with minor Se doping in FeTe films, the $FeSe_{0.1}Te_{0.9}$ thin film still maintains the main characteristics of $FeSe_{0.5}Te_{0.5}$ films, such as tetragonal crystal structure, high critical transition temperature, high critical current, reproducible film growth, long term phase stability and good epitaxial quality. Now, combined with a high H_{c2} value as large as 114 T, superconducting $FeSe_{0.1}Te_{0.9}$ thin films hold great promise for future high field applications.

In this research we have successfully grown epitaxial superconducting $FeSe_{0.1}Te_{0.9}$ and compared it with $FeSe_{0.5}Te_{0.5}$ and FeTe thin films on STO substrates. The $FeSe_{0.1}Te_{0.9}$ on STO has a transition temperature Tc ranging from ~13.3 K (T_c^{onset}) to ~12.5 K (T_c^{zero}). The H_{c2} of the film is ~ 114 T, which is comparable to that of the superconducting FeTe thin film but much higher than that of the $FeSe_{0.5}Te_{0.5}$ thin film on STO. At the same time, a higher critical current density compared to the $FeSe_{0.5}Te_{0.5}$ thin film, which is promising for practical applications, was achieved in the $FeSe_{0.1}Te_{0.9}$ film. These results show that iron chalcogenide superconducting thin film with composition close to the magnetic order (FeTe side) presents great potential for high field applications.

5.SUPERCONDUCTING WIRES BASED ON MgB2 COATED CNT.

5.1. Introduction: Magnesium Diboride MgB2 as High Hc and Jc Classical Superconductors

Superconducting properties of pure and C-nano doped magnesium diboride

MgB_2 is a promising superconductor for large scale industrial applications due to its high critical temperature (about 40 K), exceptional critical current densities, relatively low anisotropy, and low cost of starting materials. The significant advantage of MgB_2 based superconductors is that MgB_2 has "weak link" free grain boundaries and the supercurrent density is controlled by flux pinning rather than by grain boundary connectivity. But critical fields and critical current of a pure MgB_2 are lower than in conventional superconductors NbTi and $NbSn_3$. Significant improvements of superconducting properties of MgB_2 can be achieved by doping with carbon-based materials.

5.1.1. Origin of superconductivity in MgB$_2$

MgB$_2$ is a metal with layered structure, where Mg atoms are located between the centers of hexagons of honeycombed boron planes (Figure 5.2a). The electronic states at the Fermi level are either σ- or π-bonding boron orbitals (Figure 5.2b-d) [62]. Two σ-states are confined in the boron planes, and couple very strongly to the in-plane vibration of boron atoms. This results in a strong electron-pair formation of the σ-bonding states with an average energy gap of 6.8 meV. Two π-states are formed between boron planes which also couple with phonons, and contribute to Cooper pair formation with smaller band gap of 1.8 meV (Table 2). Due to charge transfer from σ- to π-band, localized holes of σ-band are formed within the boron layer and have high anisotropy, while electrons at π-band are delocalized over the whole crystal.

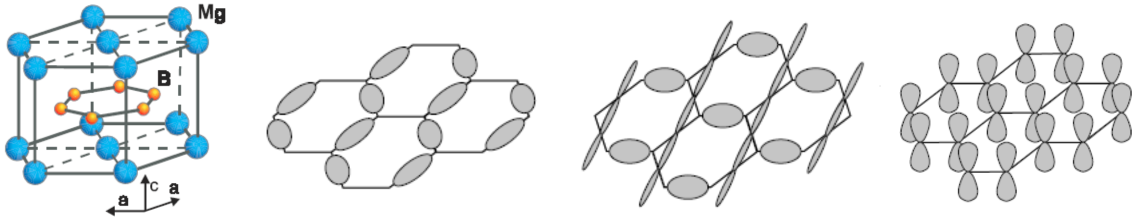

a b c d

Figure 5. 8: a) crystalline structure of MgB$_2$ [63]; b-c) σ-bonding states at Fermi level, derived from $p_{x,y}$ orbitals; d) π-bonding states, derived from p_z orbitals [62].

	Δ(0), meV	**λ(0), nm**	**ξ(0), nm**	**κ=λ/ξ**
σ	7.1	47.8	13	3.68
π	2.2	33.6	51	0.66

Table 5. 2: Characteristic properties of the σ and π bands. Δ(0)– zero temperature band gap, λ(0) zero temperature penetration depth, ξ(0) – zero temperature coherence length, κ=λ/ξ – Ginsburg-Landau parameter.[64]

The single-band Ginzburg-Landau (GL) model is not valid for MgB$_2$, and the theory has to be extended to the two-band case. The most straightforward approach is to express the free energy of the superconductor as a sum of two single-band GL functionals plus a Josephson type coupling term [65]. The interband coupling causes superconductivity always to appear in both bands at the same temperature [66], although superconductivity in the π-band has much less contribution and the band gap is small (Table 2). At small magnetic field (below 1 Tesla) and close to the transition temperature, Cooper pairs of the π-band have a noticeable contribution to the superconductivity, and that results in a positive curvature of upper critical field (B_{c2}) near the critical temperature (T_c) [67].

Characteristic properties of the σ and π bandsΔ(0) – zero temperature band gap, λ(0) zero temperature penetration depth, ξ(0) – zero temperature coherence length, κ=λ/ξ – Ginsburg-Landau parameter.[64]

5.1.2. Superconducting properties of pristine undoped MgB_2

The critical temperature of pure MgB_2 is considered to be 39.4K [68], and depends on the quality of the superconductor and impurities [69]. The only mechanism observed at the moment that can increase T_c – is softening of the E_{2g} phonon mode, which is strongly coupled to the σ-band. It is observed in high quality thin films of MgB_2, where the lattice mismatch puts a tension on the MgB_2 boron plane and increases the lattice parameter [70, 71]. Considering this, theoretical calculations suggest unique superconducting properties with high T_c in MgB_2-graphene bilayered structures [72].

The main four mechanisms that reduce the critical temperature are the reduction of density of states, the reduction of σ-band anisotropy, the hardening of the E_{2g} phonon mode and intraband scattering. All the experiments on pressure as well as doping with various compounds showed the reduction of T_c [73].

Studies of MgB_2 single crystals showed anisotropy of superconducting properties, and first of all – magnetic properties [74]. The anisotropy coefficient $\gamma = H_{c2}^{ab}/H_{c2}^{c} = \xi^{ab}/\xi^{c}$ ranges from 1.5 to 4.5 depending on measurement techniques (Figure 3a), and increases for higher critical fields, since the contribution from σ-band become dominant. Even if the in-plane upper critical field exceeds 20 T with approaching 0 K, the out-of-plane critical field hardly reaches 5 T. Similar behavior is observed for textured thin films of MgB_2 of a very high quality, although the film is polycrystalline [75]. So the grain boundaries can be considered transparent for supercurrent, which is confirmed by many other experiments and makes MgB_2 attractive for practical applications

In polycrystalline samples, upper critical fields reach about 15 T at 0 K (Figure 4b) which is lower than the maximum critical field reached in a single crystal, and show almost linear behavior with a pronounced positive curvature near T_c. With approaching nanocrystalline grain size of 40-100 nm, the slope of critical field dependence is higher with the lower T_c (Figure 4b) [76]. Preparation conditions play a major role in superconducting properties of polycrystalline samples; the main improvement can be attributed to a low relative purity of samples (96 %).

From the phenomenological Ginzburg-Landau theory the upper critical field B_{c2} is related to the coherence length ξ in the following way:

$$B_{c2} = \frac{\Phi_0}{2\pi\xi^2} \tag{1.3}$$

Here $\Phi_0 = \frac{h}{2e} = 2.07 \cdot 10^{-15}$ Wb is the magnetic flux quantum. This relationship holds for high quality superconductors where the mean free path of electrons is much higher than coherence length ($l \gg \xi$). If this condition is not valid, then the coherence length has to be modified $\frac{1}{\xi} = \frac{1}{\xi_0} + \frac{1}{l}$, where ξ_0 is the intrinsic coherence length of the superconductor, ξ, the effective coherence length and l, the mean free path. Even without deep analysis, it can be clearly seen that as mean free path decreases, it starts dominating the effective coherence length and, as a result, upper critical field increases. The essence of decreasing mean free path is introduction of so called scattering centers

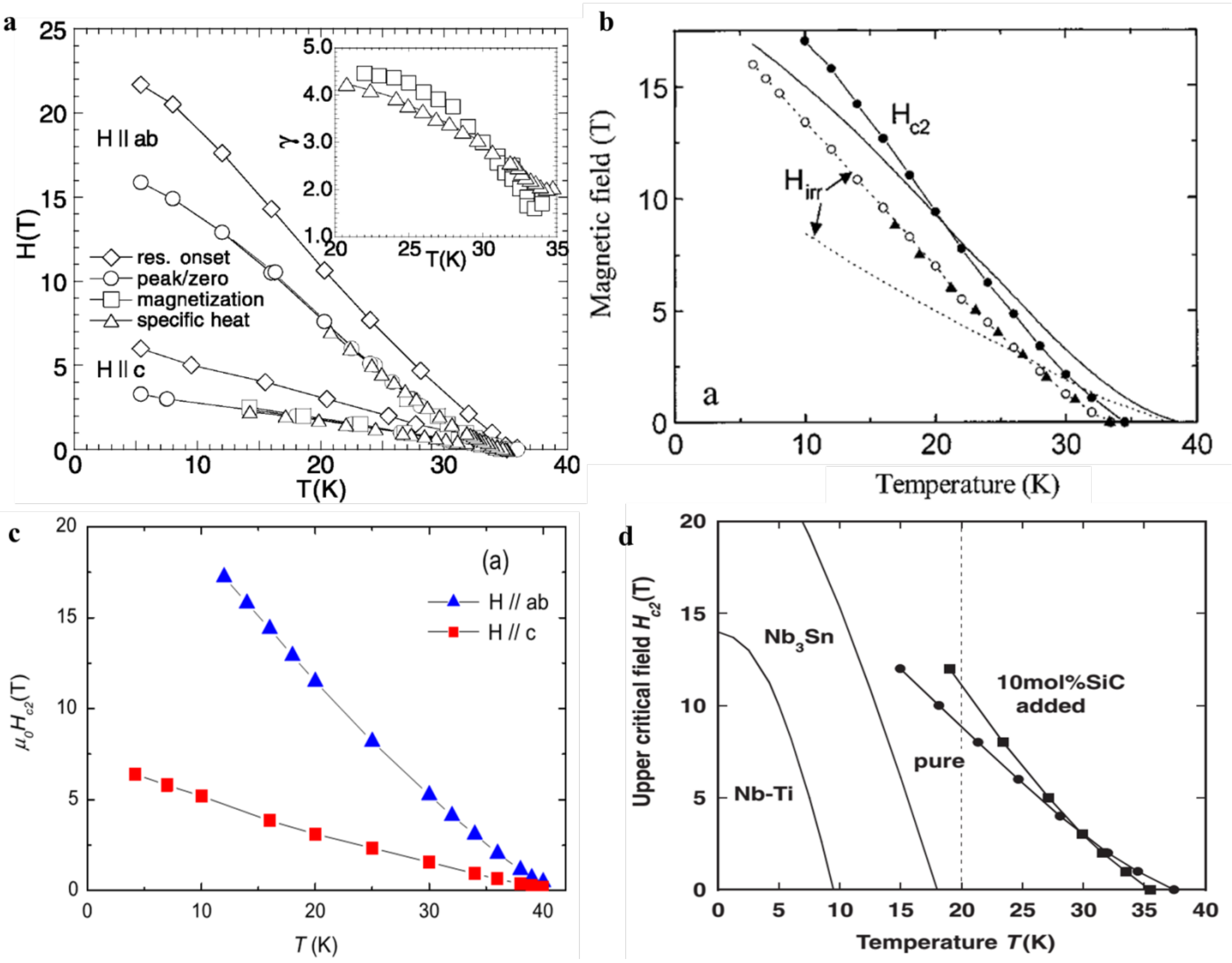

Figure 5.9: a) MgB_2 single crystals, measured by various techniques for magnetic field applied along the c- and ab-axes. Inset shows the temperature dependence for the anisotropy coefficient γ [74]; b) critical field of poly (lines) and nano-crystalline (lines with symbols) MgB_2 [76]; c) upper critical field of high quality textured MgB_2 thin film, where c-asix is perpendicular to film surface [75]; d) upper critical field of MgB2 tapes, developed for commercial applications [77].

In MgB_2 scattering centers can have various natures, usually of atomic size, such as vacancies, local disorder, grain boundaries, impurity-substitution atoms and nanocrystalline inclusions. So that even in comparison between polycrystalline and nanocrystalline samples the significant increase of upper critical fields can be explained by more defective structure in the latter (Figure 5.3b).

The common limit for achievable critical current density in superconductor is a depairing current J_d, that can be estimated with equation:

$$J_d = \frac{\Phi_0}{3\sqrt{3}\pi\lambda^2\xi\mu_0}. \tag{1.4}$$

Here λ is the penetration depth and $\mu_0 = 4\pi \cdot 10^{-7}$ $V{\cdot}s{\cdot}A^{-1}{\cdot}m^{-1}$, the permeability of free space. The depairing current can be achieved only partially in superconductors (up to 10-15%) and mostly with optimized pinning, which prevents vortex flow. At 0K and without a magnetic field the main contribution to the superconducting current comes from σ-band, and if we use parameters from Table 2, the depairing current density is $J_d \approx 3.4 \cdot 10^{12}$ A·m^{-1}. If the magnetic field above 1 Tesla is applied, the depairing current decreases [67].

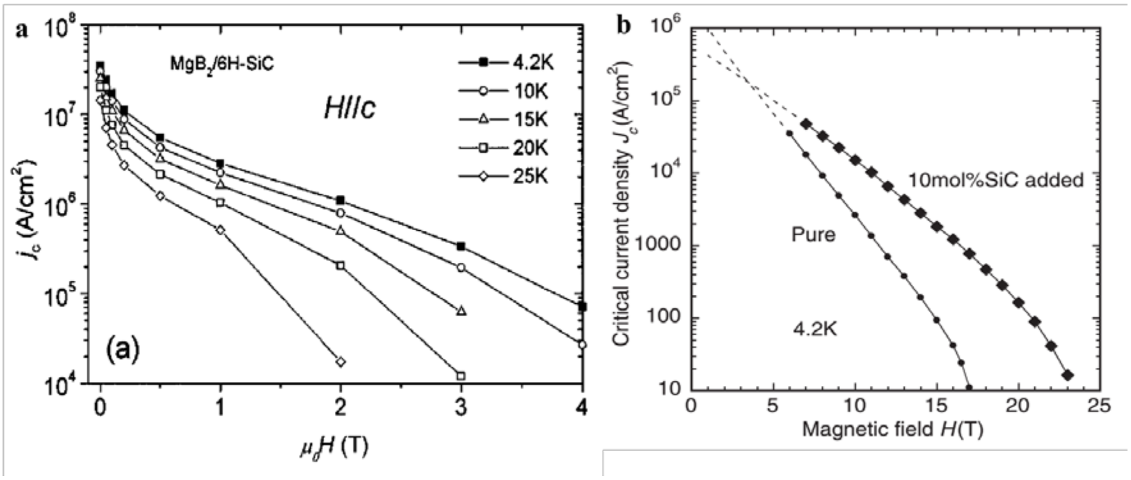

Figure 5. 10: a) Critical current density for thin film at various temperatures [78]; b) critical current density of polycrystalline superconducting tapes [77].

The highest critical current density reported for thin films is around $3 \cdot 10^{11}$ A·m^{-1} from transport measurements (Figure 4) [78], although other reports have similar values [79, 80]. It has been shown that with decreasing grain size, the critical current increases, and this effect is attributed to improved flux pinning. Thus, grain boundaries can provide strong pinning. Improvement of J_c by pinning is also confirmed in bulk samples, doped with nanocrystalline SiC (Figure 4).

5.1.2.1. Improvement of superconducting properties of magnesium diboride by inclusion of carbon nanoparticles and by carbon doping

The main important goal of doping is the enhancement of critical current and critical fields. There are two main mechanisms for such enhancement (as discussed above): boron substitution creates electron scattering centers, and incorporation of defects and impurity particles increases flux pinning strength [81].
The best results on enhancing $J_c - H_{c2}$ performance are obtained by adding carbon in elemental form (fullerenes, nanotubes, nanodiamond, graphene) or by C-containing compounds such as SiC, TiC, B_4C, and organic compounds. Improvement of the $J_c(H)$ dependence on different types of doping of MgB_2 wires and tapes is shown in Figure 5. The in-field critical current for nano-SiC doped samples increased by more than one order of magnitude compared with the un-doped samples. Fresh reactive carbon is released from the SiC at low temperature (600 °C), when SiC reacts with Mg to form Mg_2Si. This reactive carbon can effectively substitute boron, and highly dispersed particles of Mg_2Si and nanosized C act as flux pinning centers.

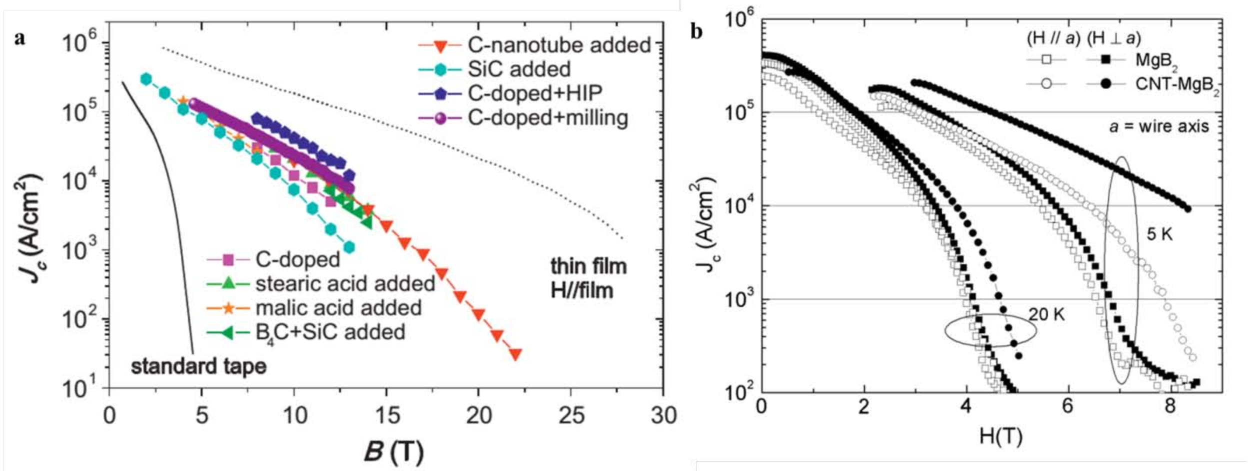

Figure 5.11: a) $\boldsymbol{J_c - H_{c2}}$ for MgB2 doped with various carbon containing compounds [82]; b) $\boldsymbol{J_c - H_{c2}}$ – MgB2 wire doped with carbon nanotubes [83].

The organic materials can decompose at relatively low temperatures, and generate the reactive carbon for MgB_2 doping. But the high amount of oxygen that comes with the organic doping can negatively affect superconducting properties.

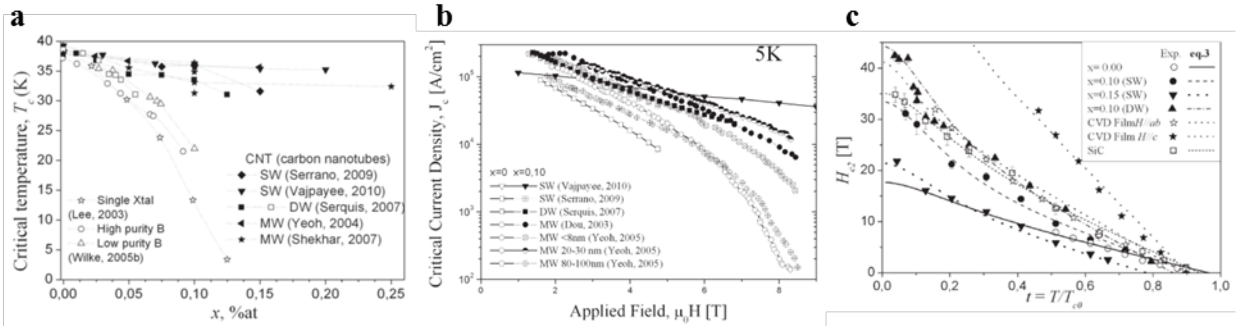

Figure 5. 12: Superconducting properties of CNT doped MgB_2 [84]: a) critical temperature as a function of the nominal carbon content using different carbon sources; b) Critical current density – field dependence from magnetization measurements with the same nominal composition x=10%, but different CNT types; c) upper critical field derived from transport measurements.

Doping of MgB_2 with carbon nanotubes showed significant improvements of superconducting properties, and also can be used to reinforce, improve heat transfer, and dissipation [85]. The optimum CNT nominal content is about 10% for highest $J_c - H_{c2}$ performance. Comparing different types of nanotubes, one finds the highest effect on critical current from double-walled [86] and multi-walled CNT (20-30 nm diameter) [87] (Figure 6). That can be attributed to a more homogeneous C-incorporation by avoiding nanotube agglomeration.

As a summary, even though critical temperature of MgB_2 is only 39K, which is low for using cheap liquid cryogenic technologies based on liquid nitrogen, MgB_2 is a promising superconductor for large scale industrial applications due to its exceptional critical current densities, relatively low anisotropy, and low cost of starting materials. It is a real competitor with commercial superconductors: NbTi and Nb_3Sn. The significant advantage of MgB_2 based superconductors over BSCCO (T_c~ 108K) and YBCO (T_c~92K) is that MgB_2 has "weak link" free grain boundaries, so the supercurrent density is controlled by flux pinning and by grain boundary connectivity [88].

Chemical doping is one of the most effective and relatively simple ways to improve superconducting properties of MgB_2 and includes element substitution and/or inclusion of impurity particles. Even though no dopants were found to increase the transition temperature, substitutional and inclusion doping improved flux pinning, infield critical current densities, upper critical and irreversibility field. The most significant effect was observed for carbon and carbon-based compound doping [81]. Carbon nanotubes have several advantages as a component of superconducting composite: they can carry relatively high currents comparing to copper, can provide mechanical strength and have high thermal conductivity, which can improve thermal stability and enhance heat dissipation of MgB_2 wire. Being one-dimensional nanostructures, they can act as highly effective pinning sites.

As clear from the above Introduction both CNT and MgB2 are representing two classes of novel electronic materials, created in last decade and holding great potential for applications.

The motivation for the present work was to combine this two unique materials and create a composite MgB2/CNT nanostructures which will have superior properties to all existing superconducting wire systems beating them either in electrical or mechanical or thermal performance at same or less cost.

Particularly the objectives are to create MgB2/CNT yarns, that can be combined into superconducting wires, that will be flexible, lightweight and will beat existing PIT (powder in the tube) type MgB2 wires in flexibility and nish applications.

For this several tasks has been solved:

The novel method was developed to synthesize MgB_2 on the surface of carbon nanotubes, which included two steps: laser assisted chemical vapor deposition of boron on CNT sheets and annealing in Mg vapors to convert it into MgB_2. The important question addressed in this process was optimization of synthetic conditions and the analysis of the thickness, morphology and crystalline structure of MgB_2/CNT nanowires.

5.1.3. Studying of superconducting properties of MgB_2/CNT sheets yarns.

Superconducting properties will be characterized with transport measurements and magnetization measurements. Critical temperature, critical field and critical current density of various MgB_2/CNT yarns will be found and correlated with correlated with morphological and structural characteristics. Since our superconducting matrix is extremely porous (>90% porosity), we will pay special attention to the calculations of a critical current density, which is usually normalized by cross-section area. Several techniques will be used to improve the estimation and to compare with reported values for MgB_2 superconductors. The anisotropy of superconducting propertis will help to understand the role of carbon nanotubes in such composites.

5.1.4. Superconducting wires based on MgB_2/CNT hybrid sheets and yarns

Soon after its discovery, MgB_2 was already considered a promising candidate superconductor for various applications [1]. Besides having superconducting properties that are comparable to or even better than commercially used superconductors, MgB_2 also has a simple crystalline structure, low density and can be synthesized from cheap raw materials. MgB_2 can be prepared in the form of nanoparticles [2], nanofibers [3] and thin films [4], that have similar, or even improved, superconducting performance relative to its bulk form.

The standard approach to make strong superconducting wires of brittle materials, such as MgB_2 is a powder-in-tube technique. The main disadvantages of this method are poor connectivity between MgB_2 grains, usually covered with oxides, and low filling factor of the powder in cladding [5]. Also, these MgB_2 wires are not very flexible: its bending strain before failure, defined as a ratio of wire diameter to the yarn diameter, is below 0.005 [6]. Doping with carbon compounds (organic compounds, nano-carbon, fullerenes, CNTs, graphene, and nanosized carbides) improves superconducting properties in high magnetic fields for drawn wires and tapes [7]. The final performance of doped MgB_2 samples also improves due to increased filling factor, introduction of defects into crystalline structure and decrease of MgB_2 grain size [7,8,9].

Carbon atom inclusions in the MgB_2 crystalline structure serve as electron scattering centers, that increases the upper critical field (H_{c2}) and consequently critical current density (J_c), since the sample can sustain higher fields generated by current flow [10]. On another hand, embedded nanosize particles serve as pinning centers that hinder vortex movement, which requires energy and give rise to resistance. Carbon nanotubes, aside from doping effects, also provide mechanical reinforcement, improve heat transfer, and supply current dissipation in MgB_2 superconducting wires [8]. The optimum CNT content seems to be about 5 wt% for highest J_c and H_{c2} (which corresponds to the composition $MgB_{1.8}C_{0.2}$) [11].

Another synthetic approach to superconducting wires has been reported for MgB_2 in which 160 µm wires are produced by diffusion of Mg into the boron layer deposited around tungsten wires [12]. However, this method produces samples with multiple defects and cracks, which significantly reduces the mechanical strength of the wire.

As a novel approach to create superconducting wires, we developed MgB_2/CNT hybrid yarns using CNT sheets as a mechanically robust template for the synthesis of magnesium diboride nanowires, as well as an effective dopant that can improve superconducting performance (Figure 5.12). Produced MgB_2-CNT composite has the form of an aligned nanowire network, which can be spun into yarns of unlimited length.

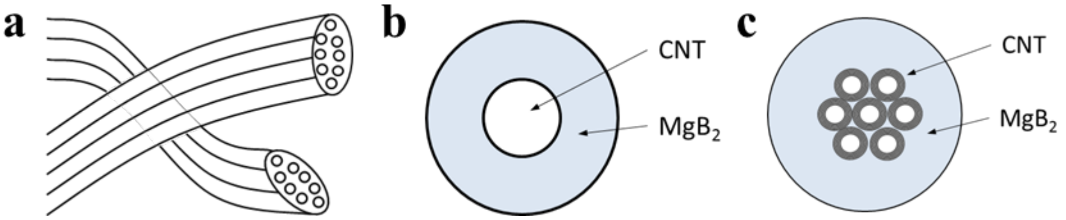

Figure 5. 13: a), c) Bundles of CNT coated with superconductor. b) CNT (12-15 nm diameter) coated with superconductor.

The first step is the production of boron nanowires using aligned carbon nanotube sheets as a template and BBr_3 as the precursor for boron deposition. For this purpose, a forest of spinnable nanotubes was placed inside a photo-thermal chemical vapor deposition (CVD) reactor filled with BBr_3 vapor (Figure 13). During the deposition process, a 50-100 nm thick sheet of carbon nanotubes is drawn from the CNT forest and wrapped around a mandrel while a stationary laser beam heats the CNTs, thereby causing the gas phase decomposition of BBr_3 to produce boron coated CNTs. After the deposition, the mat of B-coated CNTs on the mandrel (comprising 20-50 sheet layers) can be liquid densified with acetone and cut from the mandrel. Depending on the laser exposure time, the thickness of the boron coating can be varied from 20 nm up to several hundred nanometers (Figure 14). This birolling process and subsequent biscrolling process provides much higher current densities than the boron-particle-based biscrolling method that we have previously used to fabricate superconducting MgB_2 yarns [26].

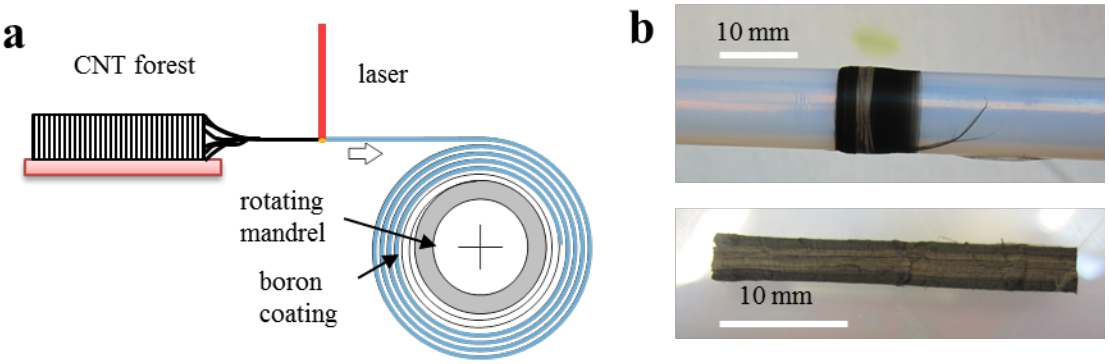

Figure 14: a) Setup for continuous laser assisted chemical vapor deposition; b) B-CNT stack on mandrel and free standing

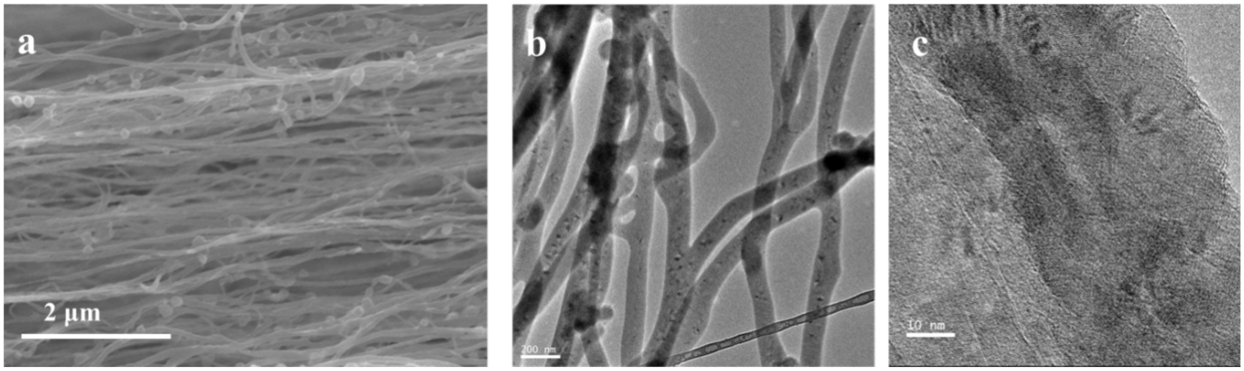

Figure 5.15: a) SEM image of boron/CNT network; b) TEM images of boron nanowires; c) TEM image of individual boron wire with CNT core.

Boron coated CNT sheets can be converted into MgB_2, either before or after biscrolling the sheets into yarns. This is accomplished by annealing in Mg vapor (which enables subsequent diffusion of Mg inside the boron nanowires and corresponding chemical transformation). The transformation of the B into MgB_2 was accomplished in a 1 atm tubular quartz furnace at a temperature of 900°C (for 10 minutes in Ar/5-10% H_2 using a flow rate of 300 sccm). The nanowire thickness observed in SEM images almost doubled, which supports magnesium penetration into the boron lattice and MgB_2 formation (Figure 15).

There are two samples selected for comparative study. Morphological differences as well as various hydrogen content during annealing in Mg vapors (5% for Sample A, and 10% for Sample B) contribute to the differences in superconducting properties.

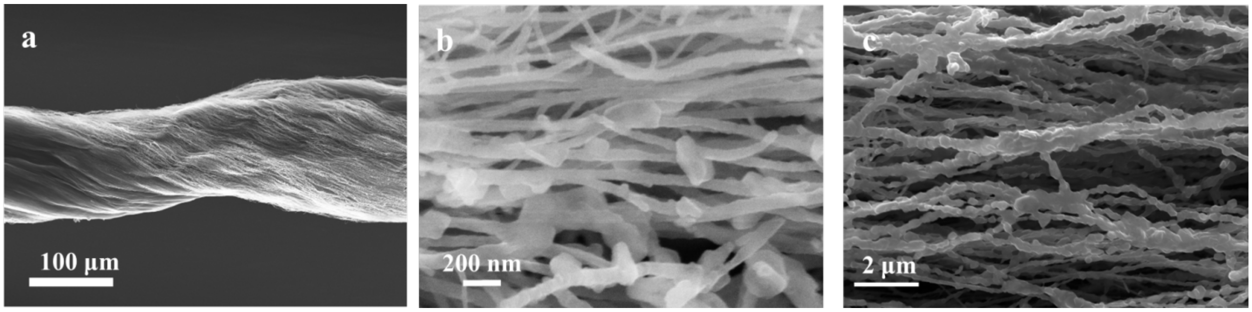

Figure 5. 16: a) MgB_2/CNT yarn; b) MgB_2/CNT nanowires of sample A; c) MgB_2/CNT nanowires of sample B.

Carbon nanotube networks have been previously used as a base layer to biscroll magnesium diboride particles into superconducting MgB_2 yarns, although superconducting properties of such composites have been poor due to limited connectivity between MgB_2 grains [13]. Another method to fabricate composite yarns is templating CNT sheets with inorganic materials through physical deposition methods and subsequent twist spinning into final shape [14].

We here present a new method for the synthesis of MgB_2-CNT composites, wherein carbon multi-walled nanotubes (MWNTs), assembled in a highly oriented carbon nanotube aerogel sheet, provide a template for the deposition of a boron layer with controlled thickness around individual CNTs and CNT bundles, which is later converted into MgB_2 to provide MgB_2-CNT shell-core nanofibers. Sheets of coated nanofibers are twist spun in the solid-state to produce a superconducting yarn.

Carbon nanotubes and their bundles are mechanically strong, have high thermal and electrical conductivity and therefore serve as suitable cores for MgB_2 nanofibers, providing mechanical strength and damping during a superconducting quench. Even though bulk MgB_2 is a very brittle material, MgB_2-CNT yarns can be easily bent to small radii without damage. Moreover the continuous coating of CNTs with boron by chemical vapor deposition (CVD), during the simultaneous drawing of a CNT sheet from a CNT forest and twist-based spinning of the sheet into yarn, enables continuously production of tens of meters of B-CNT yarns, which can yield similar lengths of MgB_2-CNT yarns.

MWNT forests were synthesized by CVD on iron-particle-catalyzed silicon substrates and then drawn in the solid state to provide nanometer-scale thickness, carbon nanotube sheets having nearly the same density as air [15]. The drawing direction defined the preferential alignment axis of CNTs in these sheets, which can be twist-spun into yarns [16]. The extremely low areal density of these thin sheets, between 1.8 and 5.0 $\mu g\ cm^{-2}$ in the present study (**Table S1**), combined with their low heat capacity [15], low thermal conductivity [17] and their high light absorption, allowed the localized heating of a carbon nanotube aerogel sheet to high temperatures (~2000 K in vacuum) [18] using similar power as obtained for an ordinary laser pointer (0.3 W). Local temperatures up to 1670 ºC were achieved for a 1.5 torr atmosphere of hydrogen gas pressure by using a focused laser beam having 250 $W\ cm^{-2}$ intensity (**Figure S1**).

Local laser heating by a scanned beam was used to promote chemical reaction between BBr_3 and hydrogen on the surface of CNTs and CNT bundles in sheets, which provided crystalline boron and hydrobromic acid vapor: $2BBr_3+3H_2=2B+6HBr$. In parallel, boron carbide can be formed during this process: $4BBr_3+6H_2+C_{CNT}=B_4C+12HBr$, although the rate of this reaction is limited by slow solid-state diffusion through the carbide layer. The thickness, crystallinity and morphology of the boron layer can be controlled over a very wide range by tuning the laser beam intensity, exposure time, and precursor vapor pressure. The typical microstructure of the initial and boron coated CNT sheets are shown in scanning electron microscope (SEM) images (**Figure 1a** and **Figure 1b** respectively).

Since MWNT forests can produce very long sheets (each centimeter of forest yields typically about 5-6 meters of sheet having the same width as the forest (Table S1)) we were able to develop semi-continuous production of boron-coated CNT sheet and yarn (**Figure 1c**). For this purpose, a spinnable MWNT forest was placed inside a photothermal CVD reactor and exposed to a low-pressure mixture of BBr_3 vapor and hydrogen gas. During the deposition process, a sheet of MWNTs was drawn from a forest while a scanned laser beam locally heated the sheet, thereby causing decomposition of BBr_3 to produce boron-coated CNTs. Scanning of the laser beam in the sheet width direction was used to cover a wider area of the MWNT sheet as it passes under the laser (**Figure 1d** and **Movie S1**). Along the drawing direction the coating was very uniform. Perpendicular to that direction, however, there was a variation in the boron thickness due to the variation in laser exposure time during laser scan. The resulting long, thin sheet of B-CNT nanofibers is flexible and can be wrapped around a mandrel to provide a layer stack. The boron coating is visible with the naked eye and usually changes the color of nanotube sheets to grey-brown. Alternatively to wrapping B-CNT layers and then twist spinning a segment from a layer stack, the B-CNT nanofiber yarns can be produced by using simultaneous sheet draw and twist-spinning during laser scan (**Figure S2**).

We produced B-CNT nanofibers having diameters between about 50 and 100 nm (Figure 1b), with an average boron layer thickness of 20-40 nm around CNT bundles (as well as segments of individual nanotubes that are not bundled, which less commonly exist). Transmission electron microscope (TEM) shows a polycrystalline morphology (**Figure 1e**), however it is difficult to recognize CNT walls inside the nanofibers due to the similar atomic number of boron and carbon. From selected area electron diffraction (SAED) patterns, the boron in the B-CNT shell-core composite (**Figure 1f**) is polycrystalline, containing possibly a mixture of boron allotropes that is dominated by the rhombohedral β-form.

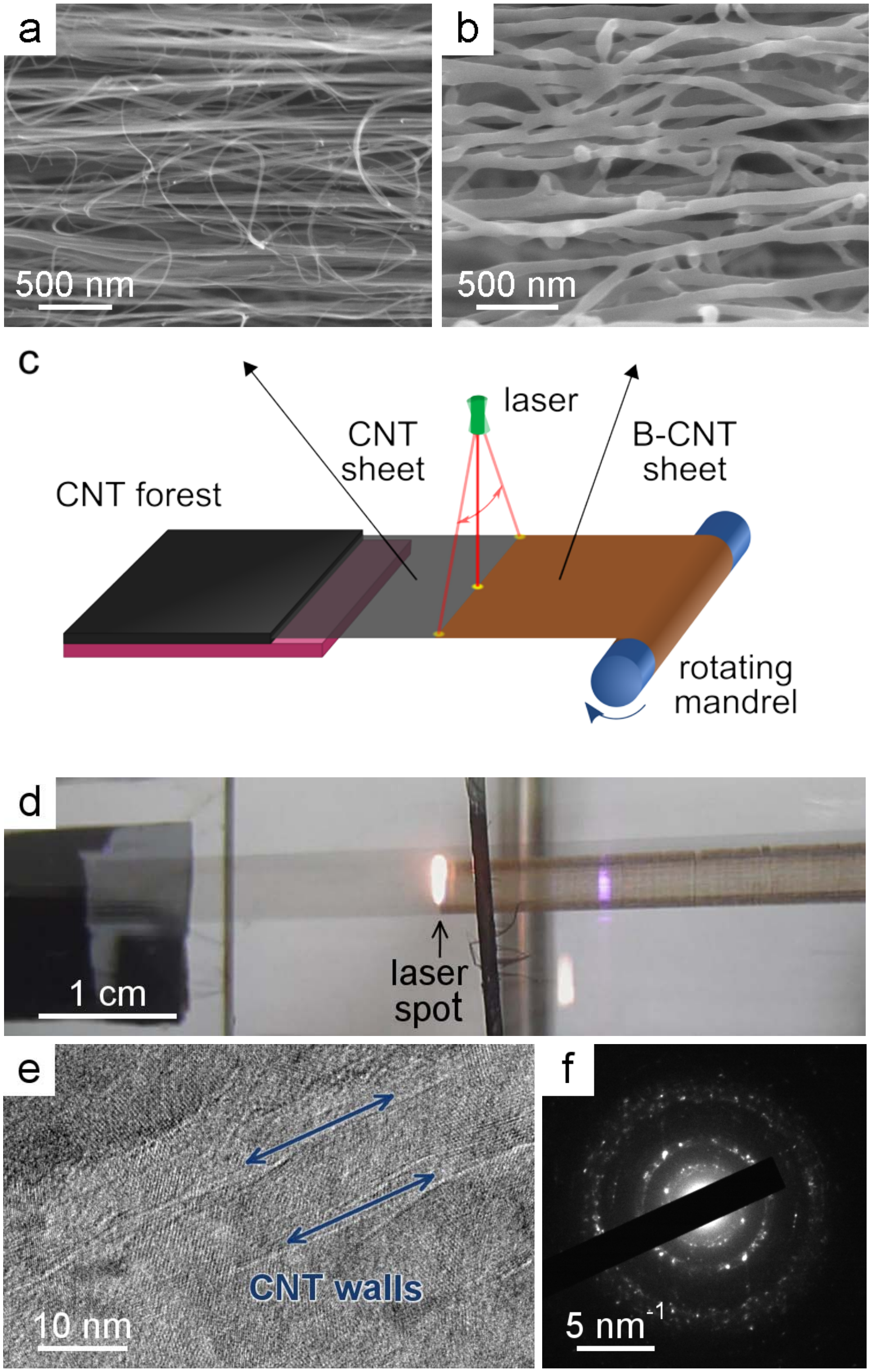

Figure 5.1.1. a) pristine CNT sheet (SEM); b) boron-coated CNT sheet (SEM); c,d) schematic illustration and photograph for photohermal CVD of boron on a forest-drawn CNT sheet; e) TEM image of CNT bundle embedded in boron sheath; f) SAED pattern of a boron-coated CNT nanofibers.

These B-CNT nanofibers were used as scaffolds for formation of MgB_2-CNT nanofibers by exposing them to magnesium vapor at 900 °C as described in the experimental section. The weight of the final MgB_2-CNT composite nanofibers increased by about 90% compared to the weight of the original B-CNT nanofibers, suggesting complete conversion of boron into MgB_2. The average CNT content in the final composite is about 4.8%wt. The MgB_2-CNT nanofibers consist of connected nanosize crystals that can be clearly seen in SEM and TEM images (**Figure 2a** and **Figure 2b**). The main crystalline phase by x-ray diffraction (XRD) analysis is $MgB_{2,}$ with 8 %at. of MgO and 5 %at. of metallic Mg (**Figure 2c**).
Investigation of the diameter distribution of nanofibers before and after reaction with magnesium (**Figure 2d**) shows an increase of the average diameter of the nanofibers from 50-100 nm for B-CNT to 70-200 nm for MgB_2-CNT. This is about the expected diameter change during the conversion from boron to magnesium diboride
For studying superconducting properties of the composites, we prepared 50 to 250 um yarns (**Figure 2e**). The yarns were cut using a focused ion beam (FIB) to analyze their internal structure. SEM images of the cross-section of yarns show approximately 92-95% empty space (**Figure 2f** and **Figure S3**). The density of the sample used in this study is 0.124 g cm^{-3}, which is an order of magnitude lower than for typical MgB_2 wires produced by powder-in-tube methods inside metallic sheath (1.3-1.4 g cm^{-3} [19]) and 20 times less dense than MgB_2 wire with tungsten core (2.4 g cm^{-3} [12]), which is close to theoretical density of MgB_2 2.55 g cm^{-3}. The density of MgB_2-CNT yarn in our study, corrected by porosity of the yarn measured from the SEM image analysis of its cross-section, approximates the density of the bulk MgB_2. Additionally, the specific surface area of such yarns is estimated from micrograph analysis along with gravimetric measurements and is about 160 m^2 g^{-1} (Supporting Information).

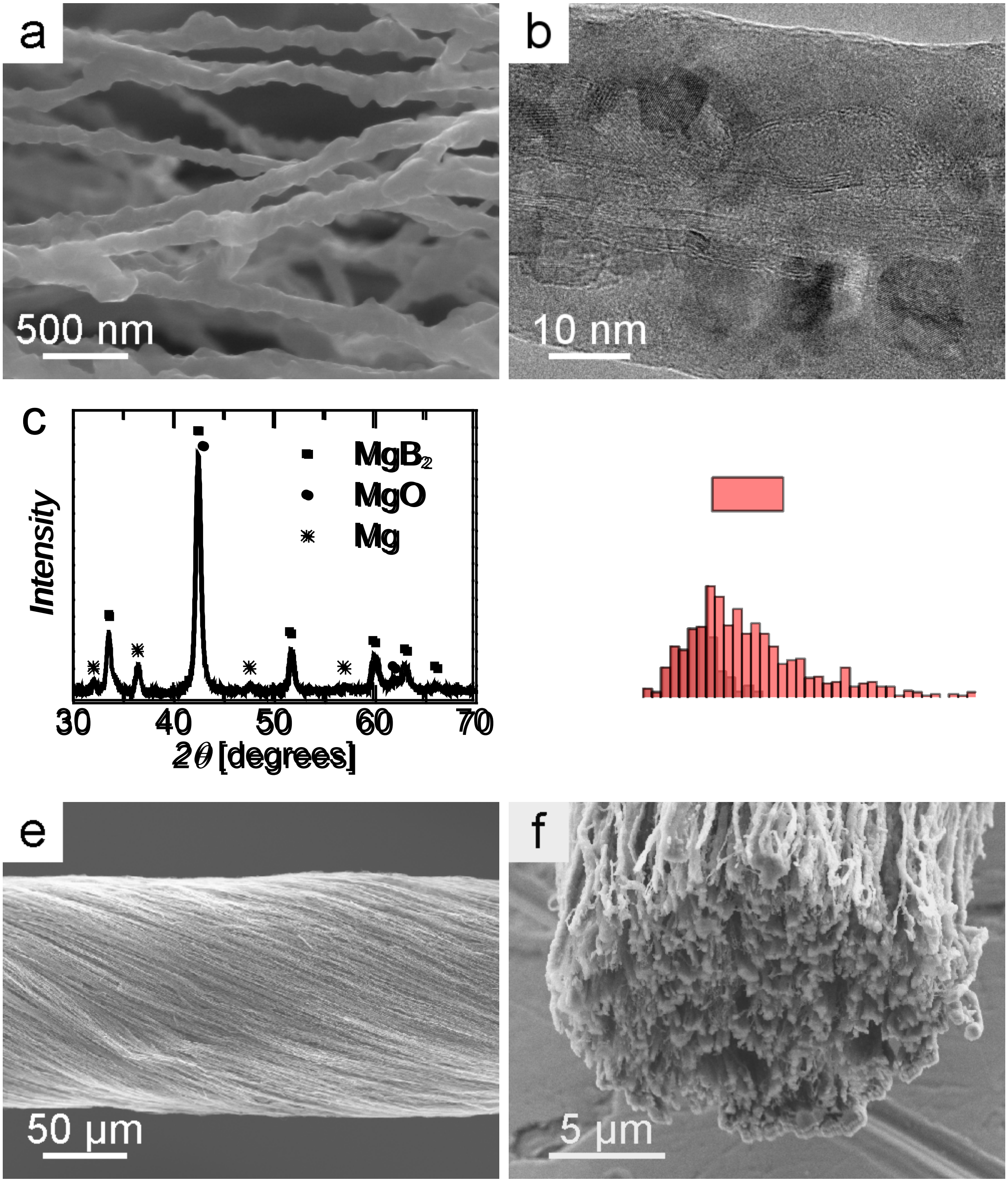

Figure 51.2. a) SEM image of a MgB_2-CNT nanofiber sheet, uneven morphology is due to large MgB_2 nanocrystals forming nanofibers; b) TEM image of a MgB_2-coated bundle of carbon nanotubes; c) XRD spectra of a MgB_2-CNT sheet stack; d) size distribution of B-CNT nanofibers and MgB_2-CNT nanofibers; e) lateral SEM image of a 250 µm diameter MgB_2-CNT twisted yarn; f) cross-sectional SEM image of a 50 µm diameter MgB_2-CNT yarn.

Electrical resistance versus temperature for applied magnetic fields up to 7 Tesla is shown in **Figure 3a**. In the absence of magnetic field, the onset temperature for superconductivity is 37.8 K and the resistance drops to zero at 34.3 K. The critical fields at which the resistance dropped to 90% and to 10% of normal state value (40 K) are plotted versus temperature in **Figure 3b**. The superconducting transition is broad and its width increases with increasing field. The T = 0 London penetration depth of clean, bulk MgB_2 is 35-50 nm [10] and increases at higher temperatures, so it becomes comparable to the diameter of MgB_2 nanofibers (about 70-200 nm). The reduced dimensionality of nanofibers interconnected into a network gives rise to percolation and fluctuation effects, which broadens the zero-field transition.

The high-field H_{c2} characteristics for our likely carbon-doped MgB_2-CNT nanofiber yarns are improved compared with those for bulk MgB_2 wire [12], which agrees with earlier findings for carbon-doped MgB_2 [11]. Carbon substitution at boron sites creates local scattering centers which, in the dirty limit, reduce the Ginzburg-Landau coherence length, thereby increasing the upper critical field at low temperatures toward the extreme dirty limit, $H_{c2}=\Phi_0/(2\pi l^2)$ (Φ_0 – flux quantum) [10]. Indeed, differing mean-free paths (l) along different MgB_2 pathways will result in a spread of upper critical field values, further broadening the transitions in applied magnetic fields.

The critical current was determined by I-V measurements at different fields at 4.2 K using a voltage criterion of 1 µV/cm (**Figure 3c**). Due to the large difference in density compared to samples prepared by conventional methods and in order to compare yarns of various thicknesses and sizes, the critical current I_c was normalized by the linear gravimetric density (expressed as g cm^{-1}), which is the same as critical current density J_c normalized by gravimetric density ρ (with units g cm^{-3}): J_c/ρ [A cm^{-2} g^{-1} cm^3 = A cm g^{-1}]. This way, instead of using the total cross-section, which is up to 95% empty, only the effective cross-section is taken into the account. For comparison, we show critical current data for dense MgB_2 wires obtained by transport measurements [12]. At higher fields MgB_2-CNT yarn has an order of magnitude higher gravimetric critical current density than dense MgB_2 wires (Figure 3c) at 5 K and at 20 K. While this result is surprising, considering the extremely high porosity of the MgB_2-CNT yarn, it likely demonstrates the positive effects of high crystallinity, inter-grain connectivity along the wires, and the effective doping effect provided by carbon nanotube network. This behavior is similar for carbon-doped MgB_2 wires [8,11] and is usually attributed to increased critical field. To the contrary, at low magnetic fields, doping does not much affect superconducting properties and the critical current in doped samples is similar and sometimes slightly lower than in non-doped samples [10].

The multifilament structure in MgB_2-CNT nanofiber sheet provides outstanding flexibility comparing to conventional MgB_2 wires: it can be easily bent without mechanical damage and applied to planar and highly curved surfaces. Moreover, these sheets can be twisted into yarns that maintain desired characteristics as a superconductor. As a prototype for a possibly practical superconductor, a B-CNT sheet was laminated with forest-drawn CNT sheet for reinforcement and twisted into yarn. After annealing in Mg vapor, this yarn was transformed into a MgB_2-CNT yarn having excellent mechanical properties, which could be bent and even tighten into a knot while maintaining superconductivity (**Figure 3d, Figure 3e** and **Figure S4**). Considering the yarn and knot diameters, the bending strains can be estimated to be 0.25 and 0.45 for the maximum and minimum diameter of the knot, which are at least 100 times larger than is possible without fracture for MgB_2 wires fabricated using conventional methods. The flexibility of these CNT laminated MgB_2-CNT yarns enables them to be weaven into textiles (**Figure 3f** and

Figure S5). The room temperature resistance of these MgB_2-CNT yarns have been stable for more than 60 cycles during the bending cycling test (**Figure S6**). The rupture tensile strength normalized by gravimetric density of MgB_2-CNT yarns reaches 161±47 MPa g^{-1} m^3 and exceeds the tensile strength of conventional metal-sheathed MgB_2 wires [20] (**Figure S7** and **Table S2**).

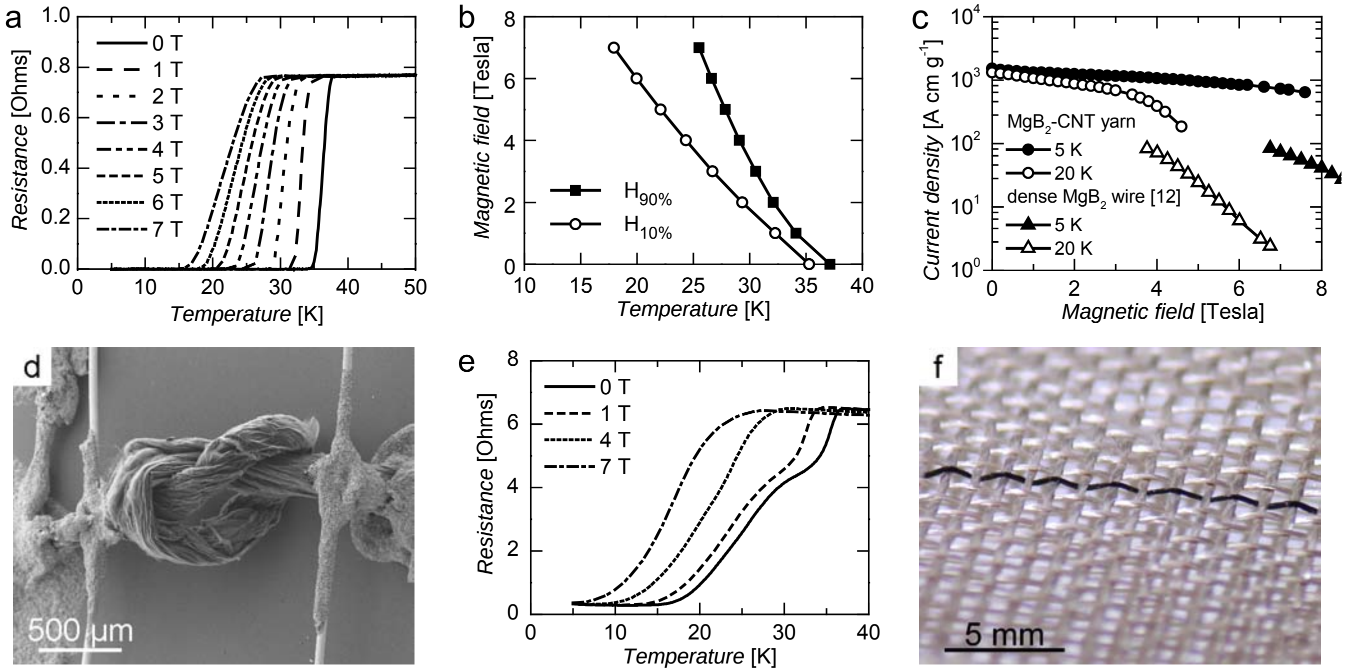

Figure 51.3. a) $R(T)$ for different applied magnetic fields, b) $H_c(T)$ for a MgB_2-CNT superconducting yarn, critical fields are defined as $R(H_{90\%},T)=0.9R_n$, R_n is resistance in the normal state at 40K and $R(H_{10\%},T)=0.1R_n$; c) $J_c/\rho(H)$ critical current density normalized by gravimetric density, (A cm^{-2}) / (g cm^{-3}) = A cm g^{-1}; d) SEM micrograph of a knotted MgB_2-CNT yarn with 4-probe connections to gold wires and e) $R(T)$ for different applied magnetic fields for the knotted yarn shown in d); f) textile containing MgB_2-CNT superconducting yarn.

In summary, a semi-continuous method for producing flexible MgB_2-CNT composite yarns having attractive superconducting properties has been demonstrated using forest-drawn MWNT sheets as a template. First, CNT sheets have been coated with boron by semi-continuous photothermal chemical vapor deposition, and then B-CNT networks have been converted into MgB_2-CNT composite networks by annealing in magnesium vapors.

The critical temperature reaches 37.8 K and gravimetric superconducting characteristics are significantly improved compared to those for bulk pure-MgB_2 superconducting wires. The low density, flexibility and porosity of the MgB_2-CNT yarns make them suitable for applications where these properties are required. For instance, superconducting yarns can be woven into textiles and braids and their porosity enables fast cooling using a penetrating cryogenic liquid or gas. Additionally, it is anticipated that the pores in the superconducting yarns can be filled with normal state conductors by infiltration or electrodeposition of metals. Finally, the existence of these porous superconducting yarns having giant internal surface area may provide a useful platform for investigating the effects on superconducting properties of (a) electronic coupling with materials infiltrated inside the pores and (b) chemical or electrochemical charge injection into the MgB_2 [21].

Experimental Section

Continuous photothermal boron deposition. For continuous boron deposition, a spinnable CNT forest was fixed on the holder inside the quartz tube reaction chamber (50 mm diameter), and the end of a drawn CNT sheet was attached to a 13.2 mm diameter teflon mandrel. The inlet of the reactor was connected through a flow controller to a hydrogen gas cylinder, as well as to a cylinder containing BBr_3 (Aldrich). The outlet of the reactor was connected to the vacuum pump through a liquid nitrogen trap. The BBr_3 cylinder was kept in the ice bath to control its vapor pressure. The reaction chamber was maintained at 8.6 torr of BBr_3 vapor and the hydrogen flow was 30 sccm. Local heating of the CNT sheets to deposite B from the BBr_3 vapor was accomplished using an external laser power (808 nm wavelength, 1.2 W, 0.72-0.85 mm beam diameter) whose beam position was controlled using galvano-mirror system. During deposition of the boron, the mandrel was rotating at 1.5 rpm, which corresponded to the sheet draw from the CNT forest at 6.2 cm/min, and the laser beam was oscillating in direction across the sheet width at 30 Hz to produce a 8-mm-wide boron line on the CNT sheet. About 20 layers of boron-coated CNT sheets were collected on a mandrel. Afterwards, the sheet stack was carefully cut along the axial direction of the mandrel, so that separate strands of B-CNT could be peeled from the mandrel, twisted into yarn, and used later for magnesium treatment to convert the B to MgB_2.

Treatment in magnesium vapor. Boron-coated CNT samples were attached to the lid of a graphite crucible filled with magnesium flakes and loaded in the quartz tube (diameter 50 mm) chamber of an electrical furnace. The furnace was heated to 900 ℃ during 45 minutes with then cooled down to ambient at 8°C/min. The gas flow was 250 sccm for Ar and 50 sccm for H_2. After this annealing in Mg vapor, the samples were used for transport measurements and other characterizations.

Characterization of superconducting sheets and yarns. Imaging was by scanning electron microscopy (JEOL 2100F at 11 kV) and transmission electron microscopy (JEOL 2100 at 200 kV). Yarn cross-sectional cutting for imaging utilized a focused ion beam (FEI Nova 200, Ga ions 30 kV, 1-7 nA). X-ray diffraction characterization utilized a Rigaku Ultima III XRD. Transport properties measurements in a 4-probe contact configuration were made using a Quantum Design PPMS-9 system and DC and AC options.

Electrical resistance versus temperature for applied magnetic fields up to 7 Tesla was measured in a PPMS (Physical Properties Measurement System) using a 4-probe electrode configuration. Yarns of aligned, interconnected MgB_2-CNT nanowires showed a critical temperature at zero field of 38 K (onset) and at 24 K the resistance dropped to 0 for sample B (Figure 16). Broad superconducting transition of sample A can be attributed to presence of weak links and Josephson junctions (JJ), with T_c much lower than that of MgB_2 grains. The transition of JJ is observed as a separate step on R(T) curves with T_c below 20 K. Sample B has a broad superconducting transition but not as broad as sample A. Grain boundaries and impurity inclusions (MgO, CNTs, possibly B_4C, Mg condensated) serve as an effective pinning centers, while intergrain scattering centers reduce the mean free path and as a result increase the critical field and critical current.

The critical temperature for the upper critical field H_{c2} was defined as the temperature at which ρ/ρ_n=90% (where ρ and ρ_n – are resistance at which the temperature is defined and resistance in normal state respectively). The irreversibility field H_{irr} (the field at which current vanishes) was defined as ρ/ρ_n=3%.

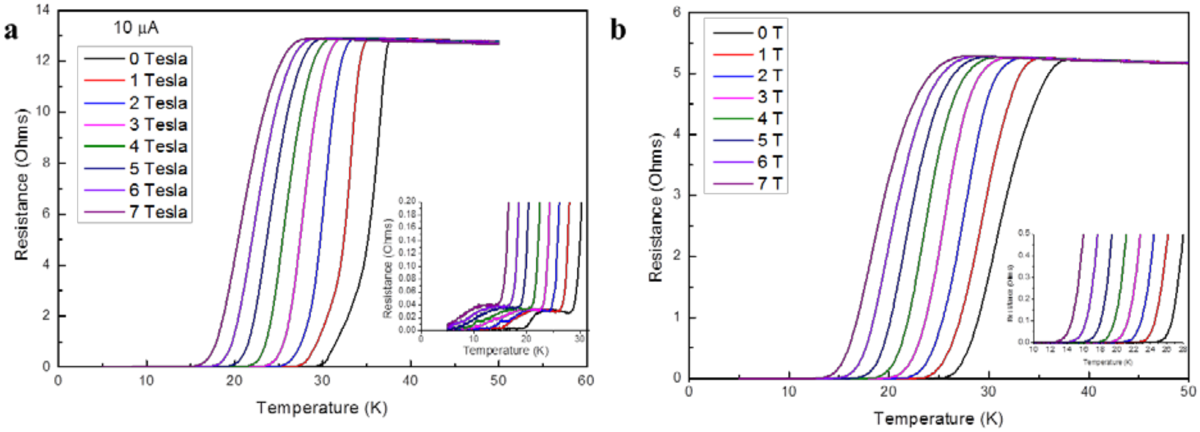

Figure 5. 17: Transport properties of MgB_2/CNT yarns: a) sample A; b) sample B.

The critical field dependence on temperature for MgB_2 has specific features including linear dependence and positive curvature at temperatures near T_c [89]. The high-field H_{c2} characteristics for our likely carbon-doped MgB_2/CNT yarns are improved compared with those for bulk MgB_2 wire [68], which agrees with earlier findings for carbon-doped MgB_2 [83]. Higher H_{c2} and higher T_c of sample A suggests better crystallinity and bigger MgB_2 grains (Figure 17). Although there is a pure connectivity between grains and possibly CNT connected regions which increases the amount of Josephson junction and weak links. Since Josephson junctions have lower irreversibility field (H_{irr}), the overall H_{irr} of sample A is significantly lower than in sample B.

The critical current was determined by I-V measurements at different fields at 4.2 K using a voltage criterion of 1 μV/cm (Figure 17). To compare yarns of different thicknesses and sizes, critical current was normalized by gravimetric density $\frac{J_c}{d}\left[\frac{A\cdot cm^3}{cm^2\cdot g}=\frac{A\cdot cm}{g}\right]$. MgB_2/CNT yarns' critical current is the same order of magnitude as bulk MgB_2 wires [68], which confirms high crystallinity and inter-grain connectivity along the wires. Sample B yarns have significantly higher critical temperatures due to low amount of Josephson junctions and weak links, comparal to Sample A. Also, improved pinning by grain boundaries and uniform defect distribution strengthens the critical field and critical current.

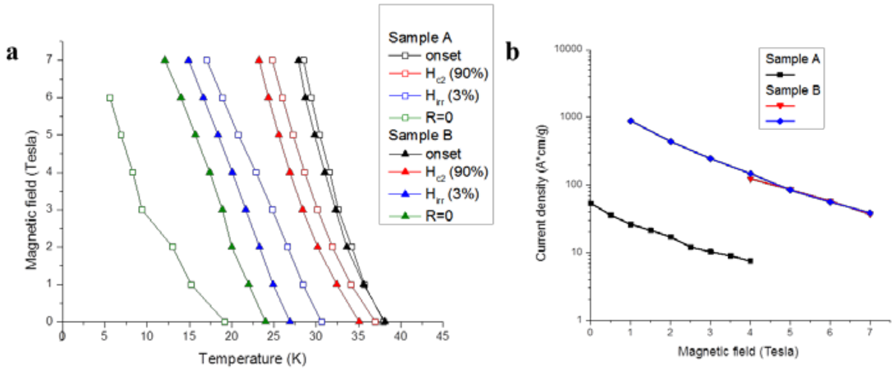

Figure 5. 18: a) upper and irreversibility fields for MgB_2/CNT yanrs; b) critical current density dependence on applied magnetic field at 4.2K.

5.4. LFMA: Low field microwave absorption in MgB2@CNT Superconductors

To understand the origin of superconducting characteristics of various samples, low-field microwave absorption spectroscopy (LFMA) is performed on the samples (fig. 2b). Hysteresis intensity is assigned to grain sizes while peak-to-peak intensity can be assigned to a Josephson junction network and describes the connectivity between grains.

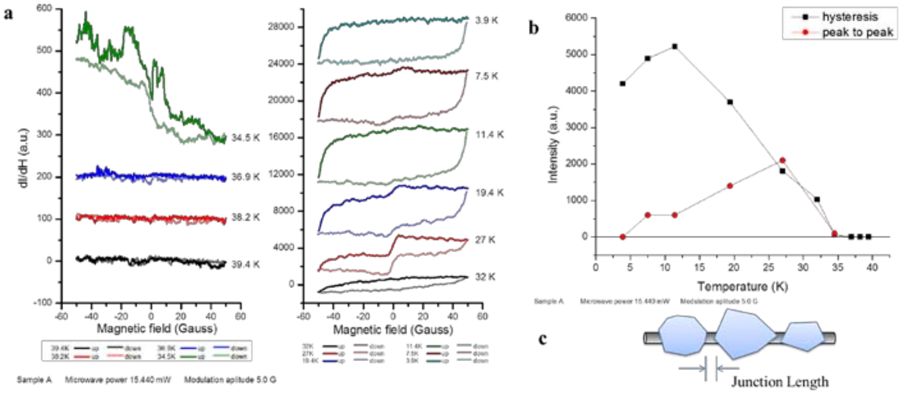

Figure 5. 19: a) LFMA scans at various temperatures for sample A; b) relative intensities of hysteresis and peak-to-peak value, defined from LFMA scans; c) schematics of morphology of sample A.

The correlation between the microscopy studies and the LFMA spectra are shown, with variation of grain size and morphology of interconnects in between. The large hysteresis of LFMA signal of the sample A suggests a big grain size (Figure 18). Although JJ network has a low pinning strength, which is described by peak-to-peak intensity on LFMA curves. That can be explained by large junction length (Figure 18c). Large peak-to-peak intensity of LFMA signal of the sample B at temperature 15-30 K is due to the uniform JJ network and the strong vortex pinning (Figure 19). The grain size is smaller in the sample B than in the sample A, since the hysteresis is not that significant. So the intragrain boundaries serve as effective pinning centers.

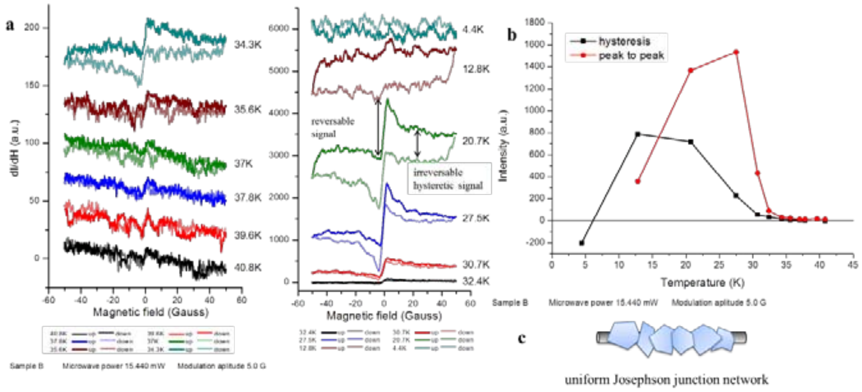

Figure 5. 20: a) LFMA scans at various temperatures for sample B; b) relative intensities of hysteresis and peak-to-peak value, defined from LFMA scans; c) schematics of morphology of sample B.

By using Laser Assisted CVD of boron followed by Mg vapor treatment was possible to produce MgB_2 nanowires using CNTs as a template in the form of birolled mats or twisted yarns. The critical temperature reaches 38.6 K (onset), the critical field has linear temperature dependence. The presence of CNT increases the mechanical strength of networks, improves flux pinning and increases critical field and current. The transport measurements of the critical field and the critical current combined with the LFMA studies confirmed that a Josephson junction network is formed. Grain size, uniformity and distribution of pinning sites and weak junctions have a large influence on superconducting properties. Also important, these MgB_2-CNT composite yarns are highly flexible, in contrast with the case for conventional MgB_2 wires.
Our method for producing MgB_2/CNT composite yarns using MWNT sheets as a template has produced superconducting yarns having attractive properties. The critical temperature reaches 38 K, and the density-normalized critical currents and critical fields are comparable to those for bulk pure-MgB_2 superconducting wires. Unlike conventional MgB_2 wires, these MgB_2-CNT composite yarns are highly flexible. LFMA studies, combined with characterization of morphology and crystalline structure of MgB_2/CNT composite yarns, demonstrate the importance of pinning centers and Josephson junction networks on superconducting properties.
Although we have already developed superconducting MgB_2/CNT sheets and yarns, there is more improvement and study that needs to be done to extend this approach to other layered superconductors, such as FeSeTe coated on CNT:

Part 6. Search for SC-ty upon doping in CNT, and nanocomposits with CNT, graphene and diamond

6.1. Doping by ion implantation by P and S
6.2. Ion implantation into MWCNT sheets: unusual negative resistance behavior
6.1 Post-synthesis doping:

Chemical doping of various forms of sp^2 carbons have been studied extensively since 1920 beginning with graphite intercalation compounds [7]. Based on this existing research, Eklund's group developed a novel post-synthesis chemical method to dope SWNTs [8]. However, the success of this method was limited since the high stability of the $C=C$ bond in a SWNT makes it difficult to substitute a dopant atom. Furthermore, this method uses corrosive gases such NH_3 resulting in significant.3. Superconductivity in Boron doped diamond,
structural damage to the tube deteriorating its electrical properties. For this reason, Clemson team developed a modified Eklund method to dope B, N, S, and P in SWNTs, MWNTs, and graphene. Such a modified Eklund approach (MEA) is advantageous since it is less time consuming, allows controllable doping, and is applicable to many carbon allotropes. In this process, high purity SWNTs (obtained from Nanomaterial Store. Product No: SN2102) are refluxed in a H_2O_2/HCl mixture for 72 hours to
Figure 5.8. SEM of pnictide powder on CNT.

6.2.Puzzle of negative resistance observed in ion implanted MWCNTs at low T< 5 K.

Dense network of interconnected CNTs resulted in
strongly negative R(T) (??) at lowest T<5-10 K

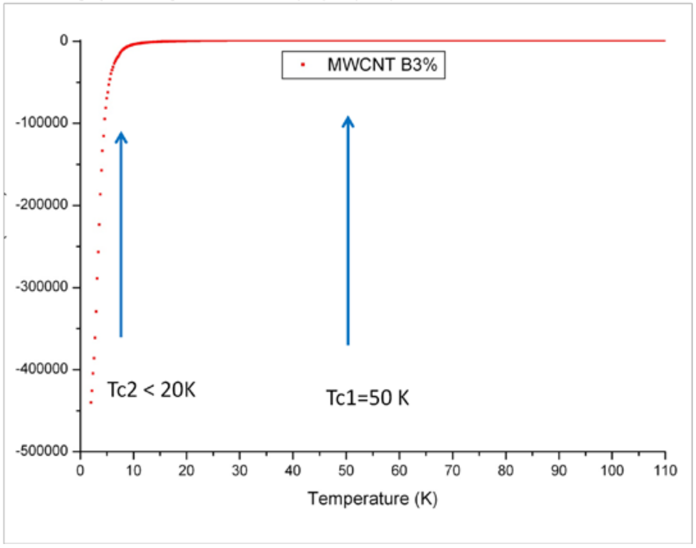

Of course all resistances in CNT network are positive !.

2. However due to non-homogeneous spatially contacts to the 3-D porous network The 4 probe contacts create inherent “Wheatstone bridges”, which become imbalanced with T and can show effective negative V and neg R(T) in I-V curves.
3. Current dependent R(T) can phenomenologically explain nearly all experimental findings of observed puzzle, particularly the functional shape of I-V
4. The real origin of the dependence of Rx on I/Io is not clear though. However a superconducting critical current is a good candidate for Imin, since it becomes zero at Tc
5. Different explanation might be possible, such as Coulomb blockade or similar

Non-ideal 4 probe connection, with V leads connected to different CNT bundle paths

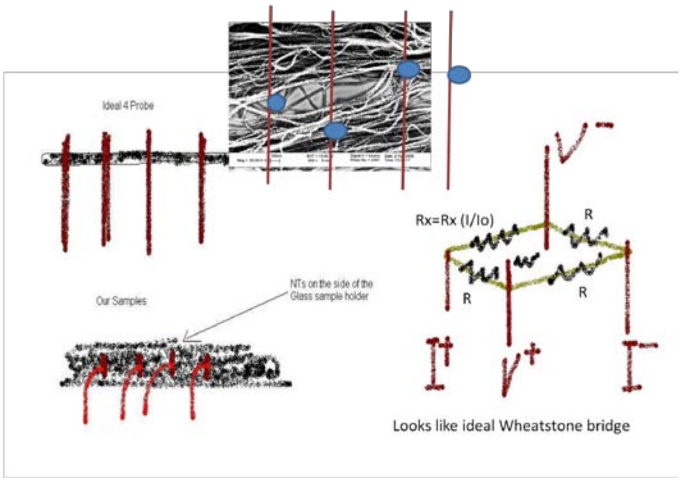

Looks like ideal Wheatstone bridge

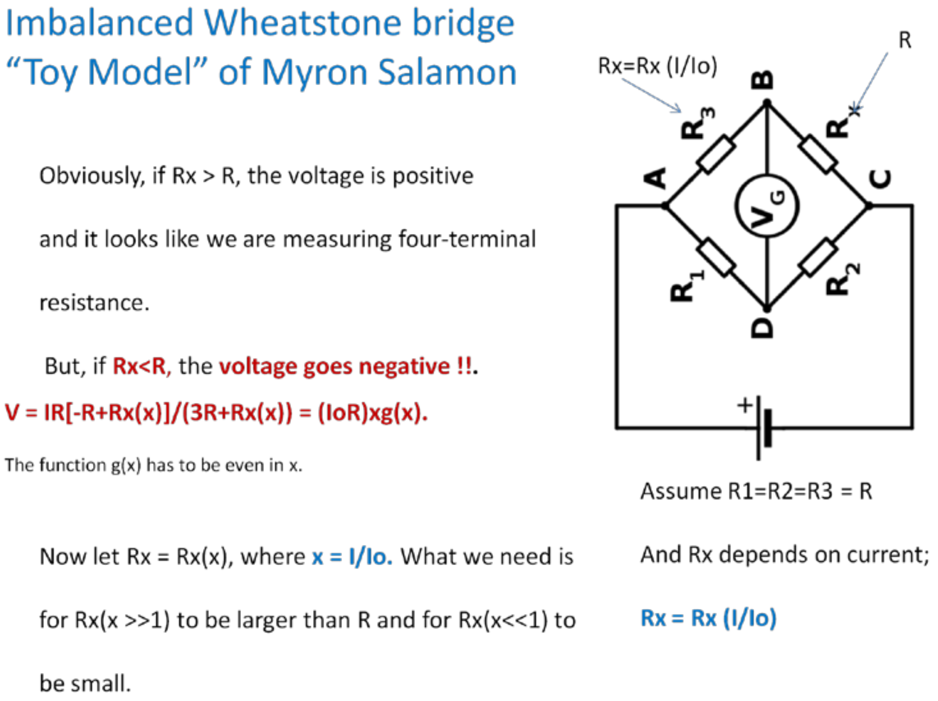

Imbalanced Wheatstone bridge
"Toy Model" of Myron Salamon

Obviously, if Rx > R, the voltage is positive and it looks like we are measuring four-terminal resistance.

But, if **Rx<R**, the **voltage goes negative !!**.

V = IR[-R+Rx(x)]/(3R+Rx(x)) = (IoR)xg(x).

The function g(x) has to be even in x.

Now let Rx = Rx(x), where **x = I/Io.** What we need is for Rx(x >>1) to be larger than R and for Rx(x<<1) to be small.

Assume R1=R2=R3 = R

And Rx depends on current;

Rx = Rx (I/Io)

So the puzzle of negative R<0 can be explained as strongly inhomogeneous network of CNT with 4 contacts.
It still does not disprove the possibility of superconducting small islands of CNt within a non-R network.

This demonstrates the complexity to obtain clear evidence of SC-ty in MWCNTs.

Task 5. 2 Synthesis of nanocomposites- Previously**,** Prof. Baughman's group showed that spontaneous a forest of aligned nanotubes could be drawn into MWNT yarns and sheets. Further, they have coated bi-scrolled nanotube yarns with 99 wt% of MgB2 to obtain superconducting yarn. However, the yarns are not robust and exhibit weaker mechanical properties compared to pristine yarns. Our approach is to achieve robust superconducting composites using buckypapers with lower percentages of MgB2. Further, we aim to improve the critical current and critical field in MgB2 by vortex pinning. To this end, we have successfully prepared multiwalled carbon nanotube (MWNT) bucky papers and impregnated them with MgB_2 using a solvent exfoliation and vacuum filtration process. This process yields bucky papers that exhibit strong Meissner effect. Briefly, 50 mg of MWNTs and MgB_2 (5, 10, or 25 wt %) were dispersed in 1 wt % aqueous solution of sodium dodecyl sulfate using 1/8" tip sonicator (Branson 250). Subsequently, the MWNT-MgB_2 dispersion was vacuum filtered using a 0.4□m Nylon filter paper. Finally, the filtered powder was air dried overnight at room temperature. For the convenience of discussion, the samples are labeled as MWNT-MgB2-X (X = 5, 10, or 25 wt % of MgB_2). As shown in Figure 9, the bulk MgB_2 powder (Figure 9a) breaks into sub-micron (0.5-1 □m; see Figure 9b) particles upon tip-sonication. The micro-morphology of the bucky paper changes considerably with increasing impregnation of MgB_2. At lower concentrations (5 and 10 wt% in Figures 9b and 9c) the MgB_2 particles decorate the MWNTs while micron-sized aggregates of MgB_2 are formed at high concentration of impregnation (25 wt%; Figure 9d).

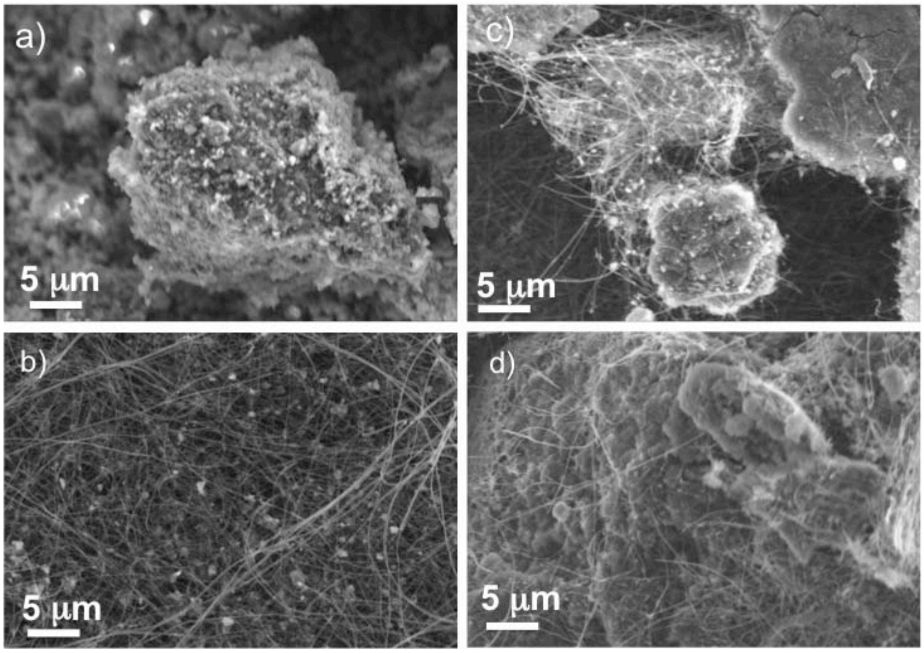

Figure 9: a) Bulk MgB_2 breaks into micron sized particles upon tip sonication for 30 mins. Panels b), c) and d) show images for MWNT-MgB2-5, 10 and 25 samples.

To gauge whether or not the increasing concentration of impregnated MgB_2 has modified the overall properties of the bucky paper, UTD team performed magnetic susceptibility measurements of MWNT-MgB2 bucky papers. As shown in Figure 10a (for MWNT-MgB2-5), the temperature (T) dependence of magnetization (M) was obtained at various fields in order to probe the vortex pinning induced by MWNTs. Firstly, as expected, all MWNT-MgB2 bucky papers exhibited Meissner effect at the same critical temperature as MgB_2 (~39 K at 10 Oe). It is noteworthy that the magnitude of zero field cooled (ZFC; shown by solid lines in Figure 10) susceptibility increased with increasing weight percent of MgB_2 in the impregnated bucky paper. The MWNT-MgB2-25 samples exhibited an increasingly strong diamagnetic response (or field expulsion below the superconducting transition temperature) with increasing amounts of impregnated MgB_2.

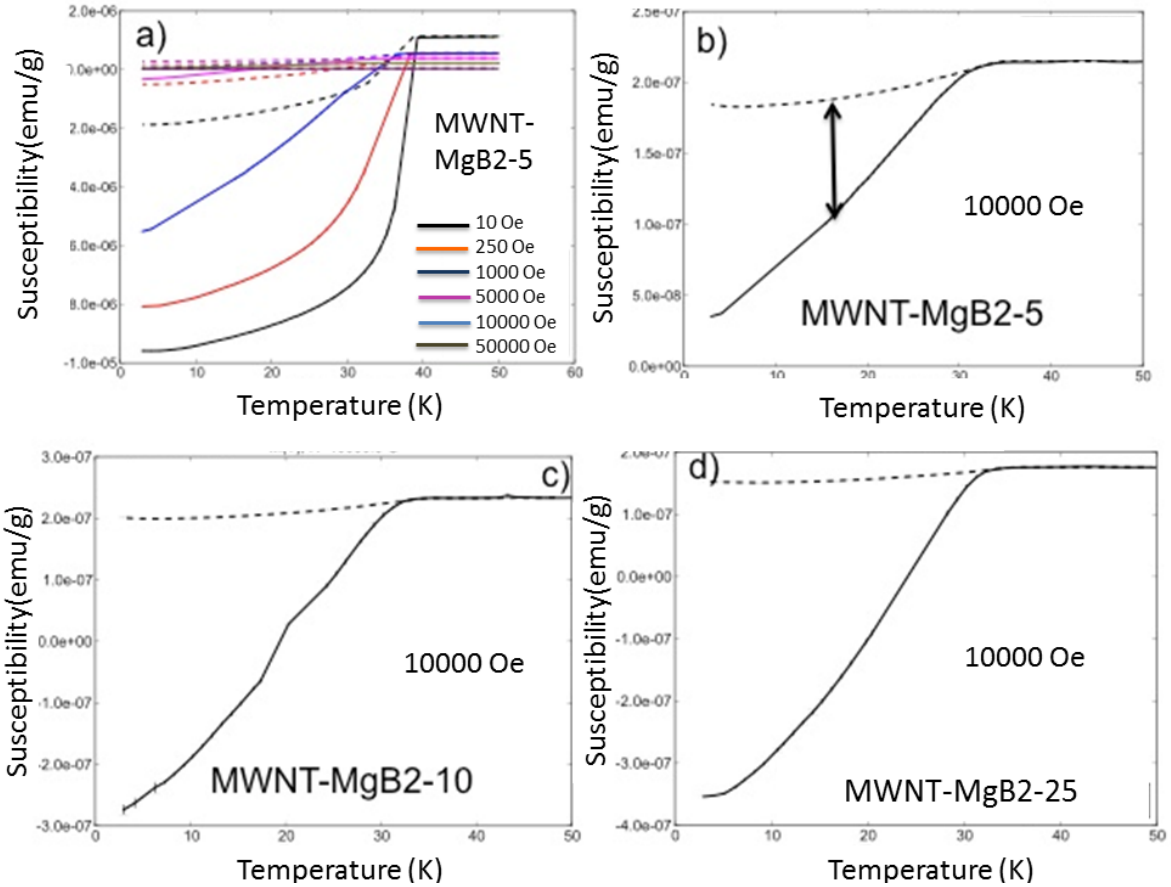

Figure 6. 10: a) FC and ZFC curves for MWNT-MgB2-5 at various fields show that the critical temperature decreases with increasing field. Panels b), c) and d) show the FC and ZFC curves for MWNT-MgB2-5, 10 and 25 samples. Clearly, the diamagnetic response below the critical temperatures increases with increasing concentration of impregnated MgB_2.

The observation of superconducting transition in transport measurements has been elusive in MgB2 composites prepared using filtration method. Therefore, we have used the 'Spark Plasma Sintering (SPS)' technique to prepare sandwiched MgB2-CNT structures shown in Fig. 11. Our initial experiments showed the presence of Meissner effect in spark-plasma sintered MgB_2-CNT sandwich structures. However, MgB_2 was found to change its crystal structure upon SPSing and as a result exhibited poor transport properties.

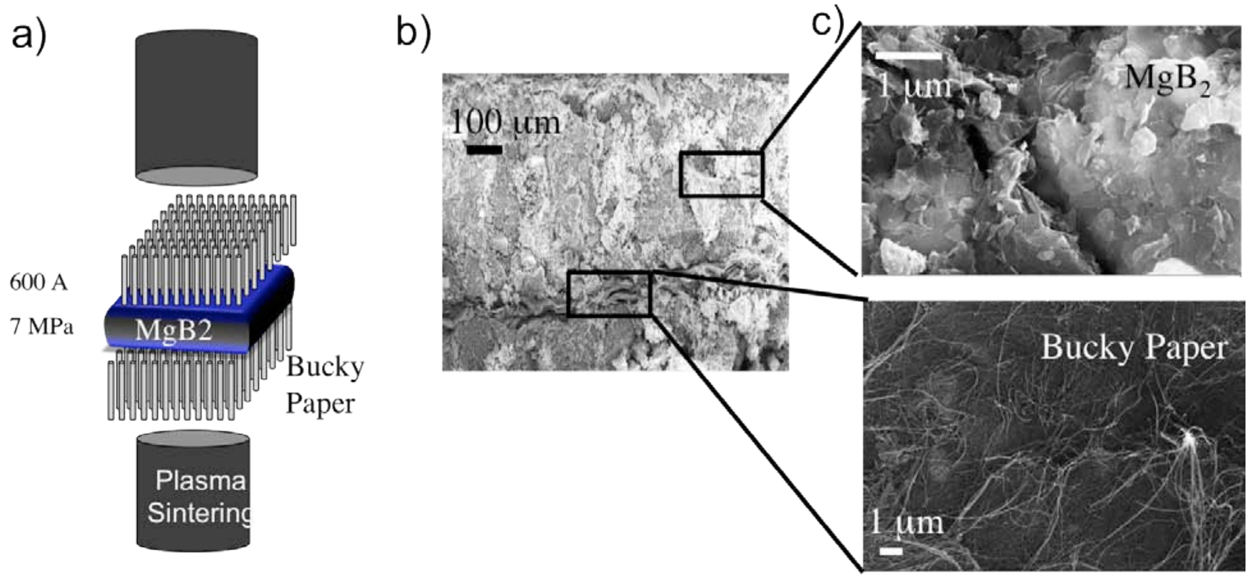

Figure 6. 11: a) A schematic showing the SPS process for preparing MgB2-CNT sandwich b) and c) show representative scanning electron microscope images of MgB2-CNT composites.

2.1 SPSed nanotube composited for superconductivity: Clemson team applied a new technique, namely, spark plasma sintering (SPS), to control the inter-tube spacing and the type of bonding in aligned MWNTs and Buckypaper of randomly oriented MWNTs. The SPS technique is a pulsed plasma discharge process that can generate highly localized intensive heating over a short time. It can densify MWNTs to higher packing densities and/or turn the inter-tube bonding from van der Waals in a rope or yarn to robust sp^2, or even to an sp^3 bonding (in micro-diamond). In a bulk sample of MWNTs, the magnitude and temperature dependence of the electrical resistance are often dominated by the inter-tube junctions, instead of being determined by the particular chirality and crystallography of each individual MWNT. In a generic sense, these inter-tube junctions should be treated as the electrical “leads”. We prepared several SPS samples of SWNTs and MWNTs for exploring superconductivity. Some of the samples showed extremely promising results in magnetization. For example, as shown in Fig. 12, SPSed SWNTs at 800 ^{o}C exhibited significant drop in magnetization along with exhibiting the characteristic M-H curve at 5 K. However, these samples did not exhibit any superconductivity in transport measurements suggesting that the superconducting volume is very small.

We have also utilized the SPS process to dope boron atoms into SWNT lattice. For this procees, arc-prepared SWNT bundles were soaked in boric acid solutions (H3BO3, 99.8%, Alfa Aesar) which contained increasing concentrations (x) of B. Boric acid powder and SWNT bundles were weighed and ultrasonicated for 5 min in ethanol to yield x = 0 at.%, 5 at.%, 7.5 at.%, 12.5 at.% and 15 at.% of B to C ratio in the mixture. The mixtures were vacuum dried and hand-ground for 10 min before loading into the graphite die (inner dia. ~1.25 cm) of the SPS system (SPS, Dr Sinter 1020, Sumitomo Coal Mining Co., Ltd., Japan). The powdered samples were sintered at 1200 ^{o}C under vacuum for 5 min into densified pellets. As shown in Fig. 13, the electrical conductivity results showed that the resistivity of these samples decreases with increasing boron concentration suggesting that SPS can effectively modify SWNT structure and inter-tube junctions [13]. However, we did not find any evidence for superconductivity in these samples possibly due to high resistance arising from tube-tube junctions.

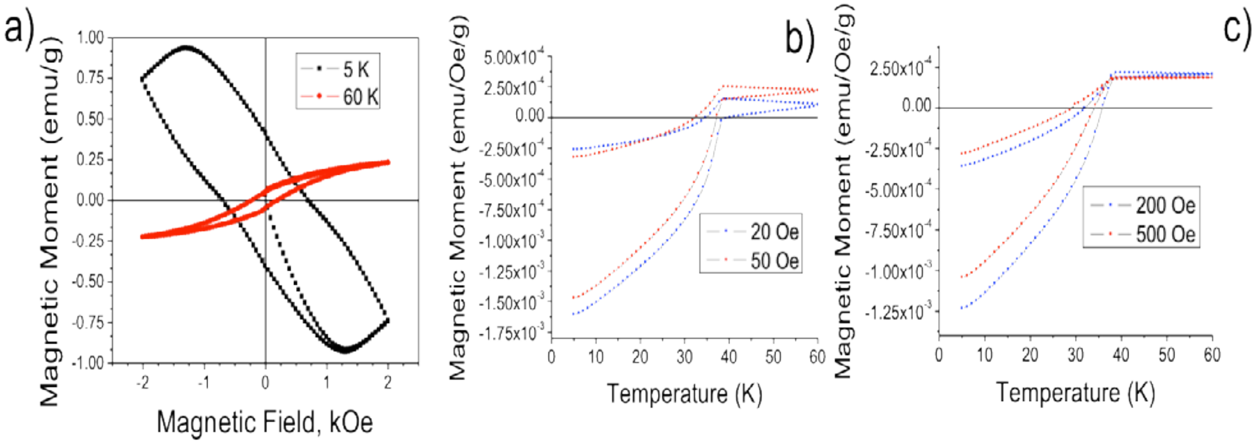

Figure 12: a) M-H curves for SWNTs SPSed at 800 C show the characteristic features of superconductivity, b) and c) show the drop in magnetization ~35 K indicating the presence of small superconducting volume.

Task 6. 3 Development of novel methods to identify the dopant configuration, environment, and bonding- The doping processes described in Task 1 and 2 do not necessarily result in a homogeneous distribution of heteroatoms in carbon nanostructures. For example, in the PLD method B substitution in the SWNT lattice is not necessarily uniform, and the formation of B nanodomains has been considered previously. The dopant-bonding environment can significantly influence superconducting properties of SWNTs. For this reason, quantifying the amount and bonding environments of B in the SWCNT lattice is highly important. Traditionally, researchers employ methods such as synchrotron based XPS and EELS to study the dopant configuration. However, these existing methods are time consuming, limited to single-crystal surfaces and incompatible with monitoring defects and dopants in nanomaterials with a high-throughput. In light of this, we have develop novel and facile methodologies to study surface states, dopant configurations, and defect chemistry through non-linear optical (NLO) spectroscopy. Dopant-induced changes in the electronic band structure of SWNTs are expected to influence their NLO properties. Indeed, Xie *et al*. predicted an enhancement in the second order hyper-polarizability in boron (B)-doped zigzag nanotubes due to the dopant-induced changes in the π electron cloud. We systematically studied the effects of substitutional B doping on the NLO properties of SWNTs by correlating open aperture Z-

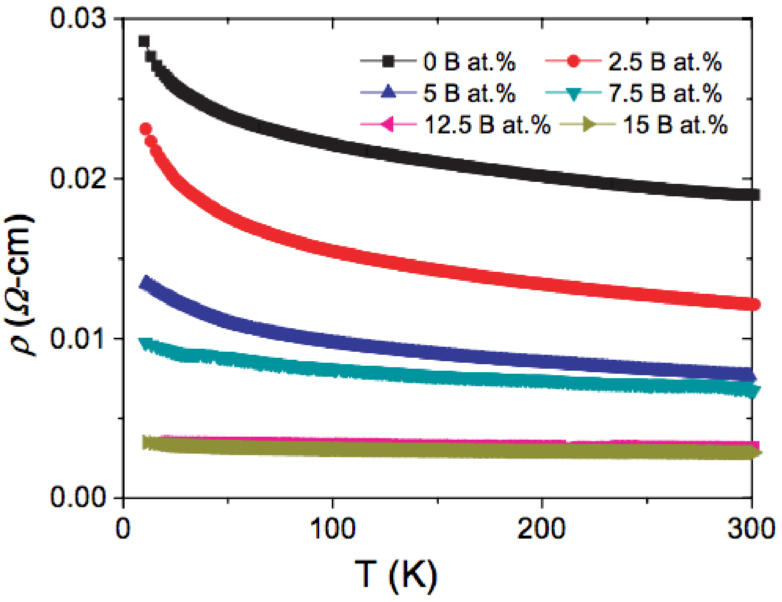

Figure 6.13: The temperature dependence of resistivity shows that the boron doping alters the electronic properties of SWNTs resulting in the lowering of net resistance

scan measurements (carried out in both nanosecond (ns) and femtosecond (fs) excitation regimes) with XPS and Raman spectroscopy. We found that in the ns excitation domain non-linear absorption increases with B doping, which is evident from the corresponding increase in two-photon absorption coefficient (β) seen in Fig. 14a. The increase of metallic character with doping underlies this direct correlation between doping levels and β. Therefore, it is possible to utilize NLO studies to get an estimation of dopant levels in SWNT lattice. As shown in Fig. 14b, a standardized plot of β values with respect to doping levels can assist in prompt preliminary screening of samples for further XPS studies.

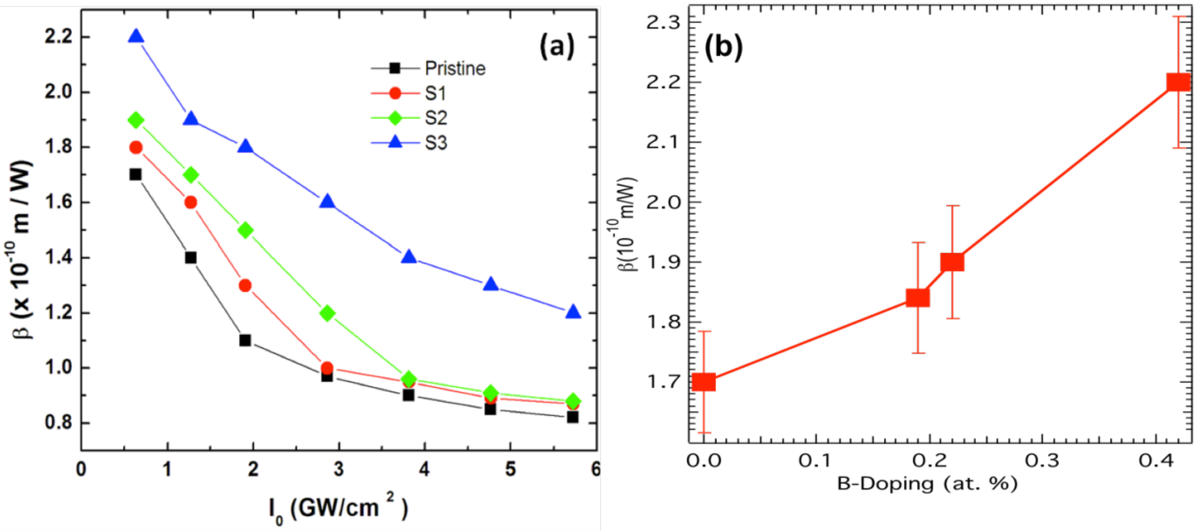

Figure 14: (a) The variation of the nonlinear absorption coefficient β with on-axis peak intensity I_o in the ns excitation regime suggesting excited state absorption in B-doped SWNTs when excited with the 532 nm photons. (b) The standardized correlation plot between nonlinear absorption coefficient and doping concentration allows one to promptly screen SWNT samples for determining the doping %

6.1.1 Nanocomposite of Ba-122 pnictide and CNT.

Attempts were made to combine polycrystalline $Ba(Fe_{0.91}Co_{0.09})_2As_2$ with carbon nanotubes with the aim of creating a superconducting yarn that is light, strong, and easily fabricated. Highly spinnable forests of multiwall CNT were drawn into sheets before having fine ground powder of $Ba(Fe_{0.91}Co_{0.09})_2As_2$ deposited on the surface before being twisted into yarns and then annealed. Under the strain of twisting, even separate particles on the surface of the nanotube sheet are confined inside the yarn at micrometer or nanometer scales. The tests with some of the first grown polycrystalline Ba122 pnictide samples were successfully spun into yarns, but were unable to replicate the superconducting transition in transport measurements of resistivity. Measurements of the magnetic susceptibility in the MPMS of the pnictide CNT composite as seen in figure 2.7 show that the robust grains of $Ba(Fe_{0.91}Co_{0.09})_2As_2$ still remain superconducting nevertheless, and as such continues to be a viable candidate for further superconducting wire

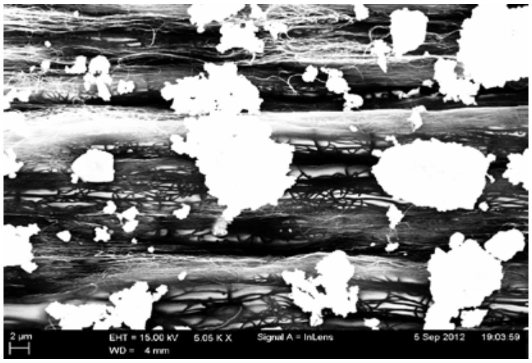

6.3.Boron doped diamond research.

Boron doped diamond created by colleagues in TISNUM (Troitsk, Moscow) has been studied by our complex methods and superconductivity has been proven by LFMA and M (T)< 0 methods. The structure of Boron-diamond single crystals is studied by multiple characterization tools and the bilayers of Boron hexagons are found to be the key motive of this superconductors. Heavily BDD have a 2D layer structure with a periodic lattice of hexagonal boron bilayers separated by a modulation period of 43 Å. Formation of the 2D boron bilayer structure changes significantly physical properties of BDD defining the origin of Mott and superconducting transitions. The superconducting transition is detected only on the surface of overdoped BDD (having a short bilayers modulation period), while the Mott transition occurs within the bulk crystal where equilibrium boron doping exists. We demonstrate that the vibrational Raman bands and electronic Raman scattering with the new shallow acceptor level at ~65 meV, whose origin was previously unclear, are surely associated with the hexagonal boron bilayers within the diamond matrix. The observation of 2D structure in BDD will help in understanding the nature of the metallic conductivity and superconductivity for other elements of the fourth group of the periodic table in which these phenomena can exist.

Part 7. Future Task 1: FeSeTe @CNT wires with high critical field Hc for power applications

7.1. FeSe0.1Te0.9 Deposited on Carbon Nanotubes (CNT).
7.2.Multiwall CNT forest dry drawn sheets: preliminary results
7.3.Singlewall CNT NanoComp & NanoEsko: promising preliminary results

7.3. $FeSe_{0.1}Te_{0.9}$ Deposited on Carbon Nanotubes

Multiwall Carbon Nanotube Substrates.

Samples were prepared on glass consisting of multiple layers of CNT sheets. These were drawn into aligned sheets from forests of nanotubes that were grown through CVD. These sheets could be densified via methanol to produce a more compact layer, but was not necessary for adhesion to the underlying glass. They were taken to TAMU and deposition was carried out in their

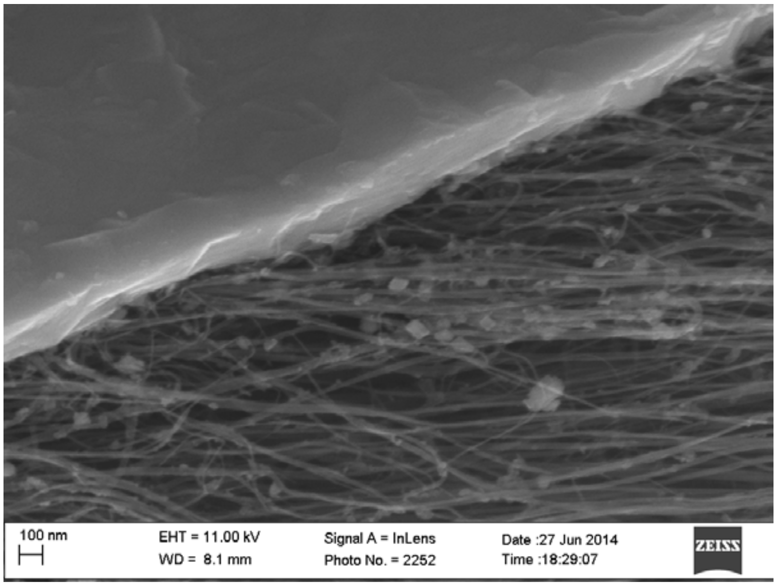

pulsed laser deposition (PLD) system using a target of $FeSe_{0.1}Te_{0.9}$ that was fabricated using standard solid state reaction methods. A layer of the iron chalcogenide approximately 100nm thick was deposited on various samples.

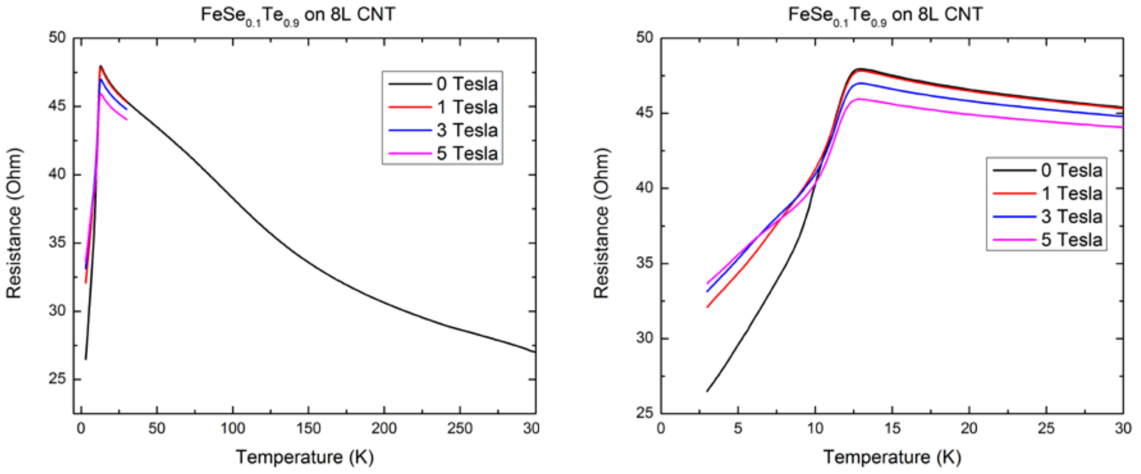

Figure 7.6. $FeSe_{0.1}Te_{0.9}$ deposited on eight layers of drawn CNT sheets.

In Fig. 7.6 above, the negative magnetoresistive character of the underlying CNT sheets can be clearly seen, showing a 6.28% decrease in the resistance at the peak. It has been shown that this behavior arises from a change in the density of states (DOS) near the Fermi level due to the applied magnetic fields perpendicular to the CNT axis forming 2D Landau states.[xiii]

The onset of the superconducting transition is visible, however, much like the thin films produced on substrates of glass, the resistance does not reach zero by 2K. This suggests the $FeSe_{0.1}Te_{0.9}$ film isn't continuous along the surface of the CNT and the islands of superconducting material are in competition with the insulating behavior of the CNT between them. Since the diameters of multiwall CNTs can be in excess of 15nm and can have twenty or more tubes per bundle, the surface is very rough.

7.3.Single wall Carbon Nanotube SWCNT Substrates

Samples were prepared on glass of two brands of singlewall CNT sheets, NanoComp and NanoEsko. Unlike the multiwall sheets drawn from the forest, these are not aligned in one direction. They were transferred to glass via methanol before having $FeSe_{0.1}Te_{0.9}$ deposited.

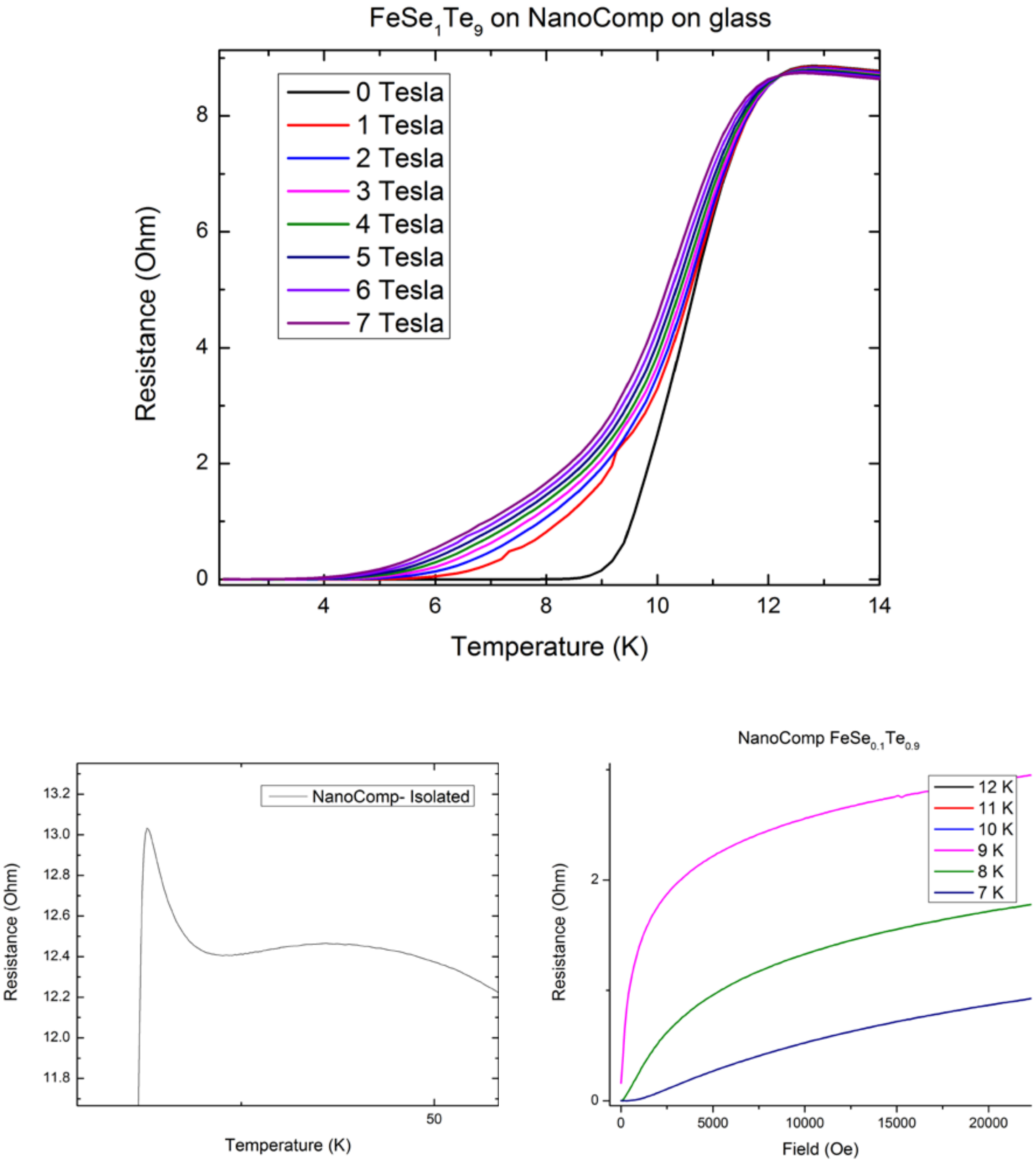

Figure 7. 7. FeSe0.1Te0.9 deposited on singlewall NanoComp

Both materials, NanoComp and NanoEsko, performed similarly as seen in Figs. 7 and 8. The magnetoresistance associated with CNTs is still present, though to a much lesser degree than in the multiwall tubes, due to a combination of greater connectivity in the unaligned network and decreased volume. The shift of the superconducting transition under applied magnetic field is also much more pronounced near zero resistance than even FeSe0.1Te0.9 on STO.

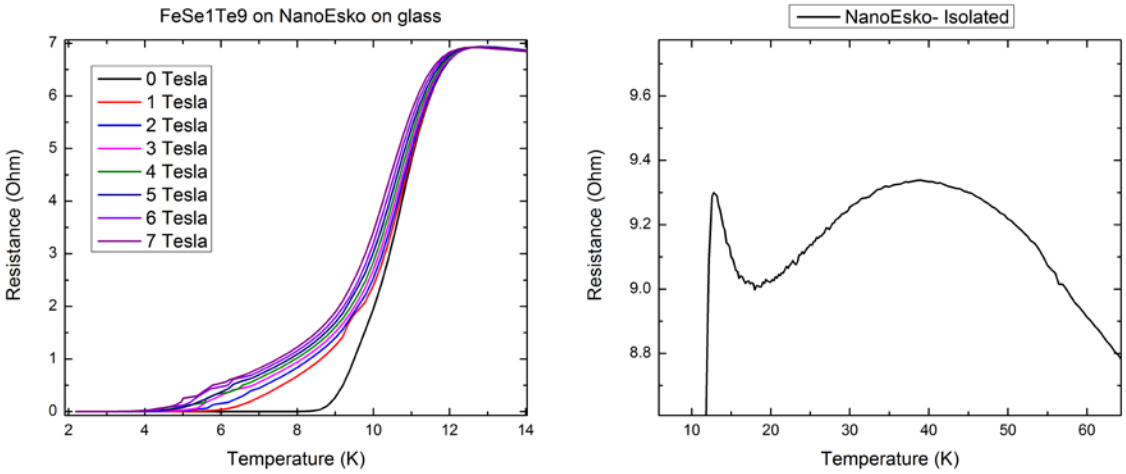

Figure 7. 8 FeSe0.1Te0.9 on singlewall NanoEsko

Figure 7. 9. SEM image of FeSe0.1Te0.9 on NanoComp

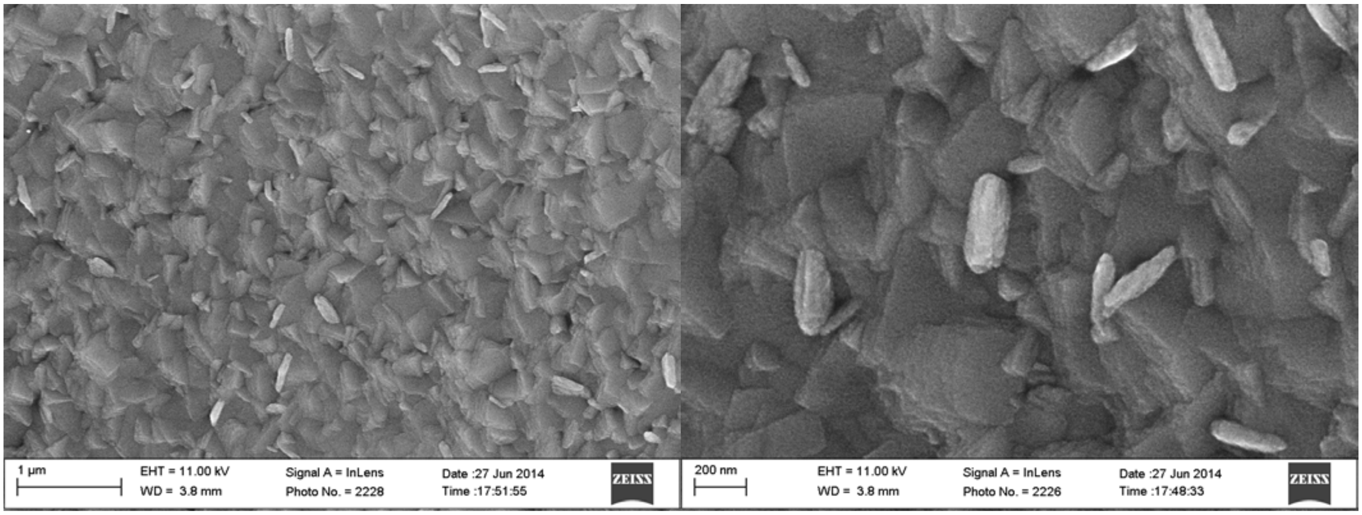

Figure 10. SEM images of FeSe0.1Te0.9 on NanoEsko

Part 8. Future Task 2: 8.1. High Field Investigation of FeSe0.1Te0.9 Thin Film.

Pulsed field measurements carried out at the National High Magnetic Field Laboratory (LANL) showed the actual upper critical field to reach 45 T at low temperatures. While much lower than the WHH estimate, it significantly exceeds the Pauli limit for paramagnetic pair breaking. The Kondo effect type behavior of R(T) clearly observed just above Tc can be the possible reason for such high Hc. The work on this important problem is going on in LANL despite the formally finished project. If the project will be extended more data will be obtained on systematically created FeSeTe films on different substrates, including SWCNT sheets and yarns.

8.2.Search for Tc > 100 K single atomic and Few Layer FeSeTe

Few atomic layer films of FeSe and interfacial superconductivity

One unit-cell thick films of FeSe grown on $SrTiO_3$ substrates by molecular beam epitaxy were shown to have signatures of a superconducting transition at 50K in transport measurements.[xiv] Through scanning tunneling microscopy, a superconducting gap as large as 20 meV was observed suggesting the possibility of superconductivity occurring above 77K. It is argued that the epitaxial strain on the single unit-cell layer is too weak to account for the observed value of Tc. The possibility of interface effects, such as interface enhanced electron-phonon coupling, or a polaronic effect associated with the high dielectric constant of STO are suggested.

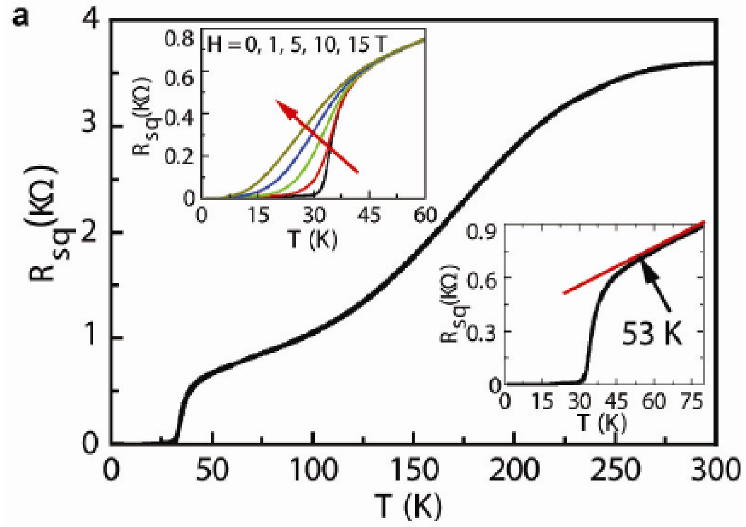

Figure 8.3: Transport measurements of 1 unit-cell thick FeSe film.[xv]

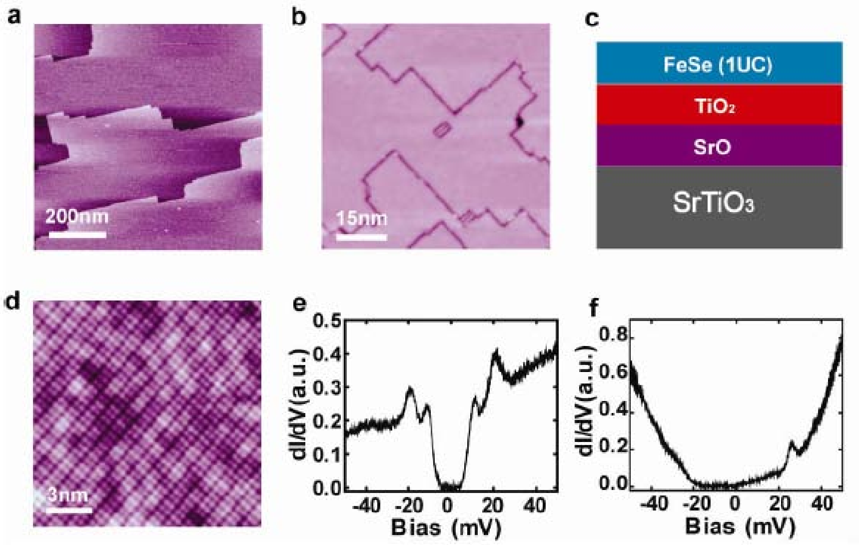

Figure 8.4: (a,b,d)STM topography of 1 unit-cell thick film of FeSe. (c) Schematic diagram of the films (e) Tunneling spectrum at 4.2K revealing superconducting gap. (f) Tunneling spectrum on a 2 unit-cell thick film revealing semiconductor-like behavior.

LFMA in few layer FeSe:

Our LFMA investigation of few layer FeSe@STO has proven the existence of superconducting LFMA appearing below Tc=29 K. it correspons to published by several groups transport resistance zero: R = 0 exactly at t=29 K. this clearly demonstrated that existanse of LFMA in 2-D systems like few layers is related with true R=0. While at the initial drop of r at 56 k there is no LFMA observed.

Summary of Accomplishments and New findings and Conclusion

1. Low-field microwave absorption (LFMA) method has been developed in UTD both as a unique device with closed cycle cryostat and as a powerful and ultra-sensitive analytical technique for search of superconductivity in nanogram amounts of novel materials. It has been demonstrated that LFMA can be used as an ultimate test to prove superconductivity existence if either zero resistance R=0, or Meisner effect M(T)<0 can not be clearly proven.

2. LFMA test has been used for characterizing complex, multiphase superconducting materials such as the (Pr,Ca)122 and (Pr,Ca)112 single crystalline systems. We have demonstrated the ability to detect small volume fraction of lower Tc1 by hysteretic LFMA in SC phases in both Pr-doped Ca 112 and 122 systems, and even smaller volumes of "interfacial" phases of the higher T_{c2} phase in (Pr,Ca)122. Additionally, we have shown that the 122 and 112 systems do not behave similarly near $T1_c$, a fact which is only known from the complete absence of the narrow peak signal in the Ca 112 samples. Additional analysis will be required in order to fully understand the complicated nature of multiphase superconductivity in these electronically doped Ca 122 and 112 pnictides.

3. The claims of Superconductivity in BN-nanotubes and BCN-nanotubes synthesized (by Lisa Pfefferle team in Yale) based on M(T) curves with downturn at T in the range of 80-130 K, has been carefully checked by our methodology of triple test: R=0,M<0 and LFMA sharp non-zero dP/dH, and conclusion is made that M(T) mimicking Meissner effect was due to contamination of 1-D nanotubes by Co- catalyst residuals, that cannot be eliminated. SC-ing LFMA has not been found in numerous samples (checked and documented carefully in UTD). Based on this > 2 year studies the search of SC-ty in BC, BN and BCN has been determined as premature and those tasks has been stopped. Objectives has been redirected towards search for higher Tc in newly discovered 2-D layered chalcogenides (FeSe, FeSeTe and FeTe thin films) deposited by PLD on various substrates.

4. Boron doped SWCTs created in Japan by Haruyama team, and also CVD synthesized by PLD assisted method (by Clemson team of Apparao Rao) has been carefully tested by triple R=0, M<0, dP/dH LFMA test and M(T) curves of paramagnetic type have been obtained (always positive) with some unusual downturns mimicking Meissner effect.

Those curves are again assigned to residual Fe catalyst and Ni, Y and other magnetic transition metal catalysts residuals, that also screen LFMA and show as ferromagnetic resonance in ESR. However since never R=0 has been observed and LFMA has never showed a typical SC-ing hysteretic curves with characteristic phase and peak at zero H-field, the conclusion was made that earlier claims (published in PRL, PR, etc.) can not be confirmed by Occam's razor test. Numerous experiments with doping by P, S, and other elements have not given clear evidences of high Tc. Therefore at present moment the SC-ty in SWCNTs remains confirmed only at very low Tc and only in purely metallic tubes. Doping by B was not proven to increase Tc in SWCNTs.

5. Alkali metal doping of SWCNTs has been studied by LFMA and in some samples of KxSWCNT doped by K vapors in vacuumated ESR tubes non-zero LFMA has been observed at $T < 13$ K. This inspired the theoretical work on possible better SC-ing pairing in 1-d systems with intercalated ions surrounding 1-D chains. The experimental work needs to be concentrated on pure metallic and pure semiconducting SWCNTs once better samples will become available. The possibility of enhancing Tc in ionically intercalated SWCNT bundles (i.e. in AxSWCNT type systems) has been studied theoretically and promising results are obtained.

6. We introduced a mean field microscopic model to describe superconductivity in a bundle of a mixture of carbon nanotubes of different superconducting properties. We have theoretically studied the dependence of the spatially averaged superconducting gap on the fraction of doped semiconducting SWCNT (with a higher pairing strength) in the bundle at different temperatures. Note that for inhomogeneous nanoscale systems, the dependence for different concentrations may be nonlinear, as a manifestation of the breakdown of the bulk BCS theory. Indeed, our calculations of show that for the dependence has less steep slope. The reason is that the bundle is a highly inhomogeneous system with a pronounced inverse proximity effect. At , below the site percolation threshold for a 2D triangular lattice, the bundle can be seen as a collection of finite islands of "good" superconductors (doped semiconducting nanotubes), diluted by normal or weakly superconducting material (metallic nanotubes). Such islands demonstrate significantly the suppressed superconductivity, even in the mean field description, due to the enhanced inverse proximity effect.

7. In quasi-one-dimensional systems with the intercalation-type doping, the dynamical response of dopant ions can substantially affect the interplay of density-wave and superconducting instabilities. We study a generic model of the system of Coulombically coupled Luttinger-liquid chains modified by the Coulomb interaction with displacements of dopant ions. Our interest is in the macroscopic, long wave-length, effects of the ionic response. Just as in the simpler one-dimensional electron-phonon case, the three-dimensional electron-ion model system is exactly solvable in the forward scattering channel allowing us to find the resulting system excitations and electron correlations. For

a jellium-like ion response, the effect of the bare electron-electron repulsion on the long-range correlations is essentially canceled by the ions with the effective electron-electron interactions now exhibiting regions of shorter-range repulsion and longer-range attraction. This picture is clarified and reproduced within the macroscopic dielectric function framework. If the system also features a non-polarizational interaction with another optical phonon mode, superconducting correlations can be developed already due to the forward-scattering only.

8. $FeSe_{0.1}Te_{0.9}$ thin films were deposited on single crystal $SrTiO_3$ (STO) (100) substrates by a pulse laser deposition (PLD) technique. CeO_2 nanolayer was introduced as either cap layer or buffer layer to investigate its pinning effects in $FeSe_{0.1}Te_{0.9}$ thin films. The results show improved film quality after doping with CeO_2 nanolayers, and no impurity phase was identified. All the samples achieve Tc of 12.5 K, and in-field Jc was greatly enhanced after doping with either cap or buffer CeO_2 nanolayer for the field range up to 7 T. The buffered one shows the best self-field J_c of 0.89 MA cm^{-2} at 4 K and a high upper critical field H_{c2} of 186 T as estimated by conventional WHH formula.

9. Te-rich iron chalcogenide ($FeSe_xTe_{1-x}$) thin films with a composition close to antiferromagnetic ordering have been deposited on $SrTiO_3$ (STO) substrates. The superconducting critical transition temperature (T_c) of the $FeSe_{0.1}Te_{0.9}$ thin film on STO substrate ranges from ~12.5 to ~13.3 K. The upper critical field is as high as 114 T, which is much higher than that of the $FeSe_{0.5}Te_{0.5}$ thin film on STO substrate (~49 T). The self-field critical current density (J_c^{sf}) at 2 K of 1.8×10^5 A cm^2 is much higher than that of the $FeSe_{0.5}Te_{0.5}$ thin film, and the $FeSe_{0.1}Te_{0.9}$ thin film also demonstrates superior pinning properties under applied magnetic field. Compared to $FeSe_{0.5}Te_{0.5}$, which was considered as the optimum composition, $FeSe_{0.1}Te_{0.9}$ presents even more promise for high field applications because of its high upper critical field and high critical current density.

10. Pulsed field measurements carried out at the National High Magnetic Field Laboratory (LANL) showed the actual upper critical field to reach 45 T at low temperatures. While much lower than the WHH estimate, it significantly exceeds the Pauli limit for paramagnetic pair breaking. The Kondo effect type behavior of R(T) clearly observed just above Tc can be the possible reason for such high Hc. The work on this important problem is going on in LANL despite the formally finished project. If the project will be extended more data will be obtained on systematically created FeSeTe films on different substrates, including SWCNT sheets and yarns.

11. In addition, we also tried to grow $FeSe_{0.5}Te_{0.5}$ thin films on amorphous glass substrates, to our surprise, the films show excellent superconducting properties even on amorphous glass substrates. Superconducting $FeSe_{0.5}Te_{0.5}$ thin films are deposited on amorphous substrates, i.e., glass substrates by a pulsed laser deposition (PLD) technique. Microstructural characterizations show that the films are highly textured along (00l) with good crystallinity. The superconducting critical transition temperature (T_c) ranges from 8 to 10 K. The self-field critical current density (J_c^{sf}) at 4 K is 1.2×10^4 A/cm^2. The in-field criticalcurrent density ($J_c^{in\text{-}field}$) decreases slowly under high magnetic field confirmed by

both transport and magnetization measurements. The growth of high quality superconducting $FeSe_{0.5}Te_{0.5}$ thin films on amorphous substrates demonstrates a low cost architecture for future Fe-based superconductor coated conductors.

12. Flexible, weavable and knottable superconducting magnesium diboride yarns have been fabricated that provide attractive gravimetric properties as a superconductor, while having a 20 times lower density than for bulk MgB_2. These yarns are made by templating forest-drawn carbon nanotube (CNT) aerogel sheets with boron using photothermal decomposition of BBr_3 produced by a scanned laser beam, conversion of the B-CNT nanofiber arrays to MgB_2-CNT sheets by exposure to Mg vapor, and twist spinning the MgB_2-CNT sheets into yarns. Carbon nanotubes in the MgB_2 structure serve as a strong conductive framework and provide carbon doping by creating scattering centers that improve the yarn's superconducting properties. Carbon nanotube sheets are laminated to MgB_2-CNT nanofiber sheets before the twist insertion process to additionally structurally reinforce the resulting yarns, and thereby produce strong flexible superconducting yarns whose bending strain before fracture exceeds 100-fold the value for high-temperature superconducting wires and tapes. While the nanoscale void volume in these knottable yarns is ~95%, the critical temperature (T_c) reaches 37.8 K and the gravimetric critical current density is over 10 times higher than for dense MgB_2 wires. The yarns remain superconducting even in regions that are tightly knotted. The high yarn porosity and associated large internal area will facilitate rapid cryogenic cooling and likely enable these very low density yarns to be used as a platform for evaluating the effect of infiltrated materials and electrochemical charge injection on superconductivity.

13. Boron doped diamond created by colleagues in TISNUM (Troitsk, Moscow) has been studied by our complex methods and superconductivity has been proven by LFMA and M (T)< 0 methods. The structure of Boron-diamond single crystals is studied by multiple characterization tools and the bilayers of Boron hexagons are found to be the key motive of this superconductors. Heavily BDD have a 2D layer structure with a periodic lattice of hexagonal boron bilayers separated by a modulation period of 43 Å. Formation of the 2D boron bilayer structure changes significantly physical properties of BDD defining the origin of Mott and superconducting transitions. The superconducting transition is detected only on the surface of overdoped BDD (having a short bilayers modulation period), while the Mott transition occurs within the bulk crystal where equilibrium boron doping exists. We demonstrate that the vibrational Raman bands and electronic Raman scattering with the new shallow acceptor level at ~65 meV, whose origin was previously unclear, are surely associated with the hexagonal boron bilayers within the diamond matrix. The observation of 2D structure in BDD will help in understanding the nature of the metallic conductivity and superconductivity for other elements of the fourth group of the periodic table in which these phenomena can exist.

Personnel supported

Ph.D. researchers partially supported: in UTD: Yu.N Gartstein, Ray Baughman, Myron Salamon, Anvar Zakhidov, and also as consultants: Ilya Grygorenko (LANL, CUNY)

Graduate Students partially supported on this project:
In UTD: Austin Howard, Julia Bykova, Nicholas Cornell, Alex Cook,
In Clemson Uni: Jason Reppert, Keqin Yang, Damien Howard, Rama Podila, Jingyi Zhu, Mehmet Karakaya and Luciana Oliveira. PI: Prof. Apparao Rao
In TAMU: Supported graduate students: Li Chen and Jijie Huang, PI: Ass. Prof. Haiyan Wang

Post doctoral fellows supported: Marcio Lima, Alexander Kuznetsov, Jonathan Yuen, Sezen Demirtas

Publications of team members related to program

Refereed Publications:

1. Microwave conductance of aligned multiwall carbon nanotube textile sheets
Brown, Brian L.; Bykova, Julia S.; Howard, Austin R.; A.Zakhidov, M. Lee.
APPLIED PHYSICS LETTERS Volume: 105 Issue: 26, 2014,

2. **“**Comparison of Pr-doped Ca 122 and Ca 112 Pnictides by Low-field Microwave Absorption Spectroscopy**”,** Austin R. Howard, Jonathan D. Yuen, Bing Lv, Myron Salamon, Ching-Wu Chu and Anvar A. Zakhidov**,** MRS Proceedings / Volume 1684 / 2014, pp.

3. Flexible, Ultralight, Porous Superconducting Yarns Containing Shell-Core Magnesium Diboride-Carbon Nanotube Nanofibers
Bykova, Julia S.; Lima, Marcio Dias; Haines, Carter S.; et al.
ADVANCED MATERIALS Volume: 26 Issue: 44 Pages: 7510-7515, 2014

1. Controlling the Optical, Electrical and Chemical Properties of Carbon Inverse Opal by Nitrogen Doping
Morelos-Gomez, Aaron; Mani-Gonzalez, Pierre G.; Aliev, Ali E.; A. Zakhidov
ADVANCED FUNCTIONAL MATERIALS Volume: 24 Issue: 18 Pages: 2612-2619

2. Superconducting properties of FeSexTe1-x thin film with a composition close to antiferromagnetic ordering
By: Chen, Li; Huang, Jijie; Tsai, Chen-Fong; N. Cornell, M.Salamon, A. Zakhidov, H. Wang
SUPERCONDUCTOR SCIENCE & TECHNOLOGY Volume: 26 Issue: 11 NOV 2013

3. Ionic plasma screening and long-range electron correlations in quasi-one-dimensional conductors
Gartstein, Yu N.; Zakhidov, A. A.
PHYSICS LETTERS A Volume: 377 Issue: 19-20 Pages: 1390-1394

4. Tunable interplay between 3d and 4 f electrons in Co-doped iron pnictides
Shang, T.; Yang, L.; Chen, Y.; Zakhidov A., et al.

PHYSICAL REVIEW B Volume: 87 Issue: 7

5. Carbon nanotube/graphene nanocomposite as efficient counter electrodes in dye-sensitized solar cells
   Velten, Josef; Mozer, Attila J.; Li, Dan; Ray Baughman, A. Zakhidov
   NANOTECHNOLOGY Volume: 23 Issue: 8 (2013)

6. Anand, B., Podila, R., Ayala, P., Oliveira, L., Philip, R., Sai, S. S. S., Zakhidov, A. A., Rao, A. M. Non-linear optical properties of B-doped single-walled carbon nanotube, *Nanoscale* accepted (2013)

7. Diamond Direct and Inverse Opal Matrices Produced by Chemical Vapor Deposition
   Ralchenko, V. G.; Sovyk, D. N.; Bolshakov, A. P.; et al.
   PHYSICS OF THE SOLID STATE Volume: 53 Issue: 6 Pages: 1131-1134,

8. Biscrolling Nanotube Sheets and Functional Guests into Yarns
   Lima, Marcio D.; Fang, Shaoli; Lepro, Xavier; et al.
   SCIENCE Volume: 331 Issue: 6013 Pages: 51-55

9. Fabrication of biscrolled fiber using carbon nanotube sheet", by R. H. Baughman, S. Fang, M. Lima, A. Zakhidov, et.al. PCT/US2010/036378 patent, 2010.

10. Structural Model for Dry-Drawing of Sheets and Yarns from Carbon Nanotube Forests
    Kuznetsov, Alexander A.; Fonseca, Alexandre F.; Baughman, Ray H.; et al.
    Source: ACS NANO Volume: 5 Issue: 2 Pages: 985-993

11. Ayala, P. *et al.* Evidence for substitutional boron in doped single-walled carbon nanotubes. *Applied Physics Letters* **96**, doi:18311010.1063/1.3427432 (2010).

12. Structure and process-dependent properties of solid-state spun carbon nanotube yarns
    Fang, Shaoli; Zhang, Mei; Zakhidov, Anvar A.; et al.
    JOURNAL OF PHYSICS-CONDENSED MATTER Volume: 22 Issue: 33, 2010

16. Podila, R. *et al.* Spectroscopic investigation of nitrogen doped graphene. *Applied Physics Letters* **101**, doi:12310810.1063/1.4752736 (2012).

17 Hitchcock, D., Yang, K. Q., He, J. & Rao, A. M. Electrical Transport Properties Of Single-Walled Carbon Nanotube Bundles Treated With Boric Acid. *Nano* **6**, 337-341, (2011).

18. Yang, K. Q. *et al.* Tuning electrical and thermal connectivity in multiwalled carbon nanotube buckypaper. *Journal of Physics-Condensed Matter* **22**, /22/33/334215 (2010).

19. Yang, K. Q. *et al.* Inter-tube bonding, graphene formation and anisotropic transport properties in spark plasma sintered multi-wall carbon nanotube arrays. *Carbon* **48**, 756-762, 2010).

20. Podila, R., Rao, R., Tsuchikawa, R., Ishigami, M. & Rao, A. M. Raman Spectroscopy of Folded and Scrolled Graphene. *ACS Nano* **6**, 5784-5790, (2012).

21. Rao, R. *et al.* Effects of Layer Stacking on the Combination Raman Modes in Graphene. *ACS Nano* **5**, 1594-1599, (2011).

22. J. Zhu, L. Oliveira, R. Podila, J. He, M. Skove, A. Howard, A. A. Zakhidov, and A. M. Rao, Magnetization Study of Sulfur-doped Graphitic Nano-platelets and Single Walled Carbon Nanotubes

23. L. Chen, J. Huang, C.-F. Tsai, Y. Zhu, J. Jian, A. Chen, Z. Bi, F. Khatkhatay, N. Cornell, A. Zakhidov, and H. Wang, *Supercond. Sci. Technol.* **26,** 112001 (2013)

24. L. Chen, C.-F. Tsai, J. H. Lee, X. Zhang, and H. Wang, *Jpn. J. Appl. Phys.* **52,** 020201 (2013)

25. J. Huang, L. Chen, J. Jian, F. Khatkhatay, and H. Wang, *Supercond. Sci. Technol.* **27,** 105006 (2014)

26. Ilya Grigorenko and Anvar Zakhidov, “Superconductivity in an Inhomogeneous Bundle of Metallic and Semiconducting Nanotubes”, Journal of Nanotechnology Volume 2013 (2013), Article ID 367270, 6 pages

27. D. Vandervelde, H. Q. Yuan, Y. Onuki and M. B. Salamon, “Evidence of d-wave pairing symmetry of the gap of the heavy-fermion superconductor CeIrIn$_5$ from magnetic-penetration-depth measurements,” Phys. Rev. B **79**, 212505 (1-4) (2009).

28. J. Chen, M. B. Salamon, S. Akutagawa, J. Akimitsu, J. Singleton, J. L. Zhang, L. Jiao, and H. Q. Yuan “Evidence of nodal gap structure in the noncentrosymmetric superconductor $Y_2 C_3$” Phys. Rev. B **83,** 144529/1-4 (2011).

29. X. Y. Tee, H. G. Luo, T. Xiang, D. Vandervelde, M. B. Salamon, H. Sugawara, H. Sato, C. Panagopoulos,1and Elbert E. M. Chia, Penetration-depth study of LaOs4Sb12: Multiband *s*-wave superconductivity, Phys. Rev. B **86**, 064518/1-5 (2012)

30. Ali E. Aliev, Ka Xiong, Kyeongjae Cho and M. B. Salamon, Reversible superconductivity in electrochromic indium-tin oxide films, Appl. Phys. Lett. **101**, 252603 (2012).

Ph.D. Dissertations prepared as a result of the Program:

31. Austin Ross Howard: MAGNETICALLY MODULATED MICROWAVE SPECTROSCOPY OF LAYERED AND QUASI-2D SUPERCONDUCTORS: IRON PNICTIDES AND CHALCOGENIDES, Thesis defended and published in UTD, 2014

32. Julia Sergeevna Bykova: CARBON NANOTUBE - MAGNESIUM DIBORIDE COMPOSITES FOR SUPERCONDUCTING YARNS, Thesis defended and published in UTD, 2014

32. Nicholas Ley Cornell: ELECTROPHYSICAL PROPERTIES OF LAYERED SUPERCONDUCTING NANOSTRUCTURES: ADVANCED SYNTHESIS AND TUNING, Thesis defended and published in UTD, 2014

Conference Presentations: The AFOSR funding supported at least 32 conference presentations at the APS and MRS meetings.
and Papers in preparation (only few shown below):

33. L. Chen, J. Huang, C.-F. Tsai, Y. Zhu, J. Jian, A. Chen, Z. Bi, F. Khatkhatay, N. Cornell, A. Zakhidov, and H. Wang, "Enhanced Superconducting Properties of $FeSe_{0.1}Te_{0.9}$ Thin Films on STO and Glass Substrates", Electronic Materials and Applications, Orlando, FL, 2014 (Oral Presentation)

34. J. Huang, L. Chen, J. Jian, F. Khatkhatay and H. Wang, "Enhanced Superconducting Properties of $FeSe_{0.1}Te_{0.9}$ Thin Films with CeO_2 Nanolayer" Applied Superconductivity Conference, Charlotte, NC, 2014 (Poster Presentation)

35. J. Huang, L. Chen, J. Jian, F. Khatkhatay and H. Wang, "Growth of iron chalcogenide thin films with enhanced pinning properties", Electronic Materials and Applications, Orlando, FL, 2015 (Oral Presentation)

36. Low-magnetic field microwave absorption and ESR in electronically doped CaFe2As2 : Evidence for Interfacial Superconducting Phase with Tc > 45 K
Austin Howard, Bing Lv,Ching-Wu Chu, Anvar Zakhidov, (prepared for submission to Phys. Rev. B),

37. Coexisting superconductivity and ferromagnetic ordering in Eu-based pnictides: Eu(Fe1-xRux)2As2 at x = 0.8, 0.2, 0.05, and EuFe2(As0.73P0.27)2 detected by ESR/LFMA, Austin Howard, Tian Shang, Jiaowen He, Caoguang Ha,Huiqui Yuan, Myron Salamon, Anvar Zakhidov,(Proc. Workshop on HTSC, 2012),

38. Higher Tc=45-49 K Phases separately detected by microwave absorption in low magnetic field in Electronically doped Ca 122, A.Howard, J.Yuen, M.Salamon, A.Zakhidov, B.Lv, C.W. Chu (in Proc. 16 US-Japan Workshop on Adv Supercond, (paper prepared for publication)

40. Interfacial high Tc~ 35-40 K superconductivity observed by ultrasensitive LFMA in single atomic layer FeSe film, A. Howard, J. Yuen, M.Salamon, A. Zakhidov, Q Xue, L.Bing, C.W.Chu (in preparation,)

Interaction/Transitions.

This program has been linked and partnering with two internationally funded AFOSR programs: And our interactions have been with those groups:

1. Search of SC in CNT by Haruyama in Japan, (Zakhidov visited Haruyama and got samples of Boron doped SWCNTs for LFMA studies)

2. Superconductivity at interfaces led by Yakov Kopelevich in Brazil in University of Campinas. Kopelevich has visited UTD twice and measurements were performed on CuCl samples and also studies of graphene@Si interfaces have been performed in UTD facilities by a student from Campinas

References:

1 Murata, N. *et al.* Superconductivity in thin films of boron-doped carbon nanotubes. *Physical Review Letters* **101**, doi:02700210.1103/PhysRevLett.101.027002 (2008).

2 Shi, W. *et al.* Superconductivity in Bundles of Double-Wall Carbon Nanotubes. *Scientific Reports* **2**, doi:62510.1038/srep00625 (2012).

3 Larkins, G. & Vlasov, Y. Indications of superconductivity in doped highly oriented pyrolytic graphite. *Superconductor Science & Technology* **24**, doi:092001 10.1088/0953-2048/24/9/092001 (2011).

4 McGuire, K. *et al.* Synthesis and Raman characterization of boron-doped single-walled carbon nanotubes. *Carbon* **43**, 219-227, doi:10.1016/j.cardon.2004.11.001 (2005).

5 Maciel, I. O. *et al.* Electron and phonon renormalization near charged defects in carbon nanotubes. *Nature Materials* **7**, 878-883, doi:10.1038/nmat2296 (2008).

6 Ayala, P. *et al.* Evidence for substitutional boron in doped single-walled carbon nanotubes. *Applied Physics Letters* **96**, doi:18311010.1063/1.3427432 (2010).

7 Falardeau, E. R., Foley, G. M. T., Zeller, C. & Vogel, F. L. VERY HIGH ELECTRICAL-CONDUCTIVITY IN ASF5-GRAPHITE INTERCALATION COMPOUNDS. *Journal of the Chemical Society-Chemical Communications*, 389-390, doi:10.1039/c39770000389 (1977).

8 Liu, X. M., Romero, H. E., Gutierrez, H. R., Adu, K. & Eklund, P. C. Transparent boron-doped carbon nanotube films. *Nano Letters* **8**, 2613-2619, doi:10.1021/nl0729734 (2008).

9 Anand, B., Podila, R., Ayala, P., Oliveira, L., Philip, R., Sai, S. S. S., Zakhidov, A. A., Rao, A. M. Non-linear optical properties of B-doped single-walled carbon nanotube, *Nanoscale* accepted (2013)

10 da Silva, R. R., Torres, J. H. S. & Kopelevich, Y. Indication of superconductivity at 35 K in graphite-sulfur composites. *Physical Review Letters* **87**, doi:147001 10.1103/PhysRevLett.87.147001 (2001).

11 Nair, R. R. *et al.* Spin-half paramagnetism in graphene induced by point defects. *Nature Physics* **8**, 199-202, doi:10.1038/nphys2183 (2012).

12 Podila, R. *et al.* Spectroscopic investigation of nitrogen doped graphene. *Applied Physics Letters* **101**, doi:12310810.1063/1.4752736 (2012).

13 Hitchcock, D., Yang, K. Q., He, J. & Rao, A. M. Electrical Transport Properties Of Single-Walled Carbon Nanotube Bundles Treated With Boric Acid. *Nano* **6**, 337-341, doi:10.1142/s1793292011002664 (2011).

14 Yang, K. Q. *et al.* Tuning electrical and thermal connectivity in multiwalled carbon nanotube buckypaper. *Journal of Physics-Condensed Matter* **22**, doi:334215 10.1088/0953-8984/22/33/334215 (2010).

15 Yang, K. Q. *et al.* Inter-tube bonding, graphene formation and anisotropic transport properties in spark plasma sintered multi-wall carbon nanotube arrays. *Carbon* **48**, 756-762, doi:10.1016/j.carbon.2009.10.022 (2010).

16 Podila, R., Rao, R., Tsuchikawa, R., Ishigami, M. & Rao, A. M. Raman Spectroscopy of Folded and Scrolled Graphene. *ACS Nano* **6**, 5784-5790, doi:10.1021/nn302331p (2012).

17 Rao, R. *et al.* Effects of Layer Stacking on the Combination Raman Modes in Graphene. *ACS Nano* **5**, 1594-1599, doi:10.1021/nn1031017 (2011).

18. J. Zhu, L. Oliveira, R. Podila, J. He, M. Skove, A. Howard, A. A. Zakhidov, and A. M. Rao, Magnetization Study of Sulfur-doped Graphitic Nano-platelets and Single Walled Carbon Nanotubes

[1] Iijima, Sumio. "Helical microtubules of graphitic carbon." *Nature* 354, (1991): 56-58.

[2] De Volder, Michael, Sameh Tawfick, Ray Baughman, and John A. Hart. "Carbon nanotubes: present and future commercial applications." *Science* 339, no. 6119 (2013): 535-539.

[3] Zhao, Yao, Jinquan Wei, Robert Vajtai, Pulickel Ajayan, and Enrique Barrera. "Iodine doped carbon nanotube cables exceeding specific electrical conductivity of metals." *Scientific reports* 1, (2011): 83.

[4] Behabtu, Natnael, Colin Young, Dmitri Tsentalovich, Olga Kleinerman, Xuan Wang, Anson Ma, E. Bengio, Ron ter Waarbeek, Jorrit de Jong, Ron Hoogerwerf, Steven Fairchild, John Ferguson, Benji Maruyama, Junichiro Kono, Yeshayahu Talmon, Yachin Cohen, Marcin Otto, and Matteo Pasquali. "Strong, light, multifunctional fibers of carbon nanotubes with ultrahigh conductivity." *Science* 339, no. 6116 (2013): 182-186.

[5] Hennrich, Frank, Sergei Lebedkin, Sharali Malik, Joseph Tracy, Matthias Barczewski, Harald Rösner, and Manfred Kappes. "Preparation, characterization and applications of free-standing single walled carbon nanotube thin films." *Physical Chemistry Chemical Physics* 4, (2002): 2273-2277.

[6] Xuewen, Wang, Li Guanghui, Liu Rui, Ding Haiyan, and Zhang Ting. "Reproducible layer-by-layer exfoliation for free-standing ultrathin films of single-walled carbon nanotubes." *Journal of Materials Chemistry* 22, (2012): 21824-21827.

[7] Gu, Hongwei, and Timothy Swager. "Fabrication of free-standing, conductive, and transparent carbon nanotube films." *Advanced Materials* 20, (2008): 4433-4437.

[8] Nasibulin, Albert, Antti Kaskela, Kimmo Mustonen, Anton Anisimov, Virginia Ruiz, Samuli Kivistö, Simas Rackauskas, Marina Timmermans, Marko Pudas, Brad Aitchison, Marko Kauppinen, David Brown, Oleg Okhotnikov, and Esko Kauppinen. "Multifunctional free-standing single-walled carbon nanotube films." *ACS Nano* 5, no. 4 (2011): 3214-3221.

[9] Zhang, M., S. L. Fang, A. A. Zakhidov, S. B. Lee, A. E. Aliev, C. D. Williams, K. R. Atkinson, and R. H. Baughman. "Strong, transparent, multifunctional, carbon nanotube sheets." *Science* 309, no. 5738 (2005): 1215-1219.

[10] Feng, Chen, Kai Liu, Jeah-Sheng Wu, Liang Liu, Jia-Shyong Cheng, Yuying Zhang, Yinghui Sun, Qunqing Li, Shoushan Fan, and Kaili Jiang. "Flexible, stretchable, transparent conducting films made from superaligned carbon nanotubes." *Advanced Functional Materials* 20, (2010): 885-891.

[11] Feng, C., K. Liu, J. S. Wu, L. Liu, J. S. Cheng, Y. Y. Zhang, Y. H. Sun, Q. Q. Li, S. S. Fan, and K. L. Jiang. "Flexible, Stretchable, Transparent Conducting Films Made from Superaligned Carbon Nanotubes." *Advanced Functional Materials* 20, no. 6 (2010): 885-891.

[12] Scardaci, Vittorio, Richard Coull, and Jonathan Coleman. "Very thin transparent, conductive carbon nanotube films on flexible substrates." *Applied Physics Letters* 97, (2010): 023114.

[13] Trancik, Jessika, Scott Barton, and James Hone. "Transparent and catalytic carbon nanotube films." *Nano Lett* 8, no. 4 (2008): 982-987.

[14] Jiang, K. L., J. P. Wang, Q. Q. Li, L. A. Liu, C. H. Liu, and S. S. Fan. "Superaligned carbon nanotube arrays, films, and yarns: a road to applications." *Advanced Materials* 23, no. 9 (2011): 1154-1161.

[15] Po, Riccardo, Chiara Carbonera, Andrea Bernardi, Francesca Tinti, and Nadia Camaioni. "Polymer- and carbon-based electrodes for polymer solar cells: toward low-cost, continuous fabrication over large area." *Solar Energy Materials and Solar Cells* 100, no. 0 (2012): 97-114.

[16] Aliev, Ali, Marcio Lima, Shaoli Fang, and Ray Baughman. "Underwater sound generation using carbon nanotube projectors." *Nano Lett* 10, no. 7 (2010): 2374-2380.

[17] Aliev, Ali, Yuri Gartstein, and Ray Baughman. "Increasing the efficiency of thermoacoustic carbon nanotube sound projectors." *Nanotechnology* 24, no. 23 (2013): 235501.

[18] Xiao, L., Z. Chen, C. Feng, L. Liu, Z. Q. Bai, Y. Wang, L. Qian, Y. Y. Zhang, Q. Q. Li, K. L. Jiang, and S. S. Fan. "Flexible, stretchable, transparent carbon nanotube thin film loudspeakers." *Nano Letters* 8, no. 12 (2008): 4539-4545.

[19] Kang, Byeong Gyun, Young Jin Lim, Kwang-Un Jeong, Kyu Lee, Young Hee Lee, and Seung Hee Lee. "A tunable carbon nanotube polarizer." *Nanotechnology* 21, no. 40 (2010).

[20] Kyoung, Jisoo, Eui Yun Jang, Márcio D. Lima, Hyeong-Ryeol Park, Raquel Ovalle Robles, Xavier Lepró, Yong Hyup Kim, Ray H. Baughman, and Dai-Sik Kim. "A reel-wound carbon nanotube polarizer for terahertz frequencies." *Nano Lett* 11, no. 10 (2011): 4227-4231.

[21] Jiang, K. L., Q. Q. Li, and S. S. Fan. "Spinning continuous carbon nanotube yarns - Carbon nanotubes weave their way into a range of imaginative macroscopic applications." *Nature Nanotechnology* 419, no. 6909 (2002): 801-801.

[22] Shoji, Satoru, Hidemasa Suzuki, Remo Proietti Zaccaria, Zouheir Sekkat, and Satoshi Kawata. "Optical polarizer made of uniaxially aligned short single-wall carbon nanotubes embedded in a polymer film." *Physical Review B* 77, no. 15 (2008): 153407.

[23] Aliev, Ali. "Bolometric detector on the basis of single-wall carbon nanotube/polymer composite." *Infrared Physics & Technology* 51, (2008): 541-545.

[24] Aliev, Ali E., Jiyoung Oh, Mikhail E. Kozlov, Alexander A. Kuznetsov, Shaoli Fang, Alexandre F. Fonseca, Raquel Ovalle, Márcio D. Lima, Mohammad H. Haque, Yuri N. Gartstein, Mei Zhang, Anvar A. Zakhidov, and Ray H. Baughman. "Giant-stroke, superelastic carbon nanotube aerogel muscles." *Science* 323, no. 5921 (2009): 1575-1578.

[25] Zhang, M., K. R. Atkinson, and R. H. Baughman. "Multifunctional carbon nanotube yarns by downsizing an ancient technology." *Science* 306, no. 5700 (2004): 1358-1361.

[26] Lima, M. D., S. L. Fang, X. Lepro, C. Lewis, R. Ovalle-Robles, J. Carretero-Gonzalez, E. Castillo-Martinez, M. E. Kozlov, J. Y. Oh, N. Rawat, C. S. Haines, M. H. Haque, V. Aare, S. Stoughton, A. A. Zakhidov, and R. H. Baughman. "Biscrolling nanotube sheets and functional guests into yarns." *Science* 331, no. 6013 (2011): 51-55.

[27] Yakobson, B., and R. Smalley. "Fullerene Nanotubes: C 1,000,000 and Beyond Some unusual new molecules—long, hollow fibers with tantalizing electronic and mechanical properties— …." *Am Scientist*, (1997).

[28] Yu, Files, Arepalli, and Ruoff. "Tensile loading of ropes of single wall carbon nanotubes and their mechanical properties." *Physical Review Letters* 84, no. 24 (2000): 5552-5555.

[29] Yu, Min-Feng, Oleg R. Lourie, Mark J. Dyer, Katerina Moloni, Thomas F. Kelly, and Rodney S. Ruoff. "Strength and breaking mechanism of multiwalled carbon nanotubes under tensile load." *Science (New York, N.Y.)* 287, no. 5453 (2000): 637-640.

[30] Yakobson, B., M. Campbell, C. Brabec, and J. Bernholc. "High strain rate fracture and C-chain unraveling in carbon nanotubes." *Computational Materials Science,* (1997).

[31] Javey, Ali, Jing Guo, Qian Wang, Mark Lundstrom, and Hongjie Dai. "Ballistic carbon nanotube field-effect transistors." *Nature* 424, no. 6949 (2003): 654-657.

[32] Li, H., W. Lu, J. Li, X. Bai, and C. Gu. "Multichannel ballistic transport in multiwall carbon nanotubes." *Physical Review Letters* 95, no. 8 (2005): 86601.

[33] Wei, B., R. Vajtai, and P. Ajayan. "Reliability and current carrying capacity of carbon nanotubes." *Applied physics Letters* 79, no. 8 (2001): 1172-1174.

[34] Yao, Zhen, Charles L. Kane, and Cees Dekker. "High-field electrical transport in single-wall carbon nanotubes." *Physical Review Letters* 84, no. 13 (2000): 2941-2944.

[35] Dai, Hongjie, Ali Javey, Eric Pop, David Mann, and Yuerui Lu. "Electrical transport properties and field-effect transistors of carbon nanotubes." *Nano: Brief Reports and Reviews* 1, no. 1 (2006): 1-13.

[36] Ma, Jun, Jie Tang, Han Zhang, Norio Shinya, and Lu-Chang Qin. "Ultrathin carbon nanotube fibrils of high electrochemical capacitance." *ACS Nano* 3, no. 11 (2009): 3679-3683.

[37] Berber, Savas, Young-Kyun Kwon, and David Tomanek. "Unusually high thermal conductivity of carbon nanotubes." *Physical Review Letters* 84, no. 20 (2000): 4613-4616.

[38] Anthony, T.R., W.F. Banholzer, J.F. Fleischer, Lanhua Wei, P.K. Kuo, R.L. Thomas, and R.W. Pryor. "Thermal diffusivity of isotopically enriched ^{12}C diamond." *Physical review. B, Condensed matter* 42, no. 2 (1990): 1104-1111.

[39] Haacke, G. "New figure of merit for transparent conductors." *Journal of Applied Physics* 47, no. 9 (1976): 4086-4089.

[40] Gordon, Roy G. "Criteria for choosing transparent conductors." *MRS Bulletin* 25, no. 8 (2000): 52-57.

[41] Dressel, Martin, and George Gruner. *Electrodynamics of solids: optical properties of electrons in matter*: Cambridge University Press, 2002.

[42] De, Sukanta, Paul King, Philip Lyons, Umar Khan, and Jonathan Coleman. "Size effects and the problem with percolation in nanostructured transparent conductors." *ACS Nano* 4, no. 12 (2010): 7064-7072.

[43] Michael, W. Rowell, and D. McGehee Michael. "Transparent electrode requirements for thin film solar cell modules." *Energy & Environmental Science* 4, (2011): 131-134.

[44] De, Sukanta, and Jonathan N. Coleman. "The effects of percolation in nanostructured transparent conductors." *MRS Bulletin* 36, no. 10 (2011): 774-781.

[45] Wu, Hui, Desheng Kong, Zhichao Ruan, Po-Chun Hsu, Shuang Wang, Zongfu Yu, Thomas Carney, Liangbing Hu, Shanhui Fan, and Yi Cui. "A transparent electrode based on a metal nanotrough network." *Nature nanotechnology* 8, no. 6 (2013): 421-425.

[46] Hecht, David, Amy Heintz, Roland Lee, Liangbing Hu, Bryon Moore, Chad Cucksey, and Steven Risser. "High conductivity transparent carbon nanotube films deposited from superacid." *Nanotechnology* 22, no. 7 (2011): 75201.

[47] Heer, W. A. de, W. S. Bacsa, A. Chatelain, T. Gerfin, R. Humphreybaker, L. Forro, and D. Ugarte. "Aligned carbon nanotubes films - production and optical and electronic properties." *Science* 268, no. 5212 (1995): 845-847.

[48] Garcia-Vidal, F., J. Pitarke, and J. Pendry. "Effective medium theory of the optical properties of aligned carbon nanotubes." *Physical Review Letters* 78, no. 22 (1997): 4289.

[49] Henrard, L., and Ph Lambin. "Calculation of the energy loss for an electron passing near giant fullerenes." *Journal of Physics B: Atomic Molecular and Optical Physics* 29, (1996): 5127-5141.

[50] Murakami, Yoichi, Erik Einarsson, Tadao Edamura, and Shigeo Maruyama. "Polarization dependence of the optical absorption of single-walled carbon nanotubes." *Physical Review Letters* 94, no. 8 (2005): 87402.

[51] Ren, Lei, Cary L. Pint, Takashi Arikawa, Kei Takeya, Iwao Kawayama, Masayoshi Tonouchi, Robert H. Hauge, and Junichiro Kono. "Broadband terahertz polarizers with ideal performance based on aligned carbon nanotube stacks." *Nano Lett* 12, (2012): 787-790.

[52] Bubke, Karsten, Harald Gnewuch, Martin Hempstead, Jens Hammer, and Malcom Green. "Optical anisotropy of dispersed carbon nanotubes induced by an electric field." *Applied Physics Letters* 71, no. 14 (1997): 1906-1908.

[53] Ma, Chen, Wei Zhang, Yuefeng Zhu, Lijun Ji, Renping Zhang, Nikhil Koratkar, and Ji Liang. "Alignment and dispersion of functionalized carbon nanotubes in polymer composites induced by an electric field." *Carbon* 46, no. 4 (2008): 706-710.

[54] Zhu, Yue-Feng, Chen Ma, Wei Zhang, Ren-Ping Zhang, Nikhil Koratkar, and Ji Liang. "Alignment of multiwalled carbon nanotubes in bulk epoxy composites via electric field." *Journal of Applied Physics* 105, no. 5 (2009).

[55] Walters, D., M. Casavant, X. Qin, C. Huffman, P. Boul, L. Ericson, E. Haroz, M. O'Connell, K. Smith, D. Colbert, and R. Smalley. "In-plane-aligned membranes of carbon nanotubes." *Chemical Physics Letters* 338, (2001): 14-20.

[56] Islam, M., D. Milkie, C. Kane, A. Yodh, and J. Kikkawa. "Direct measurement of the polarized optical absorption cross section of single-wall carbon nanotubes." *Physical Review Letters* 93, no. 3 (2004): 37404.

[57] Ichida, M., S. Mizuno, H. Kataura, Y. Achiba, and A. Nakamura. "Anisotropic optical properties of mechanically aligned single-walled carbon nanotubes in polymer." *Applied Physics a-Materials Science & Processing* 78, no. 8 (2004): 1117-1120.

[58] Kim, Y., N. Minami, and S. Kazaoui. "Highly polarized absorption and photoluminescence of stretch-aligned single-wall carbon nanotubes dispersed in gelatin films." *Applied Physics Letters,* (2005).

[59] Shimoda, H., S. Oh, H. Geng, R. Walker, X. Zhang, L. McNeil, and O. Zhou. "Self-assembly of carbon nanotubes." *Advanced Materials* 14, no. 2 (2002): 899-901.

[60] Yoo, S., Y. M. Jung, D. S. Lee, W. T. Han, K. Oh, Y. Murakami, T. Edamura, and S. Maruyama. "Optical anisotropy in single-walled carbon nanotubes." *Optics Letters* 30, no. 23 (2005): 3201-3203.

[61] Pint, Cary, Ya-Qiong Xu, Sharief Moghazy, Tonya Cherukuri, Noe Alvarez, Erik Haroz, Salma Mahzooni, Stephen Doorn, Junichiro Kono, Matteo Pasquali, and Robert Hauge. "Dry contact transfer printing of aligned carbon nanotube patterns and characterization of their optical properties for diameter distribution and alignment." *ACS Nano* 4, no. 2 (2010): 1131-1145.

[62] Choi, Hyoung Joon, David Roundy, Hong Sun, Marvin L. Cohen, and Steven G. Louie. "The origin of the anomalous superconducting properties of MgB_2." *Nature* 418, no. 6899 (2002): 758-760.

[63] Buzea, Cristina, and Tsutomu Yamashita. "Review of the superconducting properties of MgB_2." *Superconductor Science and Technology* 14, no. 11 (2001): R115.

[64] Moshchalkov, Victor, Mariela Menghini, T. Nishio, Q. H. Chen, A. V. Silhanek, V. H. Dao, L. F. Chibotaru, N. D. Zhigadlo, and J. Karpinski. "Type-1.5 superconductivity." *Physical Review Letters* 102, no. 11 (2009): 117001.

[65] Zhitomirsky, M., and V. H. Dao. "Ginzburg-Landau theory of vortices in a multigap superconductor." *Physical Review B,* (2004).

[66] Iavarone, M., G. Karapetrov, A. E. Koshelev, W. K. Kwok, G. W. Crabtree, D. G. Hinks, W. N. Kang, Eun-Mi Choi, Hyun Jung Kim, Hyeong-Jin Kim, and S. I. Lee. "Two-band superconductivity in MgB_2." *Physical Review Letters* 89, no. 18 (2002): 187002.

[67] Eisterer, M. "Magnetic properties and critical currents of MgB2." *Superconductor Science and Technology,* (2007).

[68] Canfield, P. C., D. K. Finnemore, S. L. Bud'ko, J. E. Ostenson, G. Lapertot, C. E. Cunningham, and C. Petrovic. "Superconductivity in dense MgB_2 wires." *Physical Review Letters* 86, no. 11 (2001): 2423.

[69] Eisterer, M. "Magnetic properties and critical currents of MgB_2." *Superconductor Science and Technology* 20, no. 12 (2007): R47.

[70] Hanna, Mina, Shufang Wang, Andrew David Eck, Rudeger H. T. Wilke, Ke Chen, Arsen Soukiassian, Che-Hui Lee, Wenqing Dai, Qi Li, Joan M. Redwing, Darrell G. Schlom, X. X. Xi, and Kamel Salama. "Clean epitaxial MgB_2 films fabricated by the ex situ annealing of chemical vapour deposition-grown B films in Mg vapour." *Superconductor Science and Technology* 21, no. 4 (2008): 045005.

[71] Pogrebnyakov, A. V., J. M. Redwing, S. Raghavan, V. Vaithyanathan, D. G. Schlom, S. Y. Xu, Qi Li, D. A. Tenne, A. Soukiassian, X. X. Xi, M. D. Johannes, D. Kasinathan, W. E. Pickett, J. S. Wu, and J. C. H. Spence. "Enhancement of the superconducting transition temperature of MgB_2 by a strain-Induced bond-stretching mode softening." *Physical Review Letters* 93, no. 14 (2004): 147006.

[72] Zhang, Peihong, Susumu Saito, Steven G. Louie, and Marvin L. Cohen. "Theory of the electronic structure of alternating MgB_2 and graphene layered structures." *Physical Review B* 77, no. 5 (2008): 052501.

[73] Cristina, Buzea, and Yamashita Tsutomu. "Review of the superconducting properties of MgB2." *Superconductor Science and Technology* 14, (2001).

[74] Welp, U., A. Rydh, G. Karapetrov, W. K. Kwok, G. W. Crabtree, C. Marcenat, L. M. Paulius, L. Lyard, T. Klein, J. Marcus, S. Blanchard, P. Samuely, P. Szabo, A. G. M. Jansen, K. H. P. Kim, C. U. Jung, H. S. Lee, B. Kang, and S. I. Lee. "Superconducting phase diagram of single-crystal MgB_2." *Physica C: Superconductivity* 385, no. 1–2 (2003): 154-161.

[75] Xi, X.X. "MgB_2 thin films." *Superconductor Science and Technology* 22, no. 4 (2009): 043001.

[76] Gümbel, A. "Improved superconducting properties in nanocrystalline bulk MgB_2." *Appl. Phys. Lett.* 80, no. 15 (2002): 2725.

[77] Kumakura, Hiroaki. "Development of high performance MgB_2 tapes and wires." *Journal of the Physical Society of Japan* 81, no. 1 (2012): 1010.

[78] Xu, S., Q. Li, E. Wertz, Y. Hu, and A. Pogrebnyakov…. "High critical current density and vortex pinning of epitaxial MgB_2 thin films." *Physical Review B*, (2003).

[79] Zeng, Xianghui, Alexej V. Pogrebnyakov, Armen Kotcharov, James E. Jones, X. X. Xi, Eric M. Lysczek, Joan M. Redwing, Shengyong Xu, Qi Li, James Lettieri, Darrell G. Schlom, Wei Tian, Xiaoqing Pan, and Zi-Kui Liu. "In situ epitaxial MgB_2 thin films for superconducting electronics." *Nat Mater* 1, no. 1 (2002): 35-38.

[80] Hanna, Mina, Shu-Fang Wang, J. M. Redwing, X. X. Xi, and K. Salama. "Thickness dependence of critical current density in thick MgB_2 films." *IEEE/CSC&ESAS European Superconductivity News Forum* 7, (2009).

[81] Shcherbakova, Olga V., Alexey V. Pan, and Shi Xue Dou. *Magnesium diboride superconductors: development and properties*: VDM Verlag Dr. Müller, 2009.

[82] Putti, Marina, and Giovanni Grasso. "MgB_2, a two-gap superconductor for practical applications." *MRS Bulletin* 36, no. 08 (2011): 608-613.

[83] Dou, Shi, Waikong Yeoh, Olga Shcherbakova, David Wexler, Ying Li, Zhong Ren, Paul Munroe, Sookien Chen, Kaisin Tan, Bartek Glowacki, and Judith MacManus-Driscoll. "Alignment of Carbon Nanotube Additives for Improved Performance of Magnesium Diboride Superconductors." *Advanced Materials* 18, (2006): 785-788.

[84] Serquis, Adriana , Gabriela Pasquini, and Leonardo Civale. "Carbon nanotubes addition effects on MgB_2 superconducting properties." In *Electronic Properties of Carbon Nanotubes*, edited by Jose Mauricio Marulanda, 447-472: InTech, 2011.

[85] Dou, Shi, Waikong Yeoh, Olga Shcherbakova, David Wexler, Ying Li, Zhong Ren, Paul Munroe, Sookien Chen, Kaisin Tan, Bartek Glowacki, and Judith MacManus-Driscoll. "Alignment of carbon nanotube additives for improved performance of magnesium diboride superconductors." *Advanced Materials* 18, no. 6 (2006): 785-788.

[86] Yeoh, W. K., J. Horvat, S. X. Dou, and P. Munroe. "Effect of carbon nanotube size on superconductivity properties of MgB_2." *Applied Superconductivity, IEEE Transactions on* 15, no. 2 (2005): 3284-3287.

[87] Serquis, A., G. Serrano, S. M. Moreno, L. Civale, B. Maiorov, F. Balakirev, and M. Jaime. "Correlated enhancement of H_{c2} and J_c in carbon nanotube doped MgB_2." *Superconductor Science and Technology* 20, no. 4 (2007): L12.

[88] Larbalestier, David, Alex Gurevich, D. Matthew Feldmann, and Anatoly Polyanskii. "High-T_c superconducting materials for electric power applications." *Nature* 414, no. 6861 (2001): 368-377.

[89] Bud'ko, S. L., C. Petrovic, G. Lapertot, C. E. Cunningham, P. C. Canfield, M. H. Jung, and A. H. Lacerda. "Magnetoresistivity and H_{c2}(T) in MgB_2." *Physical Review B* 63, no. 22 (2001): 220503.

---

i Van Delft, D. and P. Kes (2010) The Discovery of Superconductivity. Phys. Today 63(9), 38-43

ii Meissner, W.; R. Ochsenfeld (1933). "Ein neuer Effekt bei Eintritt der Supraleitfähigkeit". *Naturwissenschaften* **21** (44): 787–788.

iii Paolo Mele (2012) "Superconducting properties of iron chalcogenide thin films." Sci. Technol. Adv. Mater. **13** 054301

iv Chu, C. W. and B. Lorenz (2009) High pressure studies on Fe-pnictide superconductors. *Physica C: Superconductivity 469(9-12)*, 385-395

1 I. Felner, U. Asaf, Y. Levi, and O. Millo *Phys. Rev. B*, VOLUME 55, NUMBER 6 (1997)

2 Jeff Tallon et. al. *IEEE Transactions on Applied Superconductivity*, VOL. 9, NO. 2, (1999)

3 Jun Sung Kim, Seunghyun Khim, Liqin Yan, N Manivannan,Yong Liu, Ingyu Kim, G R Stewart and Kee Hoon Kim"Evidence for coexistence of superconductivity and magnetism in single crystals of Co-doped SrFe2As2" *J. Phys.: Condens. Matter 21 (2009) 102203 (6pp)*

4 Jiun-Haw Chu, James G. Analytis, Chris Kucharczyk, Ian R. Fisher "Determination of the phase diagram of the electron doped superconductor Ba(Fe1−xCox)2As2" *Phys. Rev. B 79, 014506 (2009)*

5 Liling Sun, Jing Guo, Genfu Chen, Xianhui Chen, Xiaoli Dong, Wei Lu, Chao Zhang, Zheng Jiang, Yang Zou, Suo Zhang, Yuying Huang, Qi Wu, Xi Dai,1Yuanchun Li, Jing Liu, and Zhongxian Zhao, *"Valence change of europium in EuFe2As1.4P0.6and compressed EuFe2As2and its relation tosuperconductivity" PHYSICAL REVIEW B 82, 134509 2010*

6 Guanghan Cao, Shenggao Xu, Zhi Ren1, Shuai Jiang2, Chunmu Feng and Zhu'an Xu, "Superconductivity and ferromagnetism in EuFe2(As1−xPx)2" *J. Phys.: Condens. Matter 23 (2011) 464204*

v Naurang Lal Saini "Nanoscale structure and atomic disorder in the iron-based chalcogenides." Sci. Technol. Adv. Mater. **14** (2013) 014401

vi Qiang Li,Weidong Si and Ivo K Dimitrov (2011) Films of Iron Chalcogenide Superconductors. Rep. Prog. Phys. **74** 124510

vii Mizuguchi Y and Takano Y 2010 *J. Phys. Soc. Japan* **79** 102001

viii Yhan, WYLi, LXCao, Szhang, B.Xu and B.R.Zhao, Preparation and superconductivity of iron selenide thin films. J. Phys.: Condens. Matter 21 (2009) 235702

ix C. Yang, L. Cao, N. Chen, W. Li, L. Liu, and Y. Zhang. *Preparation and Transport Properties of Superconducting FeTe Thin Film.* Advanced Materials Research Vol. 629 (2013) pp 236-239

x W. Si, Q. Jie, L. Wu, J. Zhou, G. Gu, P.D. Johnson, and Q. Li, Superconductivity in epitaxial thin films of $Fe_{1.08}Te$:O_X Phys. Rev. B 81, 092506 (2010)

xi Paolo Mele (2012) "Superconducting properties of iron chalcogenide thin films." Sci. Technol. Adv. Mater. **13** 054301

xii Takanori KIDA, Takahiro MATSUNAGA, Masayuki HAGIWARA1, Yoshikazu MIZUGUCHI2, Yoshihiko TAKANO, and Koichi KINDO Upper Critical Fields of the 11-System Iron-Chalcogenide Superconductor FeSe0:25Te0:75 Journal of the Physical Society of Japan Vol. 78, No. 11, November, 2009, 113701

xiii Lee, Jeong-O and Kim, Jae-Ryoung and Kim, Ju-Jin and Kim, Jinhee and Kim, Nam and Park, Jong Wan and Yoo, Kyung-Hwa and Park, Kang-Ho, *"Magnetoresistance and differential conductance in multiwalled carbon nanotubes"* Phys. Rev. B **61**, R16362(R) (2000)

12. APPENDIX 1.

Centers of Excellence of Nanotech Institute/Phys Department created in support of AFOSR Project on 'Strengthening Superconductivity in Nanostructures"

During 5 year program the unique centers equipped by closed cycled liquid He systems have been created in UTD with the help of matching costs funds ($ 500 K additionally to AFOSR $ 3 M funding)

Currently, the equipment valued at approximately $ 1,5 M is placed in three labs and space there is fully occupied. In addition, two smaller service rooms and part of old clean room service chase corridors are used for storage of supplies and gas cylinders. Approximately, the Solar NANOFab (ECSN 2.406) lab occupies approximately 1500 sq. ft , the Cryogenics Center (ECSN 2.404a) houses the PPMS and MPMS systems occupies 400 sq. ft. and the Cryogenics Annex (Berkner 2.306) lab occupies 600 sq.ft. as shown at the diagrams below.

The labs are located in area of former cleanroom that is very favorable for efficient equipment operation.

1. CRYO-Center: The expensive PPMS and MPMS systems by "Quantum Design" have closed cycle He systems that require constant operation of two powerful compressors. They need to be a least 6ft away from systems for sound and vibration isolation.A power outage causes loss of liquid He inside systems and the refill may cost up to $4K. Even in well-equipped ECS building such events occur quite frequently.

There is high demand for the PPMS and MPMS systems of CRYO Center from Prof. Julia Chen group, Nanotech and surrounding universities (UT Arlington, Texas State, SMU).

2. Thin Film NANOFab lab includes Multi-chamber vacuum deposition system by "Angstrom Engineering" (of $ 500 K value) four glove boxes that require continuous Ni gas supply (loading dock). Two of the glove boxes are connected together and include complicated evaporator systems

Below, diagrams of labs are shown with lists of equipment currently used. Also power needs of equipment and other additional needs

Cryogenics Center ECSN 2.404a

The following equipment is installed:

1. **CCS**- Closed Cycle System: 10 – 300K Transport
2. **MPMS**- Magnetic Properties measurement system: 2 - 400K Magnetic Susceptibility
3. **PPMS**- Physical Properties Measurement System: 2 - 400K Transport, Hall effect, and magneto-transport

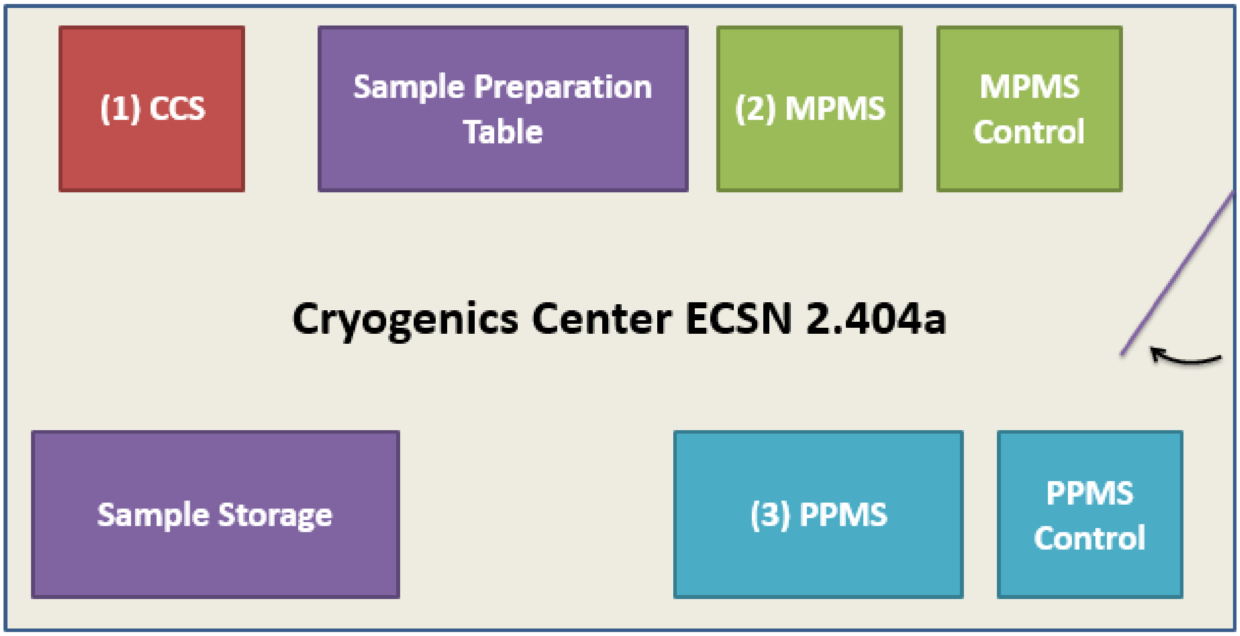

Power and other needs:

- Thirty 110V, 15A outlets
- Four 208-240V, 30A outlets
- Ultra High Purity He gas
- He Liquid
- Loading Dock
- Uninterrupted Power Supply – Emergency Generators (each power outage requires refill of liquid He with approximate cost of $4K)
- Water Chill
- Sample preparation space
- Installation of compressors at least 6ft from PPMS and MPMS system for vibration protection

<u>Cryogenics Annex Berkner 2.306 (is not planned for move now)</u>

1. **Sample Sealing**- Turbo Pump cart with Nitrogen trap to seal samples under high vacuum
2. **ESR**- Electronic Spin Resonance system: 4 - 300K Counts number of spins
3. **Charging and Measurements Table**- Electrochemical Charging Setup

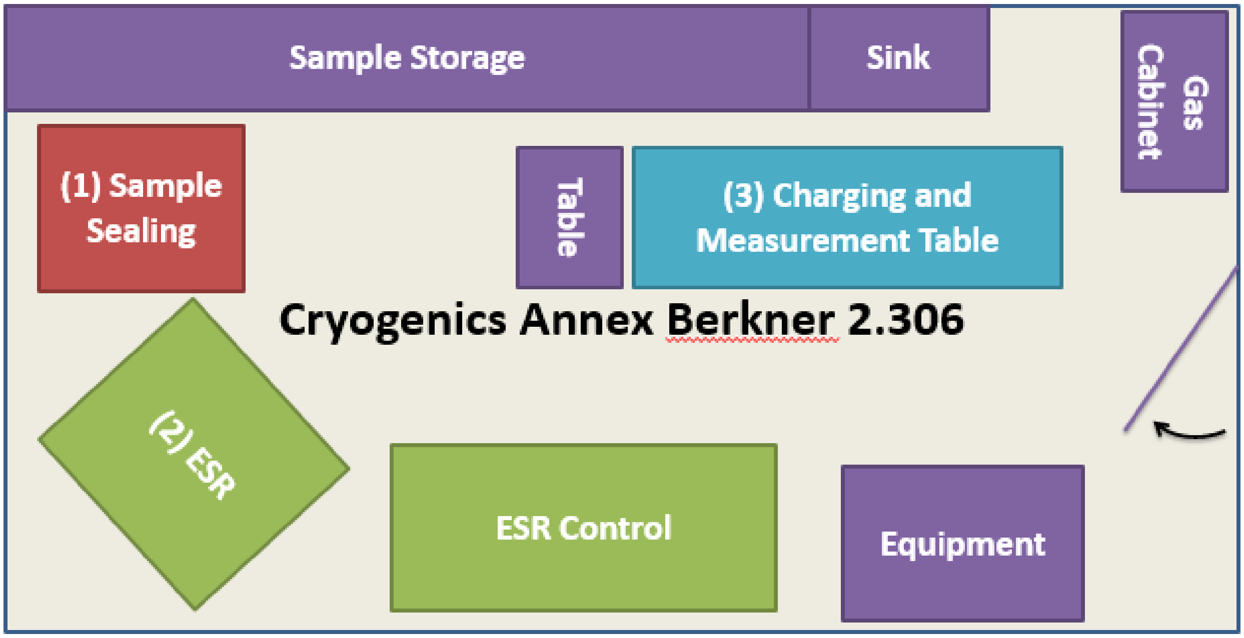

Thin Film NANOFab ECSN 2.406

The following equipment are installed:

1. **Organics Deposition**- Eight Source, High Vacuum, Organics thermal deposition system with codeposition and PID control. Glovebox prevents oxidization of samples. High-vacuum load lock allows transfer between systems, Plasma Cleaning and Mask changing.
2. **Metals Deposition**- Five Source, High Vacuum, High Power, Metals Thermal Deposition system with codeposition and PID control. Glovebox prevents oxidization of samples and has spincoating station.
3. **Measurements Table**- Stylus Profilometer, and PV Optical measurement system
4. **Solar Simulator**- AM1.5G 2x2 inch solar simulator in a Glovebox

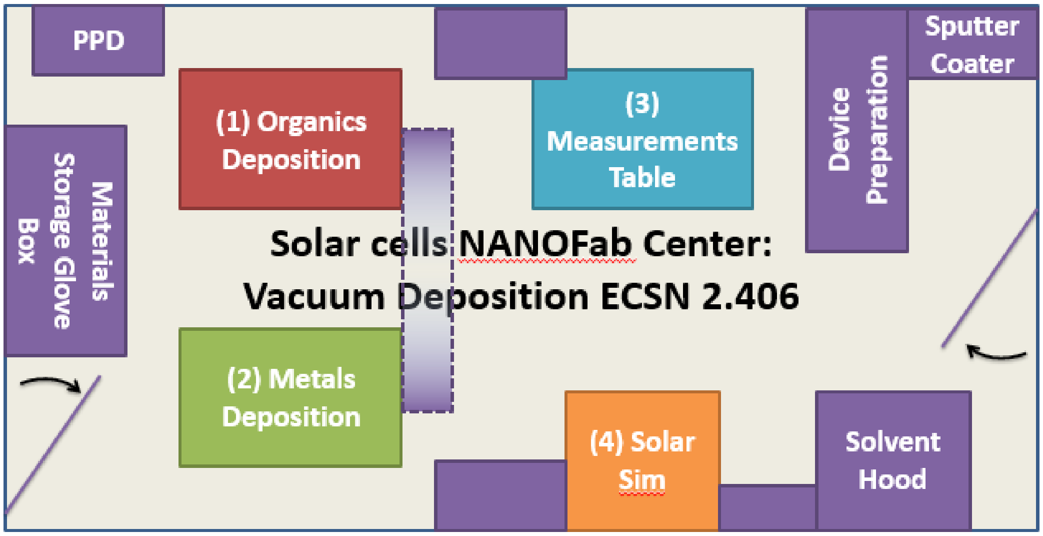

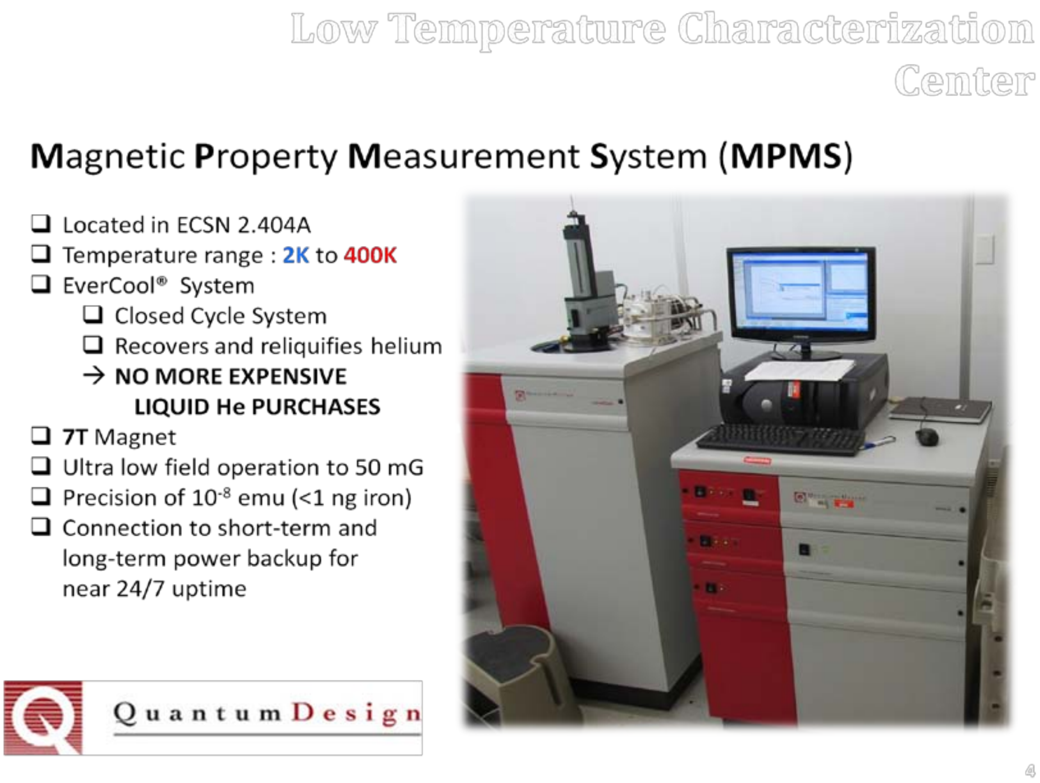

Low Temperature Characterization Center

Magnetic Property Measurement System (MPMS)

☐ Located in ECSN 2.404A
☐ Temperature range : 2K to 400K
☐ EverCool® System
    ☐ Closed Cycle System
    ☐ Recovers and reliquifies helium
    → **NO MORE EXPENSIVE LIQUID He PURCHASES**
☐ **7T** Magnet
☐ Ultra low field operation to 50 mG
☐ Precision of 10^{-8} emu (<1 ng iron)
☐ Connection to short-term and long-term power backup for near 24/7 uptime

QuantumDesign

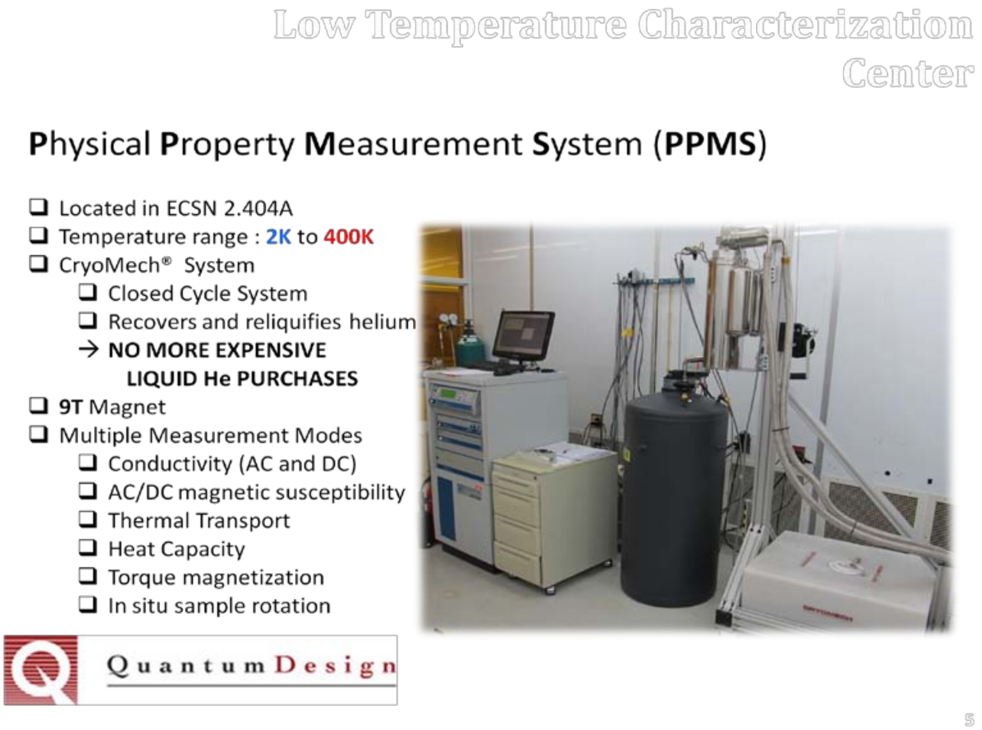

Low Temperature Characterization Center

Physical Property Measurement System (PPMS)

☐ Located in ECSN 2.404A
☐ Temperature range : 2K to 400K
☐ CryoMech® System
    ☐ Closed Cycle System
    ☐ Recovers and reliquifies helium
    → **NO MORE EXPENSIVE LIQUID He PURCHASES**
☐ **9T** Magnet
☐ Multiple Measurement Modes
    ☐ Conductivity (AC and DC)
    ☐ AC/DC magnetic susceptibility
    ☐ Thermal Transport
    ☐ Heat Capacity
    ☐ Torque magnetization
    ☐ In situ sample rotation

QuantumDesign

A Search for New SUPERCONDUCTING materials can be effectively conducted at ESR/LFMA Cry-center II by contactless Microwave methode

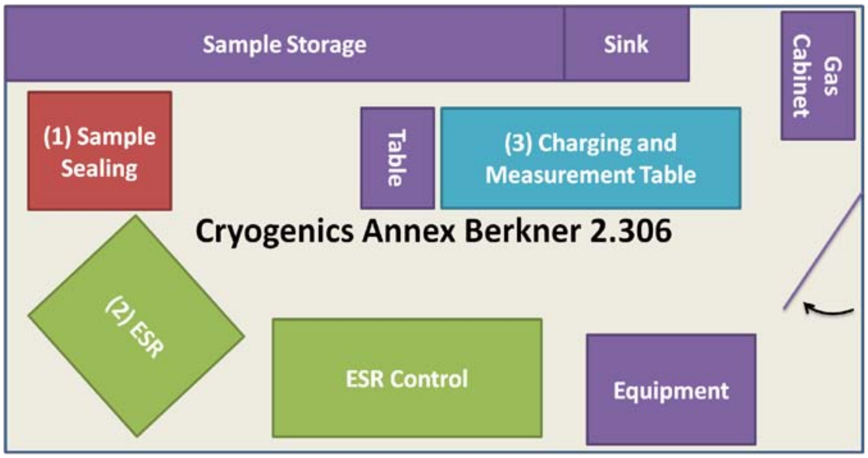

1. **Sample Sealing**- Turbo Pump cart with Nitrogen trap to seal samples under high vacuum
2. **ESR**- Electronic Spin Resonance system: 4 - 300K Counts number of spins
3. **Charging and Measurements Table**- Electrochemical Charging Setup

Low Temperature Characterization Center

Electron **P**aramagnetic **R**esonance (**EPR**)

- ❑ Located in BE 2.306
- ❑ Temperature range : **4K** to **300K**
- ❑ ColdEdge cryogen-free system
  - ❑ Refrigerates helium gas
  - → **NO MORE EXPENSIVE LIQUID He PURCHASES**
- ❑ Detection of gyromagnetic ratio and spin
- ❑ Detection and characterization of superconductors
- ❑ Can detect nanograms of superconducting material
- ❑ **1T** Magnet
- ❑ X-band (10 GHz) microwave source

BRUKER

Organic Electronics Fabrication Center

Multi-Chamber, Multi-Source Thin Film Evaporator:

Organic Electronics Fabrication Center

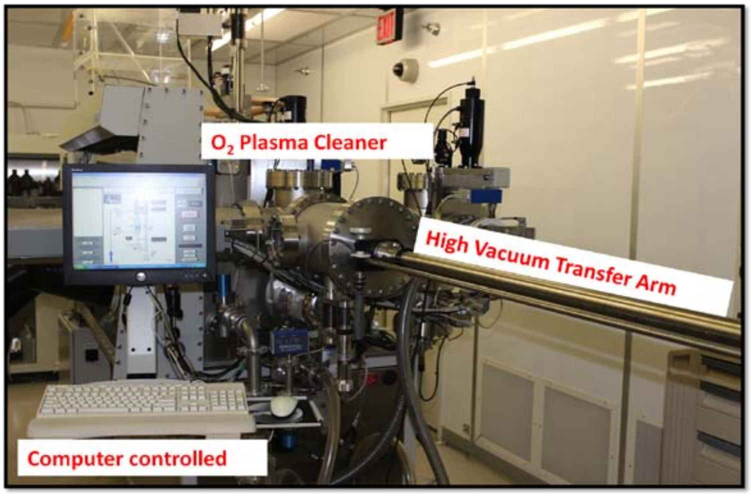

Multi-Chamber, Multi-Source Thin Film Evaporator:

Organic Electronics Fabrication Center

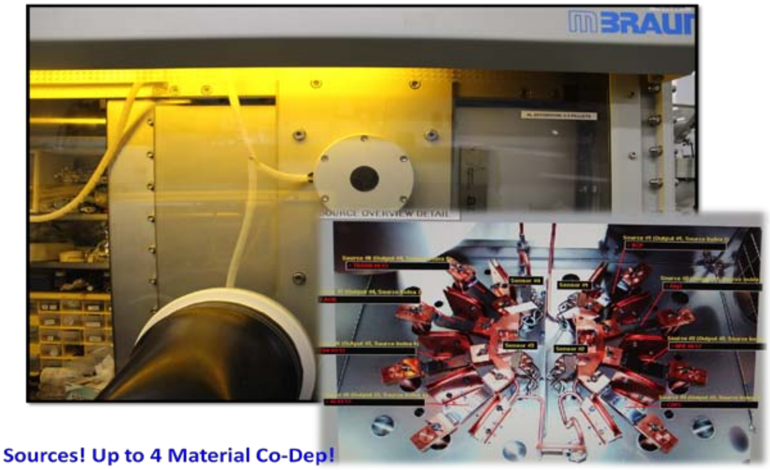

8 Sources! Up to 4 Material Co-Dep!

Organic Electronics Fabrication Center

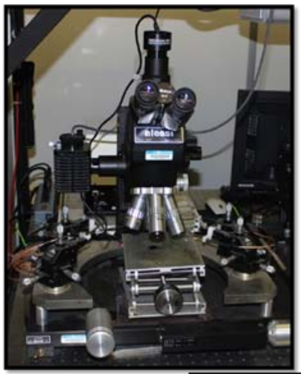

Probe Station
+
Microscope

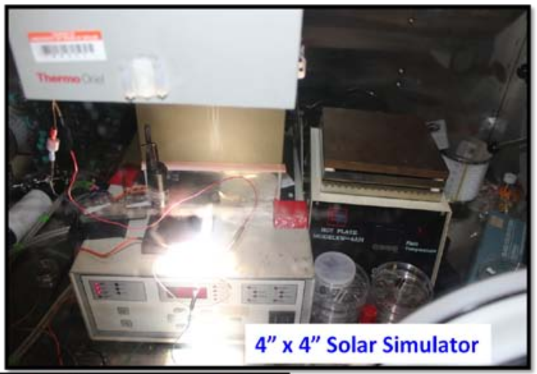

4” x 4” Solar Simulator

Surface Profilometer (<10nm)

Organic Electronics Fabrication Center

5 Source Metals Evaporator with E-Beam Upgrade Capability

Online Reservation System

nanoWeb v4.0

- ❑ Online Reservation Tool → Usage Tracking via reservations and equipment logins
- ❑ File repository

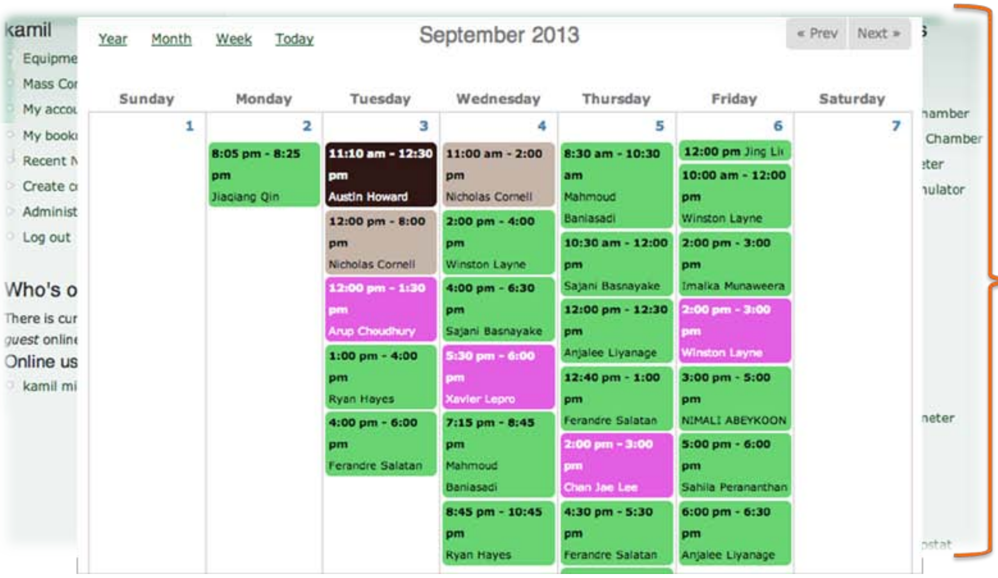

September 2013

Sunday	Monday	Tuesday	Wednesday	Thursday	Friday	Saturday
1	2	3	4	5	6	7
	8:05 pm - 8:25 pm Jiaqiang Qin	11:10 am - 12:30 pm Austin Howard 12:00 pm - 8:00 pm Nicholas Cornell 12:00 pm - 1:30 pm Arup Choudhury 1:00 pm - 4:00 pm Ryan Hayes 4:00 pm - 6:00 pm Ferandre Salatan	11:00 am - 2:00 pm Nicholas Cornell 2:00 pm - 4:00 pm Winston Layne 4:00 pm - 6:30 pm Sajani Basnayake 5:30 pm - 6:00 pm Xavier Lepro 7:15 pm - 8:45 pm Mahmoud Baniasadi 8:45 pm - 10:45 pm Ryan Hayes	8:30 am - 10:30 am Mahmoud Baniasadi 10:30 am - 12:00 pm Sajani Basnayake 12:00 pm - 12:30 pm Anjalee Liyanage 12:40 pm - 1:00 pm Ferandre Salatan 2:00 pm - 3:00 pm Chan Jae Lee 4:30 pm - 5:30 pm Ferandre Salatan	12:00 pm Jing Li 10:00 am - 12:00 pm Winston Layne 2:00 pm - 3:00 pm Imalka Munaweera 2:00 pm - 3:00 pm Winston Layne 3:00 pm - 5:00 pm NIMALI ABEYKOON 5:00 pm - 6:00 pm Sahila Perananthan 6:00 pm - 6:30 pm Anjalee Liyanage	

Color Coded Status

APPENDIX 3.
Superconducting TEXTILES.

The flexibility of these CNT laminated MgB_2-CNT yarns enables them to be weaven into textiles (**Figure 3f** and **Figure S5**). The room temperature resistance of these MgB_2-CNT yarns have been stable for more than 60 cycles during the bending cycling test (**Figure S6**). The rupture tensile strength normalized by gravimetric density of MgB_2-CNT yarns reaches 161±47 MPa g^{-1} m^3 and exceeds the tensile strength of conventional metal-sheathed MgB_2 wires [20]
(**Figure S7** and **Table S2**).

xivQ. Wang et al. Interface induced high temperature superconductivity in single unit-cell FeSe films on SrTiO3 *Chinese Phys Letters*

xvQ. Wang et al. Interface induced high temperature superconductivity in single unit-cell FeSe films on SrTiO3 *Chinese Phys Letters*

AFOSR Deliverables Submission Survey

Response ID:4313 Data

1.

1. Report Type

Final Report

Primary Contact E-mail
Contact email if there is a problem with the report.

zakhidov@utdallas.edu

Primary Contact Phone Number
Contact phone number if there is a problem with the report

9728836218

Organization / Institution name

University of Texas at Dallas

Grant/Contract Title
The full title of the funded effort.

STRENGTHENING SUPERCONDUCTIVITY IN MACRO-ARRAYS OF NANOCLUSTERES AND NANOSTRUCTURES

Grant/Contract Number
AFOSR assigned control number. It must begin with "FA9550" or "F49620" or "FA2386".

FA9550-09-1-0384

Principal Investigator Name
The full name of the principal investigator on the grant or contract.

Anvar Zakhidov

Program Manager
The AFOSR Program Manager currently assigned to the award

Dr. Harold Weinstock

Reporting Period Start Date

11/01/ 2009

Reporting Period End Date

10/30/2014

Abstract

Objective of this project was to create nanostructured superconducting systems with higher Hc and Jc for power applications as nanocomposite wires and also to search for new types of superconducting nanomaterials with higher critical temperature Tc. The interfacial novel phase have been confirmed to have a record Tc = 47-49 in Pr and other rare earth doped Ca 122 pnictide superconductors by ultrasensitive low-field microwave absorption method. Coexistence of lower Tc and higher Tc observed by LFMA proves the interfacial nature of newly found SC phase. on the contrary the LFMA in 122 pnictide shows only one signal and one phase. In thin films of FeSeTe films deposited by pulsed laser deposition very high Hc, (estimated to be 186 T by HWW formula) has been achieved at the compositions close to antiferomagnetic order. Flexible, weavable and knottable superconducting magnesium diboride yarns have been fabricated that provide attractive gravimetric properties as a superconductor, while having a 20 times lower density than for bulk MgB2. These yarns are made by templating forest-drawn

carbon nanotube (CNT) aerogel sheets with boron using photothermal decomposition of BBr3 produced by a scanned laser beam, conversion of the B-CNT nanofiber arrays to MgB2-CNT.

Distribution Statement
This is block 12 on the SF298 form.

Distribution A - Approved for Public Release

Explanation for Distribution Statement
If this is not approved for public release, please provide a short explanation. E.g., contains proprietary information.

SF298 Form
Please attach your SF298 form. A blank SF298 can be found here. Please do not password protect or secure the PDF The maximum file size for an SF298 is 50MB.

AFD-070820-035.pdf

Upload the Report Document. File must be a PDF. Please do not password protect or secure the PDF . The maximum file size for the Report Document is 50MB.

3 Final Report on Strengthening.pdf

Upload a Report Document, if any. The maximum file size for the Report Document is 50MB.

Archival Publications (published) during reporting period:

1. Microwave conductance of aligned multiwall carbon nanotube textile sheets
Brown, Brian L.; Bykova, Julia S.; Howard, Austin R.; A.Zakhidov, M. Lee.
APPLIED PHYSICS LETTERS Volume: 105 Issue: 26, 2014,

2. "Comparison of Pr-doped Ca 122 and Ca 112 Pnictides by Low-field Microwave Absorption Spectroscopy", Austin R. Howard, Jonathan D. Yuen, Bing Lv, Myron Salamon, Ching-Wu Chu and Anvar A. Zakhidov, MRS Proceedings / Volume 1684 / 2014, pp.

3. Flexible, Ultralight, Porous Superconducting Yarns Containing Shell-Core Magnesium Diboride-Carbon Nanotube Nanofibers
Bykova, Julia S.; Lima, Marcio Dias; Haines, Carter S.; et al.
ADVANCED MATERIALS Volume: 26 Issue: 44 Pages: 7510-7515, 2014

1. Controlling the Optical, Electrical and Chemical Properties of Carbon Inverse Opal by Nitrogen Doping
Morelos-Gomez, Aaron; Mani-Gonzalez, Pierre G.; Aliev, Ali E.; A. Zakhidov
ADVANCED FUNCTIONAL MATERIALS Volume: 24 Issue: 18 Pages: 2612-2619

2. Superconducting properties of FeSexTe1-x thin film with a composition close to antiferromagnetic ordering
By: Chen, Li; Huang, Jijie; Tsai, Chen-Fong; N. Cornell, M.Salamon, A. Zakhidov, H. Wang
SUPERCONDUCTOR SCIENCE & TECHNOLOGY Volume: 26 Issue: 11 NOV 2013

3. Ionic plasma screening and long-range electron correlations in quasi-one-dimensional conductors
Gartstein, Yu N.; Zakhidov, A. A.
PHYSICS LETTERS A Volume: 377 Issue: 19-20 Pages: 1390-1394

4. Tunable interplay between 3d and 4 f electrons in Co-doped iron pnictides
Shang, T.; Yang, L.; Chen, Y.; Zakhidov A., et al.
PHYSICAL REVIEW B Volume: 87 Issue: 7

5. Carbon nanotube/graphene nanocomposite as efficient counter electrodes in dye-sensitized solar cells
Velten, Josef; Mozer, Attila J.; Li, Dan; Ray Baughman, A. Zakhidov

NANOTECHNOLOGY Volume: 23 Issue: 8 (2013)

6. Anand, B., Podila, R., Ayala, P., Oliveira, L., Philip, R., Sai, S. S. S., Zakhidov, A. A., Rao, A. M. Non-linear optical properties of B-doped single-walled carbon nanotube, Nanoscale accepted (2013)

7. Diamond Direct and Inverse Opal Matrices Produced by Chemical Vapor Deposition
Ralchenko, V. G.; Sovyk, D. N.; Bolshakov, A. P.; et al.
PHYSICS OF THE SOLID STATE Volume: 53 Issue: 6 Pages: 1131-1134,

8. Biscrolling Nanotube Sheets and Functional Guests into Yarns
Lima, Marcio D.; Fang, Shaoli; Lepro, Xavier; et al.
SCIENCE Volume: 331 Issue: 6013 Pages: 51-55

9. Fabrication of biscrolled fiber using carbon nanotube sheet", by R. H. Baughman, S. Fang, M. Lima, A. Zakhidov, et.al. PCT/US2010/036378 patent, 2010.

10. Structural Model for Dry-Drawing of Sheets and Yarns from Carbon Nanotube Forests
Kuznetsov, Alexander A.; Fonseca, Alexandre F.; Baughman, Ray H.; et al.
Source: ACS NANO Volume: 5 Issue: 2 Pages: 985-993

11. Ayala, P. et al. Evidence for substitutional boron in doped single-walled carbon nanotubes. Applied Physics Letters 96, doi:18311010.1063/1.3427432 (2010).

12. Structure and process-dependent properties of solid-state spun carbon nanotube yarns
Fang, Shaoli; Zhang, Mei; Zakhidov, Anvar A.; et al.
JOURNAL OF PHYSICS-CONDENSED MATTER Volume: 22 Issue: 33, 2010

16. Podila, R. et al. Spectroscopic investigation of nitrogen doped graphene. Applied Physics Letters 101, doi:12310810.1063/1.4752736 (2012).

17 Hitchcock, D., Yang, K. Q., He, J. & Rao, A. M. Electrical Transport Properties Of Single-Walled Carbon Nanotube Bundles Treated With Boric Acid. Nano 6, 337-341, (2011).

18. Yang, K. Q. et al. Tuning electrical and thermal connectivity in multiwalled carbon nanotube buckypaper. Journal of Physics-Condensed Matter 22, /22/33/334215 (2010).

19. Yang, K. Q. et al. Inter-tube bonding, graphene formation and anisotropic transport properties in spark plasma sintered multi-wall carbon nanotube arrays. Carbon 48, 756-762, 2010).

20. Podila, R., Rao, R., Tsuchikawa, R., Ishigami, M. & Rao, A. M. Raman Spectroscopy of Folded and Scrolled Graphene. ACS Nano 6, 5784-5790, (2012).

21. Rao, R. et al. Effects of Layer Stacking on the Combination Raman Modes in Graphene. ACS Nano 5, 1594-1599, (2011).

22. J. Zhu, L. Oliveira, R. Podila, J. He, M. Skove, A. Howard, A. A. Zakhidov, and A. M. Rao,
Magnetization Study of Sulfur-doped Graphitic Nano-platelets and Single Walled
Carbon Nanotubes

23. L. Chen, J. Huang, C.-F. Tsai, Y. Zhu, J. Jian, A. Chen, Z. Bi, F. Khatkhatay, N. Cornell,
A. Zakhidov, and H. Wang, Supercond. Sci. Technol. 26, 112001 (2013)
24. L. Chen, C.-F. Tsai, J. H. Lee, X. Zhang, and H. Wang, Jpn. J. Appl. Phys. 52, 020201
(2013)
25. J. Huang, L. Chen, J. Jian, F. Khatkhatay, and H. Wang, Supercond. Sci. Technol. 27,

105006 (2014)
26. Ilya Grigorenko and Anvar Zakhidov, "Superconductivity in an Inhomogeneous Bundle of Metallic and Semiconducting Nanotubes", Journal of Nanotechnology
Volume 2013 (2013), Article ID 367270, 6 pages

27. D. Vandervelde, H. Q. Yuan, Y. Onuki and M. B. Salamon, "Evidence of d-wave pairing symmetry of the gap of the heavy-fermion superconductor CeIrIn5 from magnetic-penetration-depth measurements," Phys. Rev. B 79, 212505 (1-4) (2009).

28. J. Chen, M. B. Salamon, S. Akutagawa, J. Akimitsu, J. Singleton, J. L. Zhang, L. Jiao, and H. Q. Yuan "Evidence of nodal gap structure in the noncentrosymmetric superconductor Y2 C3" Phys. Rev. B 83, 144529/1-4 (2011).

29. X. Y. Tee, H. G. Luo, T. Xiang, D. Vandervelde, M. B. Salamon, H. Sugawara, H. Sato, C. Panagopoulos,1and Elbert E. M. Chia, Penetration-depth study of LaOs4Sb12: Multiband s-wave superconductivity, Phys. Rev. B 86, 064518/1-5 (2012)

30. Ali E. Aliev, Ka Xiong, Kyeongjae Cho and M. B. Salamon, Reversible superconductivity in electrochromic indium-tin oxide films, Appl. Phys. Lett. 101, 252603 (2012).

Ph.D. Dissertations prepared as a result of the Program:

31. Austin Ross Howard: MAGNETICALLY MODULATED MICROWAVE SPECTROSCOPY OF LAYERED AND QUASI-2D SUPERCONDUCTORS: IRON PNICTIDES AND CHALCOGENIDES, Thesis defended and published in UTD, 2014

32. Julia Sergeevna Bykova: CARBON NANOTUBE - MAGNESIUM DIBORIDE COMPOSITES FOR SUPERCONDUCTING YARNS, Thesis defended and published in UTD, 2014

32. Nicholas Ley Cornell: ELECTROPHYSICAL PROPERTIES OF LAYERED SUPERCONDUCTING NANOSTRUCTURES: ADVANCED SYNTHESIS AND TUNING, Thesis defended and published in UTD, 2014

Changes in research objectives (if any):

Change in AFOSR Program Manager, if any:

Extensions granted or milestones slipped, if any:

No-Cost extension granted once

AFOSR LRIR Number

LRIR Title

Reporting Period

Laboratory Task Manager

Program Officer

Research Objectives

Technical Summary

Funding Summary by Cost Category (by FY, $K)

	Starting FY	FY+1	FY+2
Salary			
Equipment/Facilities			
Supplies			
Total			

Report Document

Report Document - Text Analysis

Report Document - Text Analysis

Appendix Documents

2. Thank You

E-mail user

Jan 31, 2015 23:43:14 Success: Email Sent to: zakhidov@utdallas.edu